University of Strathclyde
Department of Physics

Submitted in partial fulfilment of the requirements
for the degree of Doctor of Philosophy

Orbital Angular Momentum and Fully Structured Light in Nonlinear Media and Cavities

Christopher John Gibson

1st *Supervisor*:
Dr. Alison Yao

2nd *Supervisor*:
Prof. Gian-Luca Oppo

April 2019

This thesis is the result of the authors original research. It has been composed by the author and has not been previously submitted for examination which has led to the award of a degree.

Signed:

Date:

Published material

Papers published or submitted to peer-reviewed journals

- Christopher J. Gibson, Alison M. Yao and Gian-Luca Oppo, "Optical Rogue Waves in Vortex Turbulence," *Phys. Rev. Lett.*, **116**, 043903, 2016.
- Christopher J. Gibson, Patrick Bevington, Gian-Luca Oppo and Alison M. Yao, "Control of polarization rotation in nonlinear propagation of fully structured light," *Phys. Rev. A.*, **97**, 033832, 2018.
- S. Barland, M. Brambilla, L. Columbo, B. Garbin, C. J. Gibson, M. Giudici, F. Gustave, C. Masoller, G.-L. Oppo, F. Prati, et al., Chapter 1 in *Nonlinear Guided Wave Optics* (IOP Publishing, 2017), 2053-2563, pp. 11 to 128.
- Christopher J. Gibson, Alison M. Yao and Gian-Luca Oppo, "Spatially Rotating Solutions and Structured Light in a Vectorial Kerr Cavity," *to be submitted*

Conference contributions: Talks and poster presentations

- *Optical Rogue Waves in Vortex Turbulence*, talk at EQEC 2015, Conference, International Congress Centre, Munich, 2015
- *Fully structured light in a vectorial Kerr cavity*, poster at ICOAM 2017, Conference, Sala Ipogea - Piazza Edwin Cerio, Anacapri, 2017

- *Control of Polarisation Rotation and Fragmentation of Vector Vortex Beams in Nonlinear Media*, poster at EQEC 2017, Conference, International Congress Centre, Munich, 2017

Abstract

The work in this thesis describes interesting phenomena that results from the interaction between high intensity laser light and nonlinear matter. By changing the structure of light's properties such as intensity and polarisation as well as the type of nonlinear action that occurs during propagation through the medium, we aim to describe how the properties of light are affected by the various interactions.

Considering down-conversion in a second order $\chi^{(2)}$ medium we first present a spatio-temporal mechanism for producing two dimensional optical rogue waves in a turbulent state driven by vortices with helical wavefronts. Self-organising hexagonal structures bound in phase lose stability and synchronised oscillations are unstable leading to phase-unbound vortex-mediated turbulence with high excursions in amplitude. Nonlinear amplification leads to rogue waves close to optical vortices, and probability density functions typical of rogue waves.

We then consider fully structured light (FSL) within a Kerr $\chi^{(3)}$ medium. In particular, we describe how the polarisation distribution of FSL beams is affected by propagation. In the linear case we derive an expression for the rotation of the polarisation and show the rotation is due to the difference in Gouy phase between the two eigenmodes in the beam. For nonlinear propagation we show the effect of the cross-phase modulation from self focusing results in additional rotation that can be controlled by changing various physical parameters of the FSL beam like the beam waist and magnitude of OAM.

Finally we consider the interaction with the Kerr medium in an optical cavity. Above Turing threshold we observe the formation of peaks upon the FSL structure. Where the beam carries a net orbital angular momentum we observe a rotation in the structure. We detail how the angular velocity of the Turing structure can be controlled by careful selection of the parameters of the FSL beams.

Acknowledgements

It is a great pleasure to have this opportunity to give my many thanks and appreciation to the people that have all helped in one way or another over the course of this experience.

Firstly I cannot thank my two supervisors, Alison Yao and Gian-Luca Oppo enough for the time, effort and support they have given. A great thanks for putting up with me over these long four years - your knowledge, expertise and guidance along the way has been invaluable.

Secondly a massive thanks to my family - my Mum, Dad, Gran, Grandad, Sister and better half Kerry - who have all supported me on this journey and all been there to lend an ear through both the good times and the bad.

Thirdly I would like to acknowledge and thank Duncan McArthur for all the help along the way. The coffee and fresh air breaks to discuss our work and progress as well as the help using python to create these lovely thesis images did not go unappreciated.

Lastly and by no means least to all the friends I have met along the way. A mention to the Strathclyde pool team and all its members who have been there when I needed a break and have made a lot of incredible memories.

Contents

Chapter 1

Introduction

In 1917 Einstein's prediction of stimulated emission [1] paved the way for the development of high intensity monochromatic radiation which after much development later became known as the laser (Light Amplification by Stimulated Emission of Radiation). Stimulated emission involves the interaction of a photon with an excited atom or molecule and results in another photon being released with identical properties to the incident photon such as frequency, phase and polarisation. By using an optical resonator to reflect these photons through the medium multiple times, this process can occur repeatedly in a chain reaction such producing more and more photons. The resulting field then contains many photons in phase with the same frequencies and resulting in a coherent source of high intensity monochromatic waves. Initially such a system were limited to the microwave region and during the 1950s there was many theoretical and experimental interest behind the production of high intensity coherent microwaves [2–4]. In 1958 it was suggested that these techniques could be extended into the optical and infrared region of the electromagnetic spectrum using potassium vapour and a centimetre dimensional resonant cavity [5]. Indeed, using Townes hard theoretical work the first functional laser was born using a high energy source to excite synthetic ruby as the lasing medium and the study of optics was changed forever [6].

In everyday life the typical intensities of light are low and not enough to induce any nonlinear response from a given medium that the light interacts with. Original studies of light focused on such linear systems and interactions under the assumption that the refractive index is a constant and given by the relative susceptibility of a particular medium as $n_0 \equiv \sqrt{\varepsilon_r}$. This allows a great understanding of how light behaves in systems involving mirrors, lenses and diffraction gratings. Advancements were made through the discovery of various linear phenomenon such as Snell's law which dictates the angles of incidence and refraction when changing medium, dispersion which dictates that the angle of refraction is frequency dependent resulting in light splitting to its constituent colours through a prism and many other phenomena such as diffraction and interference.

However with the invention of the laser in 1960, light with intensities high enough to induce a nonlinear response of the dielectric polarisation allowed the realisation of new and more interesting phenomena where the refractive index is no longer a constant but intensity dependent. One of the first nonlinear effects studied was by Peter Franklin who displayed the possibility for the realisation of optical harmonics where a high intensity incident beam can interact with a medium producing a new second field with double the frequency [7] - a process which has become known as second harmonic generation. This paved the way for the discovery of many other frequency mixing processes such as sum frequency generation, where two incident field produce a third with a frequency that is the sum of the incident field and various others such as optical parametric oscillation [8, 9]. Further nonlinear phenomena attracted interest such as self-focussing, where a spatially structured beam focuses upon propagation in a medium due to the difference in refractive index between the high intensity centre of the beam and the low intensity boundaries of the beam referred to as the optical Kerr effect [10, 11]. Such exotic phenomena from the nonlinear response of a medium to the intensity of light has resulted in the discovery of cross phase modulation where one mode of light can affect that of another [12], modulation instability where the nonlinearity amplifies deviation from a periodic wave function which has resulted in the observation of optical solitons, four wave mixing and deterministic chaos within optical systems [13, 14]. To this day

the field of nonlinear optics since the invention of the laser continues to attract a lot of interest.

Lasers have come a long way since then and there is now barely an optical device that does not use such a source of light, from phones, computers and CD readers to pocket sized laser pointers: lasers are *everywhere*. Since the onset of laser technology the ability to control the structure and properties of such high intensity light beams has been vital in many optical application and devices and continues to this day to attract a lot of interest in various research areas. The control of the structure of the light is important in understanding how light will interact with nonlinear medium.

In this work we will focus on some of the nonlinear processes mentioned and describe some of the emergent phenomena that arise when we consider the interaction of high intensity laser modes of various structures with nonlinear media. In particular we aim to show control over the structure of the properties of such light modes for example intensity, phase and polarisation both with propagation within nonlinear media and within a resonant optical cavity.

In Chapter 2 some of the background material detailing some of the forms of light used in the main chapters is given. Firstly a derivation of the nonlinear Scrödinger equation or wave equation for the nonlinear propagation of light is given. This equation is used as the starting point for the derivation of the numerical models used in each of the chapters, by changing the form of the nonlinear polarisation term for each of the cases considered. We then give the forms of light that are used in the numerical simulations which give linear solutions to the wave equation when the nonlinear term is neglected and analyse the structure of each solution. We give the mathematical form of plane waves which has no structure in its properties, Gaussian beams structured in their intensity, Laguerre-Gauss modes structured in intensity and phase and finally fully structured light or vector beams for which all of its properties are spatially structured in the transverse plane; intensity, phase and polarisation.

In Chapter 3 we consider a second order ($\chi^{(2)}$) crystal in a singly resonant optical parametric oscillator with an external forcing field. By decreasing the intensity of the injected field we observe a bifurcation from stationary self-organising hexagonal patterns to a dynamic turbulent state that is driven by the presence of optical defects with integer orbital angular momentum (OAM) ± 1. Such vortices are associated with the production of helical waves. Interactions between pairs of optical vortices of opposite OAM results in the emergence of very high intensity peaks in the transverse field which are the optical equivalent of rogue waves that are discussed in oceanography and hydrodynamics. We characterise the behaviour of the defect mediated turbulent state and statistically analyse the optical rogue waves to show the parameter regimes where such extreme events could be studied experimentally.

In Chapter 4 we detail the behaviour of fully structured light (FSL) - a vector superposition of two scalar Laguerre-Gauss (LG) modes with orthogonal polarisations - as it propagates through a nonlinear Kerr ($\chi^{(3)}$) medium. We focus on the rotation of the polarisation structure in the transverse profile of the beam during both linear and nonlinear propagation. In the linear case it is shown that the rotation and behaviour of the polarisation is uniform across the field and dependent purely on the difference in Gouy phase between the two LG beams within the superposition. When nonlinear propagation is considered the self-focussing from the Kerr effect causes a change in spatial overlap between the modes. This in turn changes the cross-phase modulation and interaction between the modes such that the rotation becomes complex. We show the mechanisms that contribute to the nonlinear rotation of the polarisation and compare the linear and nonlinear cases. By understanding which mechanisms contribute to the evolution of the behaviour of FSL during nonlinear propagation we show that we can control the spatial intensity and polarisation distribution by balancing key parameters to control the properties of the light modes.

Finally in Chapter 5 we analyse the propagation of fully structured light in a vectorial Kerr cavity where the intensity is above Turing instability threshold and in particular focus on the rotational behaviour of the ring structure. We first consider the scalar case

in one dimension using the well known Lugiato-Lefever model where analytical solutions are possible and calculate that the angular velocity at which the Turing pattern rotates is dependent on the OAM of the mode and the radius from the centre of the mode. We compare this result with the scalar 2D case both for Laguerre-Gauss modes and top-hat shaped beams with an azimuthal phase. In the top-hat case we note that the individual rings of the Turing pattern rotate independently at the rotational velocity calculated analytically from the Lugiato-Lefever analysis. Finally we consider the full vector case composed of two Laguerre-Gauss modes of orthogonal polarisations which is no longer trivial and analytical. The cross phase modulation between the modes as well as the changing spatial overlap between the modes for different compositions means that the rotational rate of the Turing pattern is complex. We consider the cases where the OAM is equal and opposite, and by changing the bias (relative intensity) between the two modes and show how control over the bias can control the angular velocity of the ring structure. Finally we detail cases for fully structured light where the spatial overlap between the two modes is small such that the cross phase modulation between the beams is negligible. In such a case by changing the beam width and OAM of each mode we can completely control the rotational rate of each ring structure such that they rotate independently and can even rotate in opposite directions.

Chapter 2

Background Theory

2.1 Introduction

As the topics of this research focus on the propagation of structured light in nonlinear media and interactions within optical cavities we want to first give a brief description of how these modes of light are created and understood from a mathematical viewpoint and detail their fundamental properties. In this chapter we will look at the classical theory of electromagnetism from a wave standpoint and derive a wave equation from Maxwell's equations that all modes of light must obey. Gaussian beams structured in their intensity are shown to be a solution to the wave equation and satisfy Maxwell's equations. Higher order Gaussian beams, such as Laguerre-Gauss (LG) modes, are also known to solve the wave equation and we detail that they are structured not only in their intensity but also in their phase across the transverse plane. We also show the helical wavefronts associated with such modes of light. Finally we show with a vector superposition of two of these LG modes we can create fully structured light (FSL) where the novelty is that we can completely structure all of lights properties across the transverse beam - intensity, phase *and* polarisation - and tailor each of them to suit a variety of requirements.

2.2 The Paraxial Wave Equation

2.2.1 Maxwell's Equations

From a classical point of view light propagates as waves in the electromagnetic field which can be thought of as two vector fields throughout all of space that describe the state of both the electric field and the magnetic field respectively [15]. The fields can interact such that changes in one influence the behaviour and state of the other and the interplay between these interactions results in oscillating fields that can propagate. These interactions and oscillations are governed by Maxwell's equations, our starting point for deriving a wave equation that supports the idea of light propagating as a wave. Maxwell's equations are a set of partial differential equations that form the foundation of modern electromagnetism, classical optics and electrical circuits. Not only do Maxwell's equations describe how electric fields are generated from charges and currents but also fully describe how each field affects the other. For a generalised medium which supports free charges and currents they are given by [16].

$$\nabla \cdot \mathbf{D}(\mathbf{r}, t) = \rho(\mathbf{r}, t), \tag{2.1}$$

$$\nabla \cdot \mathbf{B}(\mathbf{r}, t) = 0, \tag{2.2}$$

$$\nabla \times \mathbf{E}(\mathbf{r}, t) = -\frac{\partial \mathbf{B}(\mathbf{r}, t)}{\partial t}, \tag{2.3}$$

$$\nabla \times \mathbf{H}(\mathbf{r}, t) = \frac{\partial \mathbf{D}(\mathbf{r}, t)}{\partial t} + \mathbf{J}(\mathbf{r}, t), \tag{2.4}$$

where $\mathbf{E}$ denotes the electric field, $\mathbf{H}$ is the magnetic field, $\mathbf{D}$ is the electric displacement field, $\mathbf{B}$ is the magnetic induction, ρ and $\mathbf{J}$ are the free charge and current densities respectively. For aesthetics and simplicity the functional dependence of the relevant vectors on space and time will be dropped from the notation where relevant. The constitutive relationships between the electric and magnetic fields with their respective displacement fields are [16],

$$\mathbf{D} = \varepsilon_0 \mathbf{E} + \mathbf{P}, \tag{2.5}$$

$$\mathbf{B} = \mu_0 \mathbf{H} + \mathbf{M}, \tag{2.6}$$

where $\mathbf{P}$ and $\mathbf{M}$ are the induced polarisation and magnetisation within the medium, ε_0 and μ_0 are the permittivity and permeability of free space respectively. The induced polarisation and magnetisation in turn are related directly to the electric and magnetic fields and for a generalised medium can be expanded and written as a power series in terms of the respective fields as [17]

$$\begin{aligned} \mathbf{P} &= \varepsilon_0 \left[\chi_e^{(1)} \mathbf{E} + \chi_e^{(2)} \mathbf{E}^2 + \chi_e^{(3)} \mathbf{E}^3 \, ..\right] \\ &= \varepsilon_0 \chi_e^{(1)} \mathbf{E} + \mathbf{P}^{NL} \qquad (2.7) \\ \mathbf{M} &= \mu_0 \chi_m^{(1)} \mathbf{H} \qquad (2.8) \end{aligned}$$

where $\chi_{e,m}^{(1)}$ is the linear electric and magnetic susceptibilities, $\chi_e^{(2)}$ and $\chi_e^{(3)}$ are referred to as the second and third order nonlinear electric susceptibilities, where all terms in χ relate the relative amplitudes of the electric and magnetic fields with that of the induced polarisation and magnetisation. The linear and nonlinear contributions to the induced polarisation have been separated into two separate terms for convenience where the nonlinear polarisation has been defined as a vector $\mathbf{P}^{NL}$ that contains all the higher order nonlinear susceptibilities and higher order terms of the fields. We can substitute the expressions for $\mathbf{P}$ and $\mathbf{M}$ from Eq(2.7) and Eq(2.8) into the relationships in Eq(2.5) and Eq(2.6) to obtain the full relationship between the electric and magnetic fields with their displacement fields which we can now write as

$$\begin{aligned} \mathbf{D} &= \varepsilon_0 \left(1 + \chi_e^{(1)}\right) \mathbf{E} + \mathbf{P}^{NL} \\ &= \varepsilon_0 \varepsilon_r \mathbf{E} + \mathbf{P}^{NL} \end{aligned} \tag{2.9}$$

$$\begin{aligned} \mathbf{B} &= \varepsilon_0 \left(1 + \chi_m^{(1)}\right) \mathbf{H} \\ &= \mu_0 \mu_r \mathbf{H} \end{aligned} \tag{2.10}$$

where $\varepsilon_r = 1 + \chi_e^{(1)}$ and $\mu_r = 1 + \chi_m^{(1)}$ are the relative permittivity and permeability of the medium respectively.

2.2.2 The Wave Equation

Now that we have a full set of descriptions for each field and their relationships with each other we are ready to make some assumptions on the medium. Firstly that there are no free charges such that $\rho = 0$ which implies that there are also no current densities and $\mathbf{J} = 0$. We also assume a non-magnetic medium which greatly simplifies Maxwell's equations and the constituent relations. In order to form a wave equation from Maxwell's equations we first take the curl of Maxwell III in Eq(2.3), substitute in Maxwell IV in Eq(2.4) and finally substitute in the relationships in from Eq(2.9) and Eq(2.10) to derive the well known wave equation for a complex electric field in a medium as follows [17]

$$\begin{aligned} \boldsymbol{\nabla} \times \boldsymbol{\nabla} \times \mathbf{E} &= -\frac{\partial}{\partial t} \left(\boldsymbol{\nabla} \times \mathbf{B}\right) \\ &= -\mu_0 \mu_r \frac{\partial^2 \mathbf{D}}{\partial t^2} \\ &= -\mu_0 \mu_r \varepsilon_0 \varepsilon_r \frac{\partial^2 \mathbf{E}}{\partial t^2} - \mu_0 \mu_r \frac{\partial^2 \mathbf{P}^{NL}}{\partial t^2} \end{aligned} \tag{2.11}$$

We can simplify the term on the left hand side of the wave equation using the vector calculus identity,

$$\boldsymbol{\nabla} \times \boldsymbol{\nabla} \times \mathbf{V} = \boldsymbol{\nabla} (\boldsymbol{\nabla} \cdot \mathbf{V}) - \nabla^2 \mathbf{V} \tag{2.12}$$

and consider that in the medium the relation $\boldsymbol{\nabla} (\boldsymbol{\nabla} \cdot \mathbf{E}) \approx 0$ which Boyd gives arguments is true for most nonlinear optical media particularly for the case of paraxial beams [17]. The left hand side of Eq(2.11) then becomes $-\nabla^2 \mathbf{E}$. We now also assume that the medium is non-magnetic such that the relative permeability of the medium $\mu_r = 1$ (which is true for most media at optical frequencies) and introduce the relationships $n_0^2 \equiv \varepsilon_r$ and $\mu_0 \varepsilon_0 = 1/c^2$ such that we can fully simplify and re-write the wave equation as

$$\nabla^2 \mathbf{E} - \left(\frac{n_0}{c}\right)^2 \frac{\partial^2 \mathbf{E}}{\partial t^2} = \frac{1}{\varepsilon_0 c^2} \frac{\partial^2 \mathbf{P}^{NL}}{\partial t^2} \tag{2.13}$$

where n_0 is the linear refractive index. We have also rearranged the equation such that the linear contributions are on the left and the nonlinear contribution on the right of the equation.

2.2.3 Slowly Varying Amplitude and Paraxial Approximation

Now consider that we set the axes such that the electric field propagates parallel to the z-axis and we can split the diffraction operator on the left hand side of Eq(2.13) into its components that are parallel and perpendicular with the direction of propagation as

$$\begin{aligned} \nabla^2 &= \frac{\partial^2}{\partial x^2} + \frac{\partial^2}{\partial y^2} + \frac{\partial^2}{\partial z^2} \\ &= \nabla_\perp^2 + \frac{\partial^2}{\partial z^2}, \end{aligned} \tag{2.14}$$

where $\nabla_{\perp}^2$ is the Laplacian in the transverse plane. Under the slowly varying amplitude approximation we assume that the amplitude of each of the fields vary by a small amount in both time and along the z-directions. If the fields remain propagating parallel to the z-axis this assumption allows us to decompose the fields into rapidly and slowly oscillating terms. We can write the full form of the fields as the product of a wave envelope which gives a spatially dependent amplitude and a rapidly oscillating propagator which has the form of a simple plane wave where we make no assumption on the form of the spatially varying amplitude

$$\begin{aligned} \mathbf{E}(\mathbf{r},t) &= \mathbf{A}(\mathbf{r},t)\exp\left[i(k_e z-\omega t)\right]+c.c., && (2.15)\\ \mathbf{P}^{NL}(\mathbf{r},t) &= \mathbf{P}(\mathbf{r},t)\exp\left[i(k_p z-\omega t)\right]+c.c.. && (2.16) \end{aligned}$$

In general the wave numbers of the electric field, k_e, and the polarisation, k_p, can be different. However for simplicity here we only consider cases where the difference in wave number is negligible such that

$$\begin{aligned} \Delta k &= k_e - k_p \approx 0,\\ \Rightarrow k &= k_e = k_p. && (2.17) \end{aligned}$$

We can now substitute the form of the electric and polarisation fields from Eq(2.15) and Eq(2.16) with the assertion in Eq(2.17) into the wave equation in Eq(2.13) and calculate the respective derivatives as

$$\frac{\partial}{\partial z}\mathbf{A}(\mathbf{r},t)\mathrm{e}^{i(kz-\omega t)} = \mathrm{e}^{i(kz-\omega t)}\left[\frac{\partial \mathbf{A}}{\partial z} + ik\mathbf{A}\right], \tag{2.18}$$

$$\frac{\partial^2}{\partial z^2}\mathbf{A}(\mathbf{r},t)\mathrm{e}^{i(kz-\omega t)} = \mathrm{e}^{i(kz-\omega t)}\left[\frac{\partial^2 \mathbf{A}}{\partial z^2} + 2ik\frac{\partial \mathbf{A}}{\partial z} - k^2\mathbf{A}\right], \tag{2.19}$$

$$\frac{\partial}{\partial t}\mathbf{A}(\mathbf{r},t)\mathrm{e}^{i(kz-\omega t)} = \mathrm{e}^{i(kz-\omega t)}\left[\frac{\partial \mathbf{A}}{\partial t} - i\omega\mathbf{A}\right], \tag{2.20}$$

$$\frac{\partial^2}{\partial t^2}\mathbf{A}(\mathbf{r},t)\mathrm{e}^{i(kz-\omega t)} = \mathrm{e}^{i(kz-\omega t)}\left[\frac{\partial^2 \mathbf{A}}{\partial t^2} - 2i\omega\frac{\partial \mathbf{A}}{\partial t} - \omega^2\mathbf{A}\right], \tag{2.21}$$

$$\frac{\partial^2}{\partial t^2}\mathbf{P}(\mathbf{r},t)\mathrm{e}^{i(kz-\omega t)} = \mathrm{e}^{i(kz-\omega t)}\left[\frac{\partial^2 \mathbf{P}}{\partial t^2} - 2i\omega\frac{\partial \mathbf{P}}{\partial t} - \omega^2\mathbf{P}\right], \tag{2.22}$$

such that the wave equation becomes

$$\nabla_\perp^2\mathbf{A} + \frac{\partial^2 \mathbf{A}}{\partial z^2} + 2ik\frac{\partial \mathbf{A}}{\partial z} - k^2\mathbf{A} + \frac{n_0^2}{c^2}\frac{\partial^2 \mathbf{A}}{\partial t^2} + \frac{2i\omega n_0^2}{c^2}\frac{\partial \mathbf{A}}{\partial t} + \frac{n_0^2\omega^2}{c^2}\mathbf{A} \tag{2.23}$$

$$= \frac{1}{\varepsilon_0 c^2}\frac{\partial^2 \mathbf{P}}{\partial t^2} - \frac{2i\omega}{\varepsilon_0 c^2}\frac{\partial \mathbf{P}}{\partial t} - \frac{\omega^2}{\varepsilon_0 c^2}\mathbf{P}. \tag{2.24}$$

Now we can make use of the linear dispersion relation which is given by

$$k^2 = \frac{n_0^2\omega^2}{c^2} \tag{2.25}$$

for the wave number in the medium. It is evident that this substitution leads to the fourth and seventh terms on the left hand side of the wave equation cancelling. Furthermore by assuming that the beams remain paraxial during propagation such that the beam varies slowly along the propagation axis and the angle between the wave vector and the x-axis is small, we can make use of the paraxial approximation which implies

$$\left|\frac{\partial^2 \mathbf{A}}{\partial t^2}\right| \ll \omega \left|\frac{\partial \mathbf{A}}{\partial t}\right| \quad ; \quad \left|\frac{\partial^2 \mathbf{A}}{\partial z^2}\right| \ll k \left|\frac{\partial \mathbf{A}}{\partial z}\right|, \tag{2.26}$$

$$\left|\frac{\partial^2 \mathbf{P}}{\partial t^2}\right| \ll \omega \left|\frac{\partial \mathbf{P}}{\partial t}\right| \ll \omega \left|\frac{\partial \mathbf{A}}{\partial t}\right| \quad \text{since} \quad |\mathbf{A}| \gg |\mathbf{P}|, \tag{2.27}$$

such that we can also neglect the terms that are very small with respect to the others such that we can finally write the full paraxial wave equation, or nonlinear Schrödinger equation as an inhomogeneous partial differential equation

$$\nabla_\perp^2 \mathbf{A} + 2ik\left[\frac{\partial \mathbf{A}}{\partial z} + \frac{n}{c}\frac{\partial \mathbf{A}}{\partial t}\right] = -\frac{\omega^2}{\varepsilon_0 c^2}\mathbf{P}. \tag{2.28}$$

2.3 Unstructured Light - Plane waves

In order to find laser mode beam-like solutions to Maxwell's equations we must solve the paraxial wave equation in Eq(2.28). First we make a simplification that we are considering vacuum or linear homogeneous media such that there is no nonlinear polarisation response of the medium and we can set the term on the right hand side of the equation to 0. This simplification gives a homogeneous partial differential equation and the paraxial wave equation for a linear medium is then

$$\nabla_\perp^2 \mathbf{A} + 2ik\frac{\partial \mathbf{A}}{\partial z} = 0. \tag{2.29}$$

The trivial solution to Eq(2.29) is that the amplitude of the electric field is a constant such that $\mathbf{A}(\mathbf{r}) = A_0$ which gives the simple idealistic case of a plane wave with the form

$$\mathbf{E}(\mathbf{r}, t) = A_0 \exp[i(kz - \omega t + \varphi)]. \tag{2.30}$$

where we have added a relative phase shift φ that describes the phase of each given plane wave. Such a solution can be verified by simply substituting into Eq(2.29) and see that it satisfies the paraxial wave equation. Assuming that the dispersion as in Eq(2.25) holds then it is also known to be a solution to the full wave equation. The plane wave is the simplest known solution and has simple characteristics in that the amplitude is constant and the wavefronts are a set of infinite parallel planes. Although the simplest of solutions, plane waves can be used to model light at a great distance from a localised source where the approximation is valid, such as radio waves. However such a solution is clearly unphysical as the wave spans all of space. For modelling optical interactions with media we clearly require light that is spatially structured with parameters that we can control.

2.4 First Layer of Structure - Intensity and Gaussian Beams

We can begin to structure the light modes by multiplying the field amplitude by terms that scale the intensity such that it is localised in the transverse plane. One such mode of light is the well known and widely used Gaussian beam which is given by

$$\mathbf{E}(r,z) = E_0 \frac{w_0}{w(z)} \exp\left[-\frac{r^2}{w^2(z)}\right] \exp\left[-i\frac{kr^2}{2R(z)}\right] \exp\left[-i(kz-\eta(z)\right], \tag{2.31}$$

where E_0 is the amplitude, $r = \sqrt{x^2+y^2}$ is the radius from the centre of the beam, w_0 is the beam waist which defines the physical size of the beam, R(z) is the radius of curvature which will be defined later, and $\eta(z)$ is the Gouy phase which will also be fully defined. For a full derivation of the Gaussian beam see [18], here we are only interested in the properties of the Gaussian beam and how we can use it to model lasers in physical systems.

Figure(2.1) shows both the transverse intensity of a typical Gaussian beam as well as the phase distribution across the transverse plane. It can be seen that the peak intensity

occurs in the very centre of the mode and the intensity decreases in a well defined manner as the radius from the centre increases. The particular shape of the drop of in intensity with increasing radius is a characteristic shape of Gaussian statistics. In order to better visualise this structure in the transverse plane a cut through the centre of the Gaussian mode is given in Figure(2.2) to show the change in intensity across the transverse intensity with changing radius. We can also see from Figure(2.1) that the phase is homogeneous across the transverse plane. The colour bars will be omitted for future transverse plots but the yellow/blue scale defined for intensity and the rainbow scale defined for phase will be the scale used for all of the images presented.

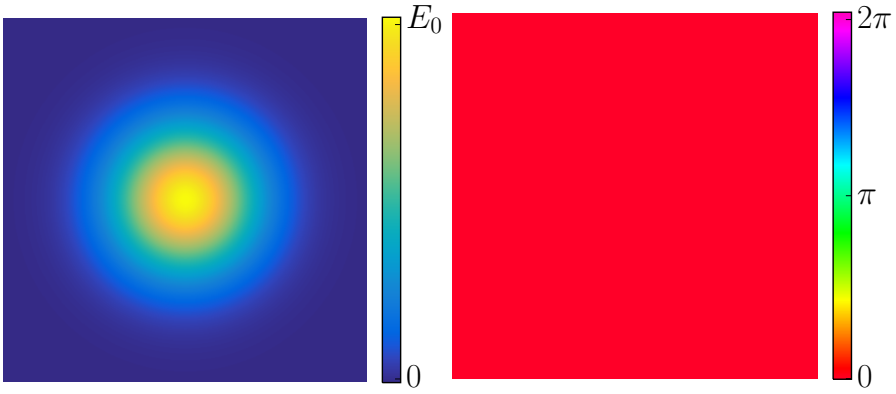

FIGURE 2.1: Left - Transverse intensity profile of a Gaussian beam. Right - Transverse phase profile of the corresponding Gaussian beam.

Some important parameters well define the Gaussian beam and its behaviour during propagation. The Rayleigh length or Rayleigh range is defined as [19]

$$z_R = \frac{\pi w_0^2}{\lambda} \tag{2.32}$$

and gives the distance at which the radius of the beam increases by a factor $\sqrt{2}$ due to diffraction. It also defines the depth of focus of the beam. We will later use the Rayleigh range to define propagation distance for a given beam which is very useful in comparing the difference in behaviour for beams that have different Rayleigh lengths. The radius of curvature R(z) is defined in terms of the Rayleigh range as [19]

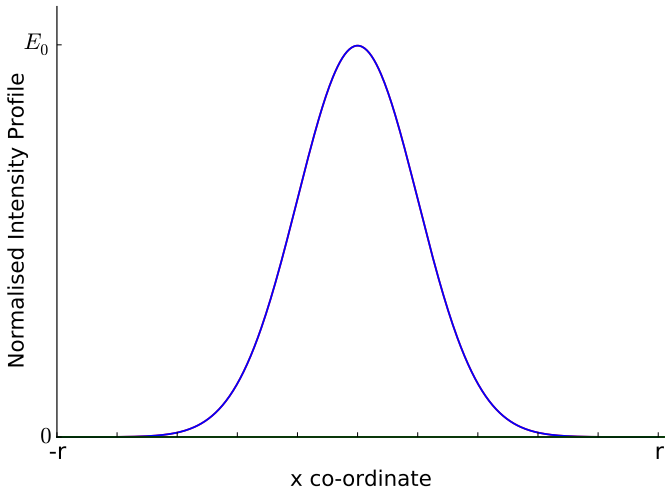

FIGURE 2.2: Cross-section of a Gaussian beam through the centre of the beam where the intensity is normalised such that the peak occurs at E_0 in Eq(2.31) and r is the radius from the centre of the beam.

$$R(z) = z + \frac{z_R^2}{z} \tag{2.33}$$

and gives the curvature of the planes of equal phase, known as wavefronts. In the plane wave case the wavefronts are parallel and separated by the wavelength λ, however in the Gaussian beam case due to diffraction and evolving phase the wavefronts are curved and defined by R(z). Finally, the Gouy phase $\eta(z)$ is given by [19]

$$\eta(z) = tan^{-1}\left(\frac{z}{z_R}\right) \tag{2.34}$$

which gives the extra phase shift acquired by a Gaussian beam during propagation over a plane wave of the same frequency.

Figure(2.3) shows the evolution of the Gouy phase as a function of propagation distance from $-10z_R$ through the beam focus to $10z_R$. It can be seen that the Gouy phase asymptotes as it is described by the inverse tangent function which also asymptotes. The phase change happens within a region of $\pm z_R$ around the beam waist and as such is not experimentally visible, however forms an important part of the numerical theory

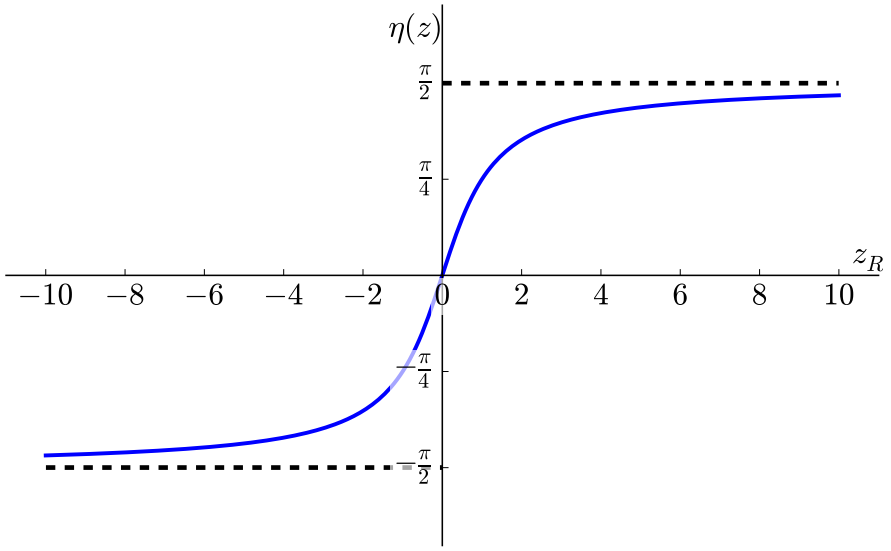

FIGURE 2.3: Evolution of the Gouy phase for a Gaussian beam with propagation distance from $z = -10z_R$ through the beam waist to $z = 10z_R$.

involving such modes of light. The Gouy phase extends over a wider range in higher order modes described in the next section where it can be observed in experimental set ups [20].

2.5 Second Layer of Structure - Phase and Laguerre-Gauss Modes

There are a variety of higher order modes that are eigensolutions to the paraxial wave equation in Eq(2.29) such as the Hermite-Gauss in Cartesian co-ordinates and the Laguerre-Gauss modes in cylindrical co-ordinates [19, 21]. Such solutions form complete orthogonal basis sets and as such can describe a wide array of paraxial light beams and reduce to the Gaussian solution described previously at the fundamental lowest order mode [22]. For the considerations in this thesis we focus on the Laguerre-Gauss modes which have cylindrical symmetry and have a doughnut shaped intensity structure. The Laguerre-Gauss basis can be derived by solving the paraxial wave equation in cylindrical co-ordinates and are given by [23]

$$\begin{aligned}\mathbf{LG}_p^{\ell}(r,\phi,z) =& \sqrt{\frac{2p!}{\pi(p+|\ell|)!}}\frac{1}{w(z)}\left(\frac{r\sqrt{2}}{w(z)}\right)^{|\ell|} L_p^{|\ell|}\left(\frac{2r^2}{w^2(z)}\right)\exp\left(\frac{-r^2}{w^2(z)}\right) \\ &\times \exp\left(i\ell\phi\right)\exp\left(\frac{ikr^2 z}{2(z^2+z_R^2)}\right)\exp\left(-i(2p+|\ell|+1)\eta(z)\right)\end{aligned} \tag{2.35}$$

where r, $w(z)$ and $\eta(z)$ are as defined in the Gaussian case, and the modes are labelled by two integers the azimuthal index, ℓ and the radial index p and $L_p^{|\ell|}$ are the generalised Laguerre polynomials. There is a constraint on the radial index such that $p \geq 0$ and for the case $l = p = 0$ the fundamental Gaussian beam is obtained. The azimuthal index is crucial in defining the Laguerre-Gauss mode as it controls both the shape of the amplitude factors, the Laguerre polynomials and most importantly the phase factor in the $\exp(i\ell\phi)$ term as well as in the Gouy phase term. The phase is therefore purely dependent on the azimuthal index and ℓ gives the number of 2π phase rotations around the azimuthal direction in the transverse plane. As the phase is undefined in the centre of the beam this means the intensity must be zero and hence the Laguerre-Gauss modes are examples of optical vortices [24]. This gives the Laguerre-Gauss modes their characteristic doughnut intensity profile and as such ℓ can be associated with the orbital angular momentum (OAM) of the beam [25]. As such we will refer to ℓ interchangeably as the azimuthal index or the OAM of a given Laguerre-Gauss mode.

Figure(2.4) shows the transverse intensity profile for some of the lowest order modes as well as the phase across the transverse plane. We can see that the lowest order mode for $\ell = 0$ is the fundamental Gaussian mode as shown in Figure(2.1). For $|\ell| > 0$ we see the characteristic doughnut intensity profile, and with increasing OAM the mode becomes larger. The radius of the peak intensity of the ring is given by $r_{peak} = w_0\sqrt{|\ell|/2}$. Laguerre-Gauss modes of equal magnitudes of OAM but opposite polarity have identical intensity structures due to the cylindrical symmetry of the beams, however we can see in Figure(2.4) that the phase distribution evolves in the opposite azimuthal direction and it is clear that the azimuthal number ℓ gives the number of times that the phase completes a full rotation of 0 to 2π.

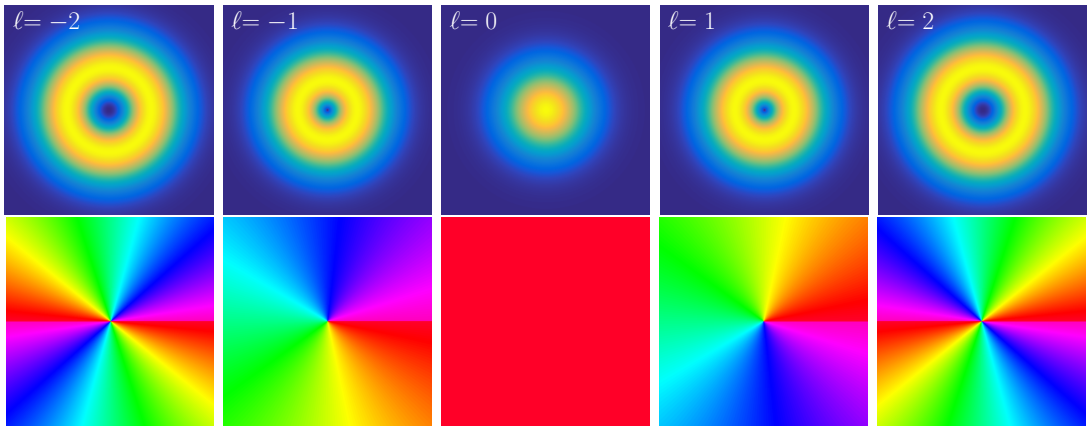

FIGURE 2.4: Top row - Transverse intensity profiles for Laguerre-Gauss modes of various OAM given in the respective images. Bottom row - Transverse phase profiles for the corresponding Laguerre-Gauss modes.

The OAM therefore gives the number of times the field is advanced (or in the case of negative OAM retarded) by a phase of 2π. Each of the phase dislocations in the transverse plane shows where a new wavefront begins and since these rotate around the azimuthal direction Laguerre-Gauss modes are associate with helical wavefronts as shown in Figure(2.5). Here we have omitted $\ell \leq 0$ but for clarity the wavefronts simply rotate in the opposite direction when the OAM has the opposite polarity just as in the case for the phase.

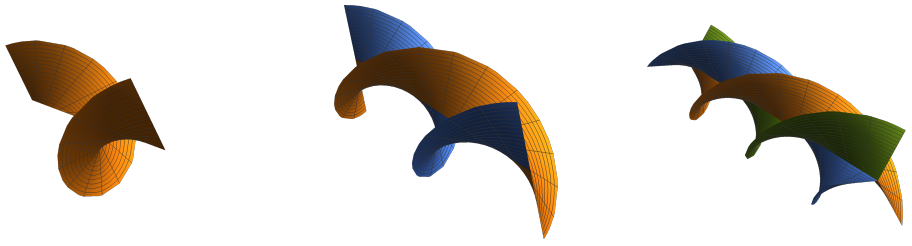

FIGURE 2.5: Helical wavefronts for the three lowest order Laguerre-Gauss modes $\ell = 1, 2, 3$ from left to right respectively. The wavefronts are coloured for a more clear view of the separate fronts for the different values of OAM.

We can also see from the form of the Laguerre-Gauss mode in Eq(2.35) there is a change in the evolution of the Gouy phase as the beam propagates and the magnitude of the change in phase is multiplied by a factor $(|\ell| + 2p + 1)$. The phase evolution for a

Laguerre-Gauss mode is therefore dependent on the value of OAM. For the same modes as shown in Figure(2.4) we show how the Gouy phase evolves with propagation from $-10z_R$ through the beam waist to $10z_R$ in Figure(2.6). We calculate this analytically later in Chapter 4.

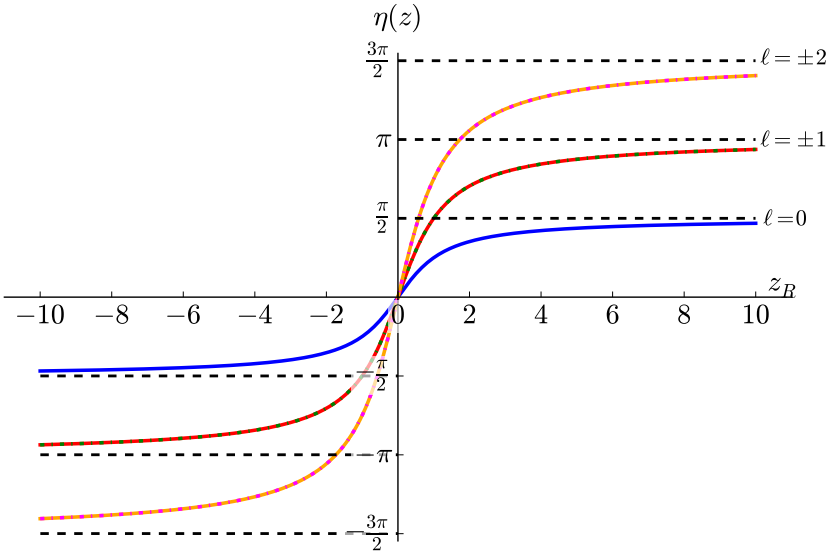

FIGURE 2.6: Evolution of the Gouy phase for Laguerre-Gauss modes composed of $\ell = 0$ (Gaussian beam as in Figure(2.3)), $\ell = \pm 1$ (red and green dashed lines) and $\ell = \pm 2$ (magenta and orange dashed lined) for propagation from $z = -10z_R$ through the beam waist to $z = 10z_R$. The dashed black horizontal lines represent the asymptotes for each respective curve.

The effect of the radial index, p, on the transverse intensity and phase of a Laguerre-Gauss beam is shown in Figure(2.7). The top row shows the transverse intensity for an OAM of $\ell = 2$ where it can be observed that there are $p + 1$ concentric intensity rings. As the radius from the central vortex increases the intensity of each ring decreases. Although omitted here we note that in the case where the OAM has the opposite polarity the intensity structure is identical for a given value of p such that the intensity is only dependent on the magnitude of the OAM as in Figure(2.4). The bottom row gives the corresponding phase distribution where it can be seen that there are p rings of phase discontinuities where a phase jump of $\pi/2$ occurs. These discontinuities occur at the rings of zero intensity in the intensity distribution. Again as in Figure(2.4) we note that for an OAM of opposite polarity the phase simply evolves in the opposite

direction. For the work in this thesis we mainly focus on the case where the radial index $p = 0$, but have included a description of its effects here.

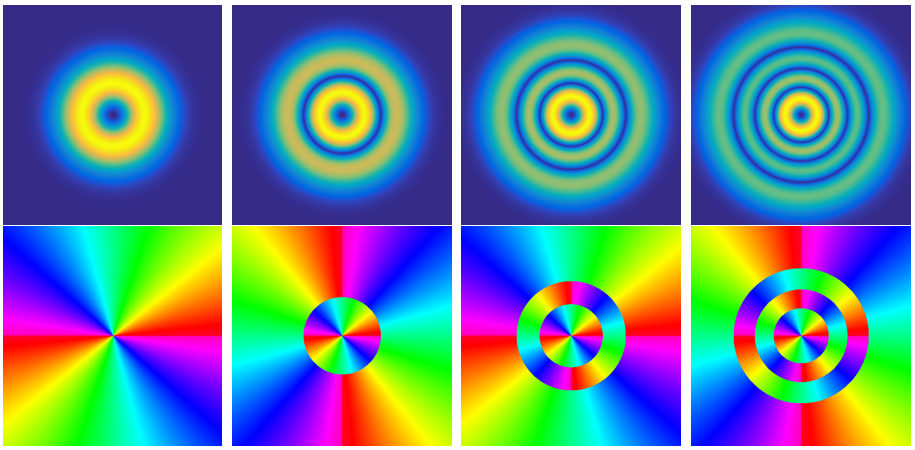

FIGURE 2.7: Transverse intensity (top row) and phase (bottom row) for Laguerre-Gauss beams with $\ell = 2$ for radial modes where $p = 0, 1, 2$ and 3 from left to right respectively.

2.6 Third layer of Structure - Polarisation and Fully Structured Light

Aside from intensity and phase, polarisation is an important property of light that defines the direction of oscillations in the electromagnetic field. For fully polarised light, these oscillations occur along a single plane and such forms of light have been extensively studied for uniform distributions where the light has a single form of of polarisation. For example; horizontal polarisation where the electric field vectors oscillate in the horizontal plane or circularly polarised light where the electric field vectors rotate in a circle at a constant rate. These states of polarisation are homogeneous across the transverse plane; the polarisation is the same at every point of the beam and does not depend on spatial location. Phenomena involving polarised light has lead to a wide variety of applications from simplistic ideas like sunglasses to complex techniques involving astronomical measurements [26]. A common use of polarisation technology everyone has experienced involves the production of 3D movies and television, which

is actually two sets of running pictures where the images are recorded from two different angles. Each of the sets of images are produced and emitted from the screen with orthogonal polarisations (light carrying each picture oscillates in perpendicular directions). The glasses are two polarising filters that only allow light that oscillates in certain directions through, and since the pictures carry orthogonal polarisations each eye only receives the image of one picture and the brain interprets this information and creates a 3 dimensional picture, a phenomena known as stereoscopic vision. More complex polarisation ideas have been used in a wide array of devices and techniques from liquid crystal display and data storage [27]. In more recent times, there has been increasing research interest into modes of light where the polarisation is no longer homogeneous across the field but is spatially dependent and varies across the transverse plane [28, 29]. The ability to tailor and control the state of polarisation across a beam to any desired distribution both allows another level of structure to light and the emergence and understanding of new phenomena for the advancement of optical techniques and devices [30].

2.6.1 Form of Fully Structured Light

Cylindrical vector beams (CVBs) or more generally fully structured light (FSL) beams are examples of modes of light that are characterised by spatially structured intensity, phase and most importantly polarisation; all of the properties of light are inhomogeneous across the transverse plane [30]. Such modes of light are composed of a vector superposition of two distinct scalar beams with orthogonal polarisation states. Any orthogonal polarisation basis can be chosen to define the beams for example vertical/horizontal for linear polarisation or left/right handed circular polarisation for circularly polarised beams etc. Here and for the remainder of the work discussing FSL we adopt the circular basis for defining the states of polarisation of the light. The circular basis is defined such that the unit vectors are given by

$$\mathbf{e}_R = \frac{\mathbf{x} - i\mathbf{y}}{\sqrt{2}}, \tag{2.36}$$

$$\mathbf{e}_L = \frac{\mathbf{x} + i\mathbf{y}}{\sqrt{2}}, \tag{2.37}$$

where $\mathbf{x}, \mathbf{y}$ are the unit Cartesian co-ordinate vectors. The transverse field of any FSL beam can be decomposed and written in terms of its right and left circular components as [12]

$$\begin{aligned} \mathbf{E} &= \mathbf{E}_R + \mathbf{E}_L \\ &= \sin(\gamma)\mathbf{LG}_{p_R}^{\ell_R}\mathbf{e}_R + e^{i\beta}\cos(\gamma)\mathbf{LG}_{p_L}^{\ell_L}\mathbf{e}_L, \end{aligned} \tag{2.38}$$

where $0 \geq \gamma \geq \frac{\pi}{2}$ controls the relative amplitudes of the two beams, LG_p^ℓ are the Laguerre-Gauss modes from Eq(2.35) with OAM ℓ_R and ℓ_L, radial number p_R and p_L respectively, $\mathbf{e}_{R,L}$ are the right and left circular polarisation vectors and $0 \geq \beta \geq 2\pi$ is the relative phase between the modes. By controlling the various given parameters such as the relative amplitude, OAM and phase difference between each mode of the superposition a rich variety of intensity and polarisation distributions can be tailored and controlled. CVBs are a specific subset of the more general FSL whereby the intensity and polarisation distributions are axially symmetric and have the same value of OAM for the right and left circularly polarised modes ($|\ell_R| = |\ell_L|$). CVBs carry only linear polarisation whereas FSL carries all states of polarisation [28].

2.6.2 Stokes Parameters and the Polarisation Ellipse

Intensity and phase are trivial to represent in the transverse plane using colour gradients as shown in Figure(2.1) and Figure(2.4). However since polarisation and its behaviour during propagation are of particular interest when studying FSL a method

of visualising the state of the polarisation at each point in the field is required on top of presenting the intensity and phase. The Stokes parameters are the four components of the Stokes vector which completely define the state of polarisation of light for any degree of polarisation. In our case we only consider fully polarised states of light such that the Stokes parameters are defined as [18]

$$S_0 = I, \tag{2.39}$$

$$S_1 = S_0 \cos 2\chi \cos 2\psi, \tag{2.40}$$

$$S_2 = S_0 \cos 2\chi \sin 2\psi, \tag{2.41}$$

$$S_3 = S_0 \sin 2\chi, \tag{2.42}$$

where χ and ψ are directly related to the helicity and orientation of the polarisation ellipse respectively. The polarisation ellipse is shown in Figure(2.8) which denotes how the angles χ and ψ define the polarisation state at a particular point of the transverse field and b is the semi-axis of the ellipse. The angle ψ gives the orientation of the ellipse and χ defines how elliptical it is. In physical terms this defines the direction of oscillations of the fields and how circularly polarised a given point of the beam is. By colouring the ellipse according to the handedness of the polarisation we can also indicate whether a particular point is right/left circularly polarised.

However, the parameters χ and ψ are not measurable physical properties of a light beam. For a fixed choice of basis the Stokes parameters can also be defined in terms of the components of the vector superposition. As discussed above we select the circular basis which is defined in Eq(2.36) and Eq(2.37) for which the Stokes parameters can be written as [12]

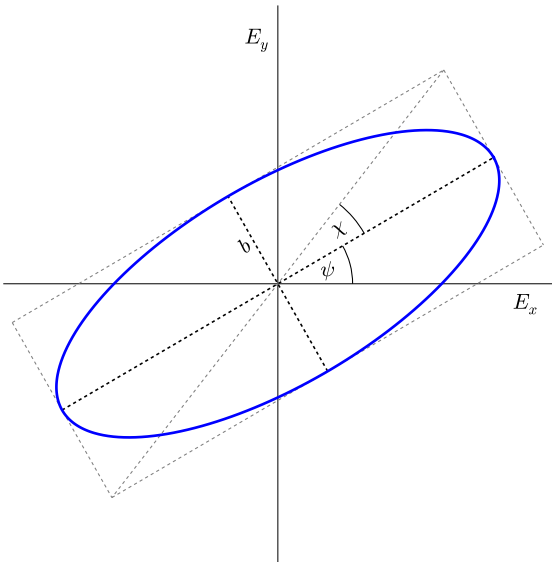

FIGURE 2.8: A polarisation ellipse defined in terms of ψ and χ from the Stokes parameters showing the polarisation of an electric field at a given point.

$$S_0 = I = |\mathbf{E}_R|^2 + |\mathbf{E}_L|^2 , \tag{2.43}$$

$$S_1 = 2\Re\left[\mathbf{E}_R^* \mathbf{E}_L\right] , \tag{2.44}$$

$$S_2 = 2\Im\left[\mathbf{E}_R^* \mathbf{E}_L\right] , \tag{2.45}$$

$$S_3 = |\mathbf{E}_R|^2 - |\mathbf{E}_L|^2 , \tag{2.46}$$

where $\mathbf{E}_R$ and $\mathbf{E}_L$ are the right and left circularly polarised components from Eq(2.38), $\Re$ and $\Im$ denote the real and imaginary parts respectively and E^* represents the complex conjugate. The parameter S_0 is the intensity of the beam, S_1 and S_2 define the vertical/horizontal and diagonal/anti-diagonal degree of the polarisation hence together define the orientation of the polarisation and S_3 is related to the helicity or degree of circular polarisation of the beam at a particular point. We can now equate Eqs.(2.39-2.42) and Eqs.(2.43)-(2.46) to find an expression for the orientation, ψ, and ellipticity, χ, in terms of the components of the FSL vector superposition as follows [18]

$$\begin{aligned}
\frac{S_2}{S_1} &= \frac{S_0 \cos 2\chi \sin 2\psi}{S_0 \cos 2\chi \cos 2\psi}, \\
&= \frac{2\Im\left[\mathbf{E}_R^* \mathbf{E}_L\right]}{2\Re\left[\mathbf{E}_R^* \mathbf{E}_L\right]}, \\
\tan 2\psi &= \frac{\Im\left[\mathbf{E}_R^* \mathbf{E}_L\right]}{\Re\left[\mathbf{E}_R^* \mathbf{E}_L\right]}, \\
\psi &= \frac{1}{2}\tan^{-1}\left(\frac{\Im\left[\mathbf{E}_R^* \mathbf{E}_L\right]}{\Re\left[\mathbf{E}_R^* \mathbf{E}_L\right]}\right),
\end{aligned} \tag{2.47}$$

and

$$\begin{aligned}
\frac{S_3}{S_0} &= \sin 2\chi, \\
&= \frac{|\mathbf{E}_R|^2 - |\mathbf{E}_L|^2}{|\mathbf{E}_R|^2 + |\mathbf{E}_L|^2}, \\
\chi &= \frac{1}{2}\sin^{-1}\left(\frac{|\mathbf{E}_R|^2 - |\mathbf{E}_L|^2}{|\mathbf{E}_R|^2 + |\mathbf{E}_L|^2}\right).
\end{aligned} \tag{2.48}$$

Using Eq(2.47) and Eq(2.48) we can represent the state of polarisation (SoP) by using polarisation ellipse from Figure(2.8) at each point in the transverse plane. An example for a fully structured light beam composed of $\ell_R = -3$ and $\ell_L = -2$ is given in Figure(2.9) which shows the polarisation ellipse at each point in the field superimposed on top of the intensity profile. In this manner we can represent both the spatial intensity structure as well as the polarisation distribution in the same image. We have chosen the colour scheme of red to represent linear polarisation, white to represent right hand circular polarisation and blue to represent left hand circular polarisation. Where the intensity of the beam drops below a certain value we have omitted from plotting the polarisation ellipses as at low intensities the polarisation is very sensitive to noise. For clarity this convention will be used in the remainder of the work presented in this thesis involving polarisation.

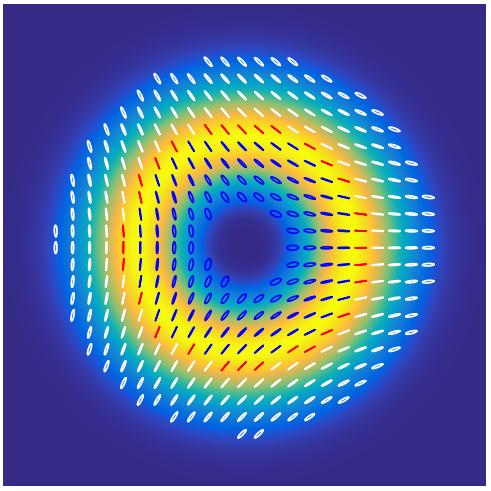

FIGURE 2.9: Transverse image of the intensity profile for a FSL light beam composed of a superposition of Laguerre-Gauss modes with $\ell_R = -3$, $\ell_L = -2$, $\gamma = \pi/4$ and $\beta = 0$. Red, white and blue ellipses correspond to linear, right circular and left circular polarisation respectively.

2.7 Conclusion

All electromagnetic radiation must obey Maxwell's equations which describe on a fundamental level how the electric and magnetic fields are affected by charges and how the fields oscillations affect each other. From Maxwell's equations we have shown a derivation of the paraxial wave equation that describes the propagation of light through homogeneous media. By ignoring the nonlinear polarisation response of the medium we have shown some of the linear solutions of the wave equation that are useful in the numerical modelling of laser systems and the important properties of such modes of light. In particular we focused on how these properties can be structured and controlled in the transverse plane.

Firstly we considered the most simple solution, that of a plane wave. Plane waves were shown to have no structure in any of lights properties and although useful in some applications are unphysical as the wave spans the entirety of space and require infinite energy. We then showed that the intensity could be confined in the transverse plane in the form of a Gaussian beam. Higher order modes associated with helical wave fronts in the form of Laguerre-Gauss modes were shown to be structured in not only their

intensity but also in their phase. Finally by creating a vector superposition of two Laguerre-Gauss modes with orthogonal polarisations the resultant polarisation distribution may also be inhomogeneous and structured in the transverse plane. Selection of the relative amplitudes, OAM and phase between the modes in the superposition allows all of lights properties - intensity, phase and polarisation to be tailored and structured to suit a variety of requirements.

In the following chapters we will see how the inclusion of the nonlinear polarisation response in the medium affects the propagation and structure of these forms of light. Such equations are not analytical and hence we will use a split-step Fourier method to numerically solve a variety of models that describe the interaction of these forms of light with nonlinear media and how placing the media in a cavity can lead to some very interesting phenomena.

Chapter 3

Optical Rogue Waves in Vortex Turbulence

Work based on the publication - Christopher J. Gibson, Alison M. Yao and Gian-Luca Oppo, "Optical Rogue Waves in Vortex Turbulence," *Phys. Rev. Lett.*, **116**, 043903, 2016.

3.1 Introduction

For many decades rogue waves in high seas were considered something of myth and legend, nothing more than extraordinary stories traded between veteran sailors. Enormous walls of water tens of metres high, capable of destroying large vessels, were described to appear from nowhere and vanish quickly leaving no trace of their existence other than the devastating damage to ships [31]. As the typical lifetimes of such waves are so short, scientific observations and quantitative studies of these events have only recently surfaced putting some truth to these tales [32, 33]. Now there is undeniable evidence that such rogue waves do occur in the ocean and at a rate that far exceeds that of the Gaussian statistics that are used to describe ocean wave heights. Satellites and

devices have been set up to observe, study and track these waves in order to understand more about their characteristics from the mechanisms behind their creation [34] to early prediction methods in their appearance [35].

In general, a rogue wave can be thought of as an extreme event whereby the height of a single wave is unexpected and is far larger than the average large waves observed [36]. Despite the originating mechanism behind the production of these events still being debated, rogue waves have been realised in a variety of optical systems [37, 38] since the optical counterpart was first observed in optical fibres [39]. They have been coined optical rogue waves due to the physical similarities they share with those found in the hydrodynamics and oceanography [40]. Since the realisation that such extreme events could be observed outside oceanography and hydrodynamics, interest in such phenomena has grown exponentially and rogue waves have been studied extensively in optical cavities [41, 42], photonic crystals [43] as well as various other optical systems. The interest in the generation, prediction and analysis of such extreme events is so broad that rogue waves have been studied in fields outside such as in plasma physics [44, 45].

In this thesis a spatio-temporal mechanism involving vortices in a two dimensional turbulent state capable of generating an accelerated production of such extreme events is analysed. The work focuses on the frequency unlocked state of a singly resonant optical parametric oscillator under the action of a low amplitude detuned seeding field where the loss of synchronisation of Adler dynamics [46] allows the generation of vortex mediated turbulence [47]. The universality of an approximate model allows the dynamics studied to be generalised to a huge variety of externally driven physical systems such as lasers with injected signal, semiconductor media and indeed systems outside optics from chemical oscillations [48] and reactions [49] and fluid dynamics [50]. The study of rogue waves in such a variety of systems allows for a greater understanding of the mechanisms behind their generation which appears to vary system to system, progress in prediction and prevention which could prove important for the safety of large oceanic vessels like ships and oil rigs and many other key statistics on such events [51, 52]. The

main aim of this chapter is to fully characterise and understand the behaviour of the two dimensional vortex mediated turbulent state previously described through a variety of methods such as correlation functions, intensity fluctuations and statistics on the rogue waves observed. The transverse intensity and phase distributions throughout this chapter use periodic boundary conditions except where stated (mainly Section 3.5) and are in the plane perpendicular to the direction of propagation such that the direction the light is travelling is straight out of the page towards the reader.

We begin in Section 3.2 by giving the mean-field considerations of an optical parametric oscillator and a nonlinear crystal that undergoes a wave mixing process known as spontaneous parametric down-conversion [9]. Details of some approximations to the model are given which is important for the universality of the dynamics observed in the system to be generalised to many other physical systems both in optics and further afield.

Section 3.3 deals with the bifurcation that leads to the onset of the vortex turbulence in which the rogue waves analysed are observed. First, the analytical and numerical solutions to model which have been previously studied [9] are analysed and the region of focus in this chapter is highlighted. The turbulence and spatially periodic pattern solutions are characterised into phase bound and unbound solutions to develop understanding of how the defects and helical waves behind the driving force of the turbulence develop and interact. Relevance to the unlocked dynamics of the Adler solutions [46] is also discussed as well as their importance at the bifurcation.

The focus of Section 3.4 is to fully characterise the behaviour and dynamics of the vortex mediated turbulence state and the rogue waves that are produced. We start by describing the main structures within the state, defects of zero intensity, phase profiles of the vortices generating their spin and the large intensity peaks that are observed from time to time. A widely accepted numerical definition of an extreme event or rogue wave is given which is used for showing we do in fact observe an accelerated production of rogue waves in the system compared with the Gaussian statistics of wave heights [38, 42, 44]. Decaying correlation functions and very short correlation lengths

show the turbulent nature of the field and statistics on the rogue waves produced in the form of probability density function reveal a mechanism for the control of extreme events produced.

Finally in Section 3.5 the transverse periodic boundary conditions are replaced with finite input beam sizes in order to replicate and simulate possible experimental observations with physical beams and we aim to show that the structures and dynamics presented previously are attainable experimentally in a wide arrange of systems that the models derived can be applicable to. Parameter regimes of occurrence of rogue waves in all models used are defined; again using mathematical definitions of an extreme event [38, 42, 44].

3.2 Mean Field Models

3.2.1 Spontaneous Parametric Down Conversion

Spontaneous Parametric Down Conversion (SPDC) is a fundamental nonlinear wave mixing process whereby a high intensity pumping laser at frequency ω_0 incident on a $\chi^{(2)}$ nonlinear crystal can interact in a manner that produces two new fields known as the signal and idler fields at lower frequencies ω_1 and ω_2 respectively [17]. A basic consideration of this process is shown in Figure(3.1).

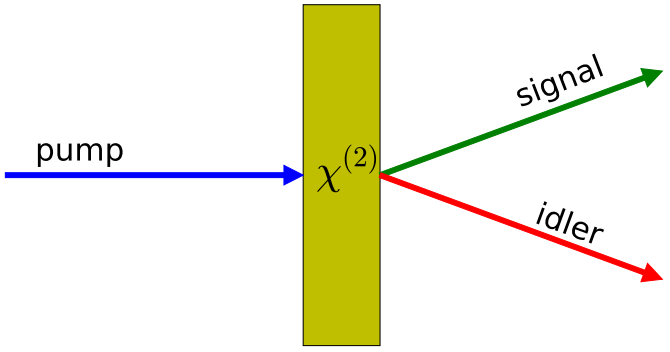

FIGURE 3.1: Graphic representation of the SPDC process. A pumping laser (blue line) interacts with nonlinear $\chi^{(2)}$ crystal with the production of two new fields, the signal (green) and idler (red).

Due to energy conservation the frequency of the signal and idler fields are constrained such that they add to that of the pump: $\omega_0 = \omega_1 + \omega_2$ which can be seen in Figure(3.2). The incident pump laser can excite the crystal medium to a virtual energy level as represented by the dashed line in Figure(3.2) with the decay back to the original state releasing two photons of lower frequency (hence the origin of the name down conversion) [9, 17]. This process happens almost instantaneously and is incredibly inefficient, just one down converted photon pair is produced for every 10^8 pump photons [53], although in more recent times efforts have been made to improve this efficiency [54]. The frequency constraint leads to two considerations for the down converted fields: degenerate down conversion where the frequency of the signal and idler fields are equal and non-degenerate where the frequency of the signal and idler are sufficiently different that they are distinguishable by their frequency alone. In the degenerate case although the frequencies are equals the process is not necessarily polarisation degenerate: the polarisation can be the same (Type-I SPDC) or orthogonal (Type-II SPDC) [55, 56]. The choice of crystal, and experimental parameters determine both the polarisation of the signal and idler fields and the level of degeneracy in the resultant frequencies. In the case of degenerate Type-I SPDC since the frequencies and polarisation are the same for both the signal and idler fields the pump photon can be considered to produce two signal photons since they are indistinguishable.

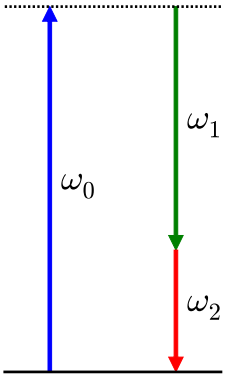

FIGURE 3.2: Energy conservation consideration of the interaction such that the frequency of the signal (green) and idler (red) sum to that of the pump (blue). The pump field excites the crystal medium to a virtual energy level (dashed black line) with the decay back to the ground state (solid black line) with the release of two lower frequency photons.

As well as energy conservation, momentum must also be conserved in the interaction.

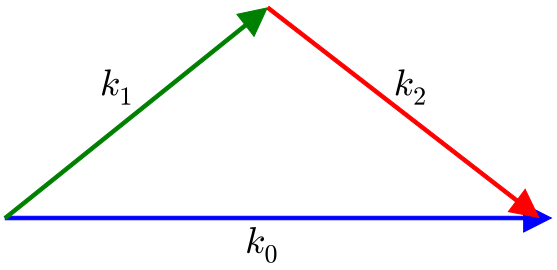

FIGURE 3.3: Momentum conservation of the process requires considerations of phase matching such that the wave vectors of signal and idler sum to that of the pump.

3.2.2 Optical Parametric Oscillators

Because the process of SPDC is so inefficient it is often useful to place the $\chi^{(2)}$ crystal in an optical cavity. An optical cavity reflects the pump beam between a set of mirrors such that it makes many round trips through the medium hence making multiple interactions. Furthermore this can also lead to stimulated emission of the signal and idler fields. A combination of these effects improves the efficiency of the down conversion. Such a set up is known as an optical parametric oscillator OPO that can be configured in a variety of experimental set ups, however the essential considerations are the same. Degenerate and non-degenerate down conversion as described in the previous section corresponding to doubly resonant (where the signal and idler fields are both resonant with the cavity due to having a shared frequency at half the pump frequency) and singly resonant OPOs (whereby the signal and idler frequencies are significantly different such that just one is resonant with the cavity) respectively are two such configurations of the OPO.

The experimental configuration can be controlled with considerations of the type of nonlinear crystal used in the cavity, orientation of the crystal within the cavity and temperature variations during the experiment. Here we focus on a $\chi^{(2)}$ crystal with non-critically phase matched or quasi-phase matched periodically poled crystals such that the co-linear phase mismatch is satisfied trivially (since the wave vectors of the produced signal and idler fields are parallel to that of the pump), and the down conversion is

highly frequency non-degenerate such that just the signal field is resonant with the cavity resulting in a singly resonant OPO (SROPO) set-up. The schematic for the configuration in consideration can be seen in Figure(3.4).

In the case of single resonance there is always perfect tuning between the signal field and the cavity since the SROPO automatically adjusts its frequency to the closest cavity resonance. As the frequency of the signal and idler fields do not have to be equal any changes in the cavity length are compensated for changes in the frequencies of the signal and idler fields respectively. This results in there being no detuning in the system and no possibility to observe pattern formation or any Turing instabilities. For this reason we include an injected signal shown by E_{IN} that acts as external forcing to the system. When $E_{IN} > 0$ the frequency of the signal locks to that of the injected signal thus introducing detuning between the signal field and the cavity resonant frequency. This allows the emergence of Turing instabilities and pattern formation as well as the onset of dynamical solutions that will be discussed in this chapter.

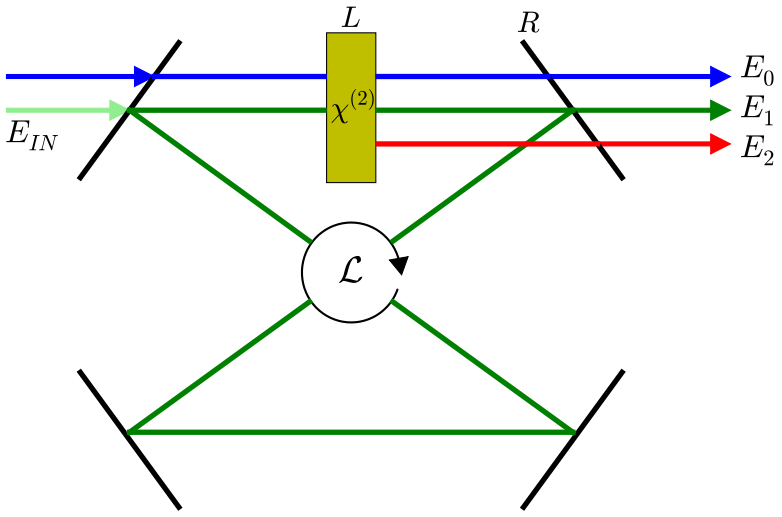

FIGURE 3.4: Schematic diagram of the SROPO set-up being analysed where a $\chi^{(2)}$ crystal of length L is placed in a cavity of round trip length $\mathcal{L}$. The blue line is the pump, the dark green and red lines are the produced signal and idler fields respectively and there is one partially reflecting mirror of reflectivity R. The light green line represents the seeding field acting at the input with frequency very close to that of the signal field.

3.2.3 Mean Field Models

We first consider the nonlinear propagation of an optical field in a second order nonlinear $\chi^{(2)}$ crystal. In Chapter 2 we derived the wave equation for the propagation of electromagnetic fields in a nonlinear medium. Thus in order to describe propagation in a $\chi^{(2)}$ medium we need to solve for the nonlinear polarisation term on the right hand side of the wave equation. Recall that the polarisation response of the medium is written as a power series in terms of the electric field as

$$\begin{aligned} \mathbf{P} &= \varepsilon_0 \left[\chi_e^{(1)}\mathbf{E} + \chi_e^{(2)}\mathbf{E}^2 + \chi_e^{(3)}\mathbf{E}^3 \,..\right] \\ &= \varepsilon_0\chi_e^{(1)}\mathbf{E} + \mathbf{P}^{NL} \end{aligned} \tag{3.1}$$

and for a second order nonlinear medium the nonlinear response is then

$$\mathbf{P}^{NL} = \varepsilon_0\chi^{(2)}\mathbf{E}^2. \tag{3.2}$$

Considering the pump, signal and idler field within the crystal the electric field can be written in the general form

$$\mathbf{E}(z,t) = E_0\exp[i(k_0z - \omega_0t)] + E_1\exp[i(k_1z - \omega_1t)] + E_2\exp[i(k_2z - \omega_2t)] + c.c. \tag{3.3}$$

Expanding the nonlinear polarisation term out in full we can then see that there are many frequency mixing components and nonlinear frequency responses of the medium and the ones of interest in this set up are those such that

$$\omega_0 = \omega_1 + \omega_2; \qquad \omega_1 = \omega_0 - \omega_2; \qquad \omega_2 = \omega_0 - \omega_1 \tag{3.4}$$

such that the frequency of the signal, ω_1 and the idler, ω_2 sum to that of the pump ω_0 a requirement described previously for parametric down conversion. We can now substitute the form of the nonlinear polarisation in Eq(3.2) and the form of the electric field in Eq(3.3) into the paraxial wave equation from Eq(2.28) and rearrange such that we obtain an expression for each of the fields within the crystal

$$\begin{aligned}
\frac{i}{2k_0}\nabla_\perp^2 E_0 - \frac{\partial E_0}{\partial z} - \frac{n_0}{c}\frac{\partial E_0}{\partial t} &= -\frac{i\omega_0\chi^{(2)}}{n_0 c}E_1 E_2 \exp\left[-i\Delta k z\right] \\
\frac{i}{2k_1}\nabla_\perp^2 E_1 - \frac{\partial E_1}{\partial z} - \frac{n_1}{c}\frac{\partial E_1}{\partial t} &= -\frac{i\omega_1\chi^{(2)}}{n_1 c}E_0 E_2^* \exp\left[i\Delta k z\right] \\
\frac{i}{2k_2}\nabla_\perp^2 E_2 - \frac{\partial E_2}{\partial z} - \frac{n_2}{c}\frac{\partial E_2}{\partial t} &= -\frac{i\omega_2\chi^{(2)}}{n_2 c}E_0 E_1^* \exp\left[i\Delta k z\right]
\end{aligned} \tag{3.5}$$

where $\Delta k = k_0 - k_1 - k_2$ is the phase matching condition within the crystal. Considerable simplification can be made if we introduce $\alpha = \frac{i\omega_0\chi^{(2)}}{n_0 c}$ and consider $\omega_1 = \mu\omega_0$ and $\omega_2 = \nu\omega_0$ where $\mu + \nu = 1$. Finally we consider non-critically phase matched or quasi-phase matched periodically poled crystals which trivially satisfy the phase matching condition such that $\Delta k = 0$ and assume $n = n_1 = n_2 = n_3$ such that Eqs(3.5) become

$$\begin{aligned}
\frac{\partial E_0}{\partial z} + \frac{n_0}{c}\frac{\partial E_0}{\partial t} &= \frac{i}{2k_0}\nabla_\perp^2 E_0 - \alpha E_1 E_2 \\
\frac{\partial E_1}{\partial z} + \frac{n_1}{c}\frac{\partial E_1}{\partial t} &= \frac{i}{2k_1}\nabla_\perp^2 E_1 + \mu\alpha E_0 E_2^* \\
\frac{\partial E_2}{\partial z} + \frac{n_2}{c}\frac{\partial E_2}{\partial t} &= \frac{i}{2k_2}\nabla_\perp^2 E_2 + \nu\alpha E_0 E_1^*
\end{aligned} \tag{3.6}$$

as in [17]. We are now ready to take the mean field limit adding in the OPO considerations for the propagation of the fields. The full derivation is omitted here but the principle behind a mean field limit derivation involves firstly assuming that the cavity mirror in Figure(3.4) has a very high reflectivity, R. We then make an expansion in the longitudinal Fourier modes and add the requirement that all the terms including the nonlinear one, are independent of the longitudinal variable z by applying boundary

conditions at the edges of the crystal. For the full calculation see [9], but the final result for the SROPO mean field limit is given by

$$\partial_t E = E_{IN} - (1 + i\theta)E + i\nabla^2 E + |E_0|^2 \operatorname{sinc}^2(|E|)E \tag{3.7}$$

where E is the complex field, E_{IN} is the amplitude of the external forcing, E_0 is the pump and θ is the detuning between the unperturbed field and the forcing field. By using a cubic approximation of the sinc^2 function we can generalise the model such that we can describe multiple physical systems and demonstrate the generality of optical rogue waves in vortex turbulence as in [57]

$$\partial_t E = E_{IN} - (1 - i\omega)E + i\nabla^2 E + Pf(|E|^2)E - \Gamma(\omega + \epsilon\nabla^2)^2 E \tag{3.8}$$

where we have introduced $\omega = -\theta$ as the detuning parameter and $P = |E_0|^2$ as the intensity of the pump. The nonlinear function $f(|E|^2)$ is $\operatorname{sinc}^2(|E|)$ for the optical parametric oscillator [9] as derived above, the cubic approximation $1 - |E|^2/3$ for the laser [58] and Γ is 0 or 1 to include the Swift-Hohenberg correction term. Without the correction we obtain the forced complex Ginzburg-Landau (FCGL) and with we obtain a forced complex Swift-Hohenberg model (FCSH). For small pump intensities the sinc^2 and FCGL model are in very good agreement. Time is normalised to the photon decay rate in the optical cavity and the space to $\sqrt{L\lambda/4\pi}$ where L is the cavity length and λ the wavelength.

3.3 Bifurcation to Turbulence

3.3.1 Fields in the Transverse Plane

The cases of relevance for the purposes of this thesis are obtained when the detuning ω is different from zero. In this case the frequency locked states that one observes at

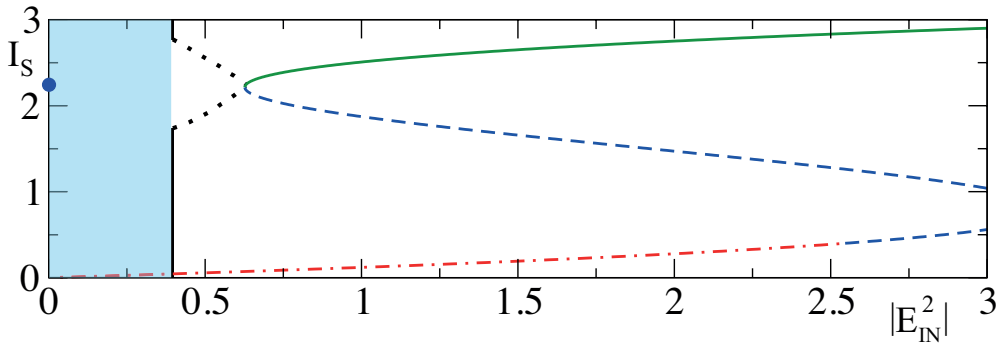

FIGURE 3.5: Stationary intensity of plane waves and their stability (stable = solid green, unstable with real eigenvalues = dashed blue, unstable with complex eigenvalues = dash-dotted red) for the FCGL model with P=4 and $\omega = 0.53$. The black dotted lines represent the minima and maxima of stationary hexagonal patterns formed when the decreasing the intensity of the external forcing and the upper branch of the S-shaped curve becomes unstable. The vertical black lines represent the bifurcation point where the hexagonal structure becomes unstable and the optical turbulent state starts (shaded area). The blue circle is the stationary intensity of the laser with no injection. We note that the FCSH model displays very similar results.

large driving amplitudes become unstable upon decreasing the driving E_{IN}. For fixed values of ω and P, the homogeneous stationary states of Eq(3.8) have a typical S-shaped dependence on E_{IN}^2 as displayed in Figure(3.5) where the stability of these solutions to perturbations of zero wave vectors is shown. The uppermost lines in the S-shaped curves of Figure(3.5) correspond to the homogeneous locked states where the external driving is large enough to overcome the frequency difference with the injected device. When increasing E_{IN}, a saddle-node bifurcation heralds the onset of the frequency and phase locked homogeneous states. When, instead, decreasing the parameter E_{IN} the homogeneous solution loses stability to spatially periodic patterns with a critical wave-vector given by $k_c = \sqrt{\omega}$. In Figure(3.5) the maximum and minimum intensities of the hexagonal patterns obtained numerically when reducing the external driver are displayed via a black dotted line.

By continuing to reduce the external forcing of the system the magnitude between the maxima and minima of the hexagonal structure grows linearly with the reduction of the forcing as shown by the dotted line in the stability diagram shown in Figure(3.5). This behaviour of the pattern continues until the bifurcation point shown by the vertical

dashed lines in Figure(3.5) at which point the hexagonal pattern becomes unstable and the structure becomes unstable. At the bifurcation point the rigid structure begins to evolve and the fixed peaks and ridges of the hexagonal pattern begin to dislocate. After sufficient evolution, the troughs of the structure begin to collapse into vortices of integer OAM (± 1) that form in pairs of opposite handedness and a regime of unlocked dynamics sets in [9]. The pairs of vortices interact and are continually created and annihilate when in close proximity to one another and have opposite handedness. The vortices dissipate throughout the structure and cause a complete breakage of the pattern. The resultant state is a dynamical turbulent solution that is driven by the interaction of helical vortices of zero intensity similar to the vortex-mediated turbulence described in [47].

In order to fully understand the onset of defect mediated turbulence in this system it is important to understand the bifurcation and how the hexagonal light pattern becomes unstable. Full characterisation of the behaviour of the turbulent state will be detailed in a later section, here we focus on the bifurcation and transition from hexagonal structure to the defect mediated turbulent state. Figure(3.6) shows the progression of the instability from image (a) which shows the transverse intensity of the stable hexagonal pattern before the bifurcation. When the intensity of the forcing in the system is above the bifurcation point (to the right of the vertical black line in Figure(3.5)) the stationary periodically modulated phase of the hexagonal structure shown in image (b) indicates that the frequency of the signal field is locked to the frequency of the injection. As described previously this frequency locking results in detuning between the resonant cavity frequency and that of the signal field. By studying the phase of the pattern as the intensity of the injected field is reduced it is clear that the instability first presents itself in the form of a phase instability. Beyond the bifurcation point, for $E_{IN} < 0.61$, the phase is no longer stationary and begins to evolve as shown in image (d) of Figure(3.6). With evolution of the phase the peaks dislocate from their fixed position and the troughs begin to collapse into vortices as can be seen in image (c). The vortices are of opposite OAM as can be seen from the corresponding phase diagram in image (d) showing the evolution in the phase occurring in the opposite directions.

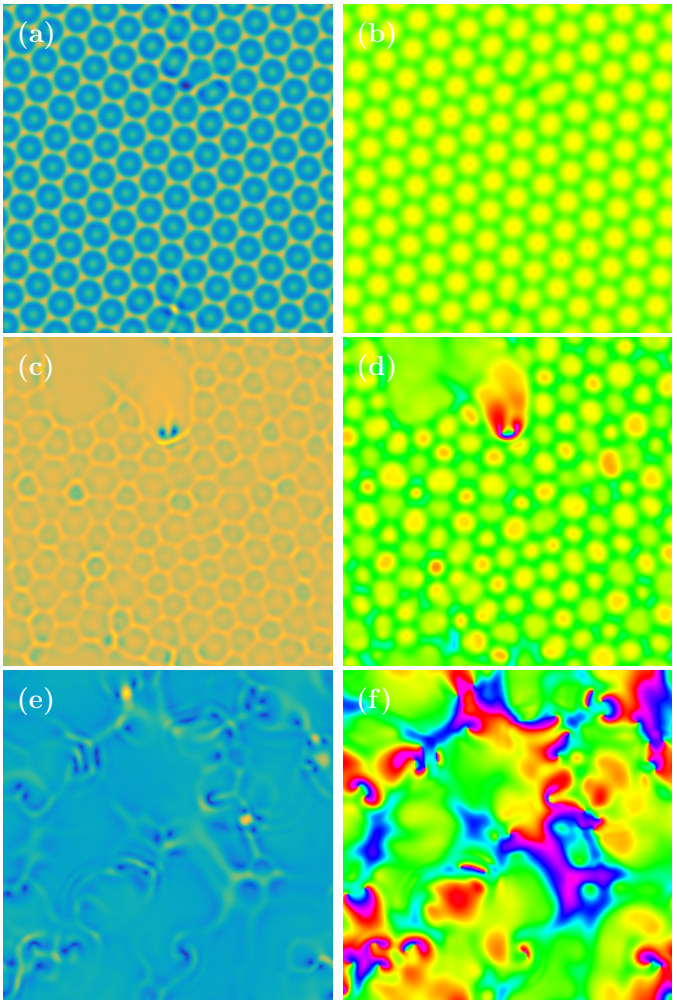

FIGURE 3.6: Transverse intensity (left) and phase profiles (right) across the field before, during, and after the bifurcation for (a)-(b) stable hexagonal Turing patterns, (c)-(d) unstable hexagonal structure during the bifurcation and (e)-(f) defect mediated turbulence for the sinc^2 model. Parameters are P=8 and $\omega = 1$ for all images, $E_{IN} = 1.8$ for (a)-(b), $E_{IN} = 1.5$ for (c)-(f).

Finally with the growth of the phase instability, the amplitude of the structure also becomes unstable and after the vortices permeate the structure there is full breakage of the pattern and the solution becomes a dynamical turbulent state that is driven by the defects as shown in image (e) of Figure(3.6) with the corresponding transverse phase in image (f). From the transverse intensity where there are interactions between vortices there are also large intensity peaks. Clusters of opposite OAM vortices result in the production of incredibly large short lived intensity spikes. By comparison between the

transverse intensity in image (e) and the phase in image (f) we can see the polarity of the OAM of each defect and the position of the large amplitude peaks. In close proximity to defects of opposite OAM it is clear there are large peaks produced. From this we can understand that when the hexagonal structure becomes unlocked in frequency from the injection the phase is no longer fixed and stationary and as the phase instability evolves this leads to an amplitude instability leading to the onset of defect mediated turbulence. To give an idea of the size of the short lived intensity peaks the profile across a cut of the transverse intensity is plotted in Figure(3.7). The cut across the transverse plane is through the intensity peak towards the top of image (f) in Figure(3.6). We can see the intensity spike is several times larger than the background turbulence and in close proximity to an optical defect.

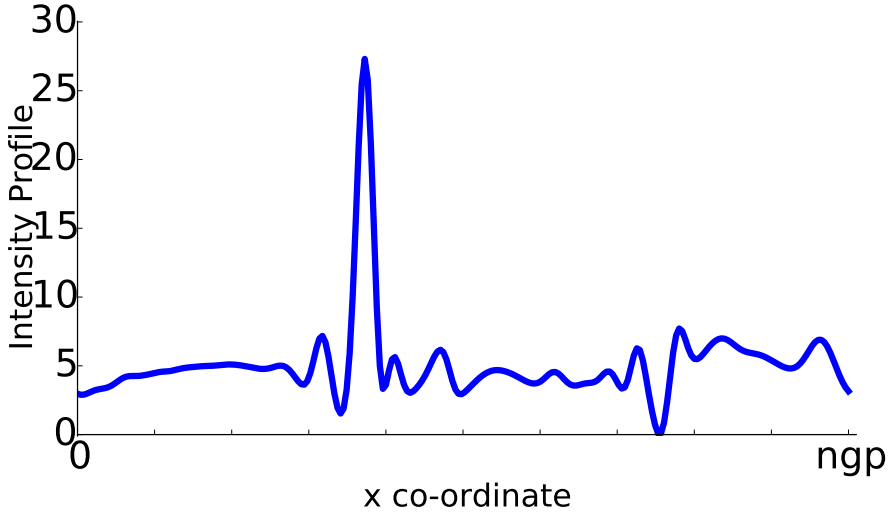

FIGURE 3.7: A cut through the transverse intensity showing the intensity profile through a rogue wave peak in image (e) of Figure(3.6).

3.3.2 Fields in the Argand Plane

The transition from hexagonal structure to defect mediated turbulence through phase instability evolving to an amplitude instability can be more clearly observed by studying the dynamics of both the phase and amplitude instabilities in the Argand plane (real versus imaginary parts of the electric field) when the forcing intensity is below the

bifurcation. The initial distribution of the field is given in image (a) in Figure(3.8) and it is clear that the pattern state is a phase and amplitude bound solution. The distribution of the field is restricted to a small region of the Argand plane showing that the amplitude and phase can only take on restricted values. After the bifurcation point in image (b) of Figure(3.8) however we observe that the field loses stability in a circle around the Argand plane and the distribution of the field spreads around this circle. This indicates the formation of a phase instability (corresponding to image (d) of Figure(3.6)) as the amplitude of the points remains constant but the phase of the field loses stability and spreads around the Argand plane. The solution is no longer phase bound. At the point where the phase distribution covers the entire circle as in image (c) the phase instability grows into an amplitude instability, first with the formation of defects at the troughs of the structure and then, through interaction of vortices, the emergence of large intensity spikes. The distribution of the field in the Argand plane in image (d) shows that the resultant turbulent field is unbound in both phase and amplitude.

This then begs the question of why the distribution of the phase initially spreads around the Argand plane in a counterclockwise direction and why this phase instability grows and leads to an amplitude instability. To fully understand the mechanisms behind this bifurcation and the generation of the turbulent state in forced models described by Eq(3.8) we can consider dynamical solutions corresponding to unlocked oscillations and their robustness to spatially dependent perturbations in the FCGL form of Eq(3.8). In the absence of diffraction, which provides the spatial coupling between points on the field, an approximate closed trajectory (limit cycle trajectory) can be found by using period averaging methods [58] such that

$$E = A_0 \left[\cos\left(\phi(t)\right) + i \sin\left(\phi(t)\right)\right] \tag{3.9}$$

where $A_0^2 = 3(P - 1/P)$. In such a consideration $\phi(t)$ is well approximated by its period average $\Omega t + \pi$ with $\Omega = \sqrt{\omega^2 - \omega_L^2}$ and $\omega_L = E_{IN}/A_0$. In the case that $\omega > \omega_L$, such

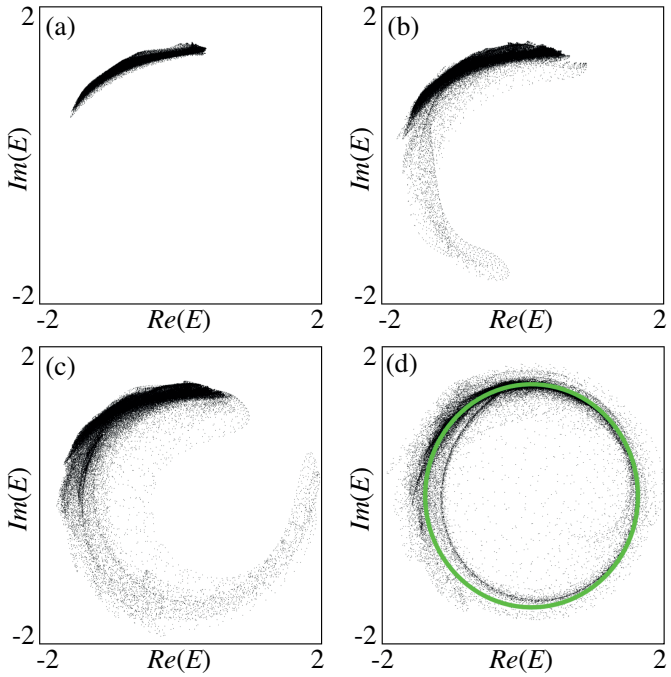

FIGURE 3.8: Field distributions in the Argand plane of the unstable hexagonal pattern at t=0 (a), during phase instability (t=183) (b), in a regime of amplitude instability (t=236) (c) and in a fully turbulent state (t=472) (d). The green circle in (d) is the Adler limit cycle. Simulations of the FCGL equation with the same parameters as in Figure(3.5) and $E_{IN} = 0.60$.

that the parameter Ω is real, we are in a parameter space in the absence of locked states. The trajectory is given by the phase-drift solution of the Adler equation as in [46] given by

$$d_t\phi = \omega - \omega_L \sin\left(\phi(t)\right). \tag{3.10}$$

Clearly such a solution has a dynamical phase term and is phase unbound. The green circle in Figure(3.8) is the solution to the Adler equation given by Eq(3.10) superimposed onto the Argand diagram against the distribution of the field for the turbulent regime. We can see from Figure(3.8) that the dynamics are ruled by the unlocked dynamic state. The accuracy of the approximate solution has been numerically tested for a wide range of forcing intensity values, $|E_{IN}|^2$, in the FCGL model. For comparison the difference in intensity is within a percent of the true value and excursions in

frequency are within 10 percent.

Such analysis of the limit cycle demonstrates exactly how the bifurcation from hexagonal structure to defect mediated turbulence occurs through the two instabilities. When the pattern becomes unstable the system tends to the unlocked Adler limit cycle given by the green circle shown in the Argand diagram. However with the spatial dependence of the field given by the diffraction, the limit cycle is not stable as each of the points in the field are not independent as in the analysis presented for the Adler solution. The diffraction means the oscillations in the field are no longer synchronised and soon become out of phase and become dislocated from the limit cycle. As the distribution of the field becomes less synchronous the amplitude instability presents with formation of defects with integer OAM as described previously.

3.3.3 Turbulence From Plane Waves and Zero Solutions

Understanding this mechanism for the generation of vortex turbulence then suggests that we can also generate such a state from the unstable lower branch of the analytical homogeneous plane wave solution and indeed even from a homogeneous zero solution. As such we have studied the stability of the spatially synchronised oscillation by including spatial coupling in the FCGL. The stability eigenvalues of the spatially synchronised limit cycle are given by

$$\lambda_{\pm} = -(P-1) \pm \sqrt{(P-1)^2 - (\omega - k^2)^2} \tag{3.11}$$

where k is the spatial wave-vector. At the critical wave-vector for pattern formation $k_c = \sqrt{\omega}$, the stability λ_+ is marginal, however perturbations due to the approximate nature of the field induce a slow instability of the synchronous oscillation. The eigenvector associated with λ_+ is along the limit cycle, again demonstrating a phase instability. As mentioned earlier, this phase instability grows into an amplitude instability and then into vortex-mediated turbulence as demonstrated numerically in Figure(3.9) where we

have started from the initial condition of low amplitude noise. A homogeneous zero state with added noise quickly evolves towards the unstable limit cycle as seen in image (a) of Figure(3.9) where the coloured dots are the distribution of the field in the Argand plane at different times from 1 to 4. The limit cycle dynamics first synchronises the spatial oscillations (see the narrow red line at t = 90 shown in image (b) of Figure(3.9)) and then moves towards the vortex turbulence state via phase (Figure(3.8) image (b)) and amplitude (Figure(3.8) image (c)) instabilities. We outline that the mechanism of spontaneous vortex creation in the FCGL and FCSH is not trivial.

In contrast with the CGL, stationary vortex solutions are not possible in driven systems like Eq(3.8) as all locked states have bound phases around that of the injection. However, at low driving amplitudes, moving vortices and vortex-mediated turbulence in Eq(3.8) are possible due to the Adler unlocked dynamics of the limit cycle trajectory. It is known [59] that the adiabatic elimination of the polarisation variable introduces an all wave-vector instability of the spatially homogeneous state below the point where the linear stability of the lower branch of the S-shaped homogeneous state predicts complex conjugate eigenvalues (see Figure(3.5)). This feature, in principle, may have serious consequences in the turbulent regimes. A second important consequence of our analysis, however, is that Eq(3.8) for $\Gamma = 0$ displays a very fast dynamics that takes the system towards the limit cycle where large wave-vector instabilities are promptly eliminated (see Figure(3.9)). The large wave-vector instability of the lower branch of the homogeneous stationary states is not present in the case of FCSH when $\Gamma = 1$. This mechanism for vortex turbulence is essential for the generation of rogue waves in externally driven systems described by the spatio-temporal dynamics of Eq(3.8).

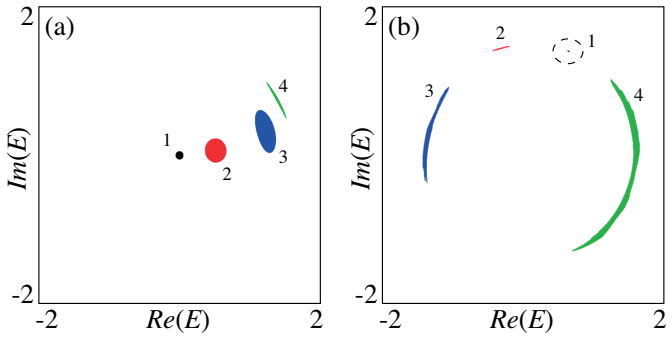

FIGURE 3.9: Field distributions in the Argand plane for the FCGL equation with the same parameters as Figure(3.5) and $E_{IN} = 0.70$ starting from noise. (a): $t = 0$ (black), $t = 0.40$ (red), $t = 0.75$ (blue) and $t = 1.4$ (green) and (b) $t = 90$ (black), $t = 256$ (red), $t = 280$ (blue) and $t = 314$ (green).

3.4 Characterisation of Rogue Waves and Turbulent State

3.4.1 Power Conservation

Here we characterise the behaviour and statistics of the turbulent dynamics and show mathematically that what we observe is in fact rogue waves and the state is different from a random superposition of plane waves which is referred to as a speckle pattern [60, 61]. The mechanism for vortex turbulence described in the previous section is essential for the generation of rogue waves in externally driven systems described by the spatio-temporal dynamics of Eq(3.8). These systems are outside thermodynamic equilibrium, do not display relaxation oscillations and present a delicate balance between the energy input and the losses (the pump, injections, nonlinearity and output mirror). During the turbulent evolution, the total power remains almost constant at values close to those of the laser with no injection. By considering the energy density and the energy flux of the FCGL equation the time evolution of the power is given by

$$\frac{\partial \mathcal{P}}{\partial t} = 2 \int \left[E_{IN} \Re(E) + \left(P - 1 - \frac{P}{3} |E|^2 \right) |E|^2 \right] dxdy \tag{3.12}$$

where (x, y) is the transverse plane to direction of propagation. For the approximate limit cycle solution the power $\mathcal{P}$ is conserved at the value of $\pi \omega_0^2 A_0^2$ where ω_0 is the

beam width of the input laser. With the onset of defect mediated turbulence, however, maintaining a constant power in the presence of vortices of zero intensity implies the simultaneous appearance of large amplitude spikes. Indeed if the vortex density is large this allows multiple vortex collisions and interactions that allow for the formation of many large, localised short lived spikes in the intensity of the output beam. Rare short lived large intensity spikes is one of the main characteristics of rogue waves.

The evolution of the power is shown in image (a) of Figure(3.10). We can see that although there are minor oscillations in the power over time, on average it maintains an almost constant value for a variety of values of P for each of the FCGL and FCSH models. It can also be seen that there is very good agreement between the numerical simulations and the predicted value of the power from the approximate model in Eq(3.12) which is given by the horizontal dashed lines.

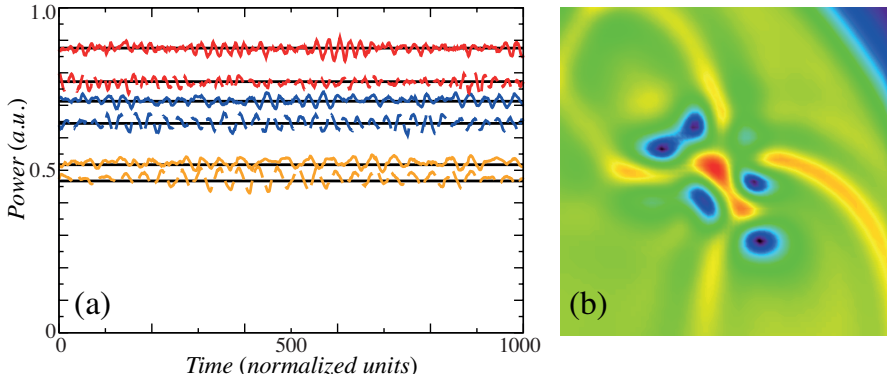

FIGURE 3.10: (a) Time evolution of the power for three values of the pump P=2 (orange), P=4 (blue) and P=5 (red) for the FCGL (solid lines) and FCSH (dashed lines) models during defect mediated turbulence. The horizontal dashed black lines represent the respective theoretical predictions of the power from the approximate model in Eq(3.12). (b) Zoomed in transverse intensity profile for a multiple vortex interaction producing a large intensity peak.

The particular shape and symmetry of each individual rogue wave is determined by the number and position of the surrounding defects which produce them such that each individual spike is unique dependent on the various interactions and waves surrounding it. Such a feature is unique to this particular mechanism of rogue wave formation. Image (b) of Figure(3.10) shows how the particular number and position of defects around an intensity peak can influence its shape. Rogue waves - in single transverse

mode class-B lasers with injected signals - have been previously observed in [42], though due to relaxation oscillations. Here the formation of such extreme events are produced in the transverse plane due to 2D vortex turbulence. Without spatial coupling from the diffraction no rogue waves can be observed by any system described by Eq(3.8) as we showed when considering the limit cycle.

3.4.2 Long Tailed Probability Density Functions

To characterise the state of our spatio-temporal turbulence into regimes where rogue waves are observed we use a commonly accepted mathematical definition of what classifies as a statistically rare event [38, 42, 44]. If the intensity at a point in the field over a significant period of time exceeds a height of eight standard deviations above the mean wave height then the wave can be considered a rare event or as described in oceanography: a rogue wave. Hence we use the cut off

$$I_{x,y} \geq \left\langle \langle I \rangle_{x,y} \right\rangle_t + 8\sigma \tag{3.13}$$

to define a rogue wave. This method falls within 3% of the significant wave height method that is used in oceanography [38]. In order to determine the regions of parameters that give rise to turbulence in which rogue waves can be observed, the intensity at each point of the transverse period is analysed over a significant period of time. The length of time is chosen such that the statistics recorded are accurately representative of the general behaviour of the turbulence for each given choice of parameter space. Using the recorded statistics of the wave heights, probability density functions (PDFs) are calculated that represent the relative number of recorded intensities observed in the field. The number of observations of each intensity is normalised to unity and the intensity axis of the probability density function is normalised by the standard deviation with the mean also subtracted. This means that any PDF for any of the chosen parameters can easily be compared independent of the time over which the statistics

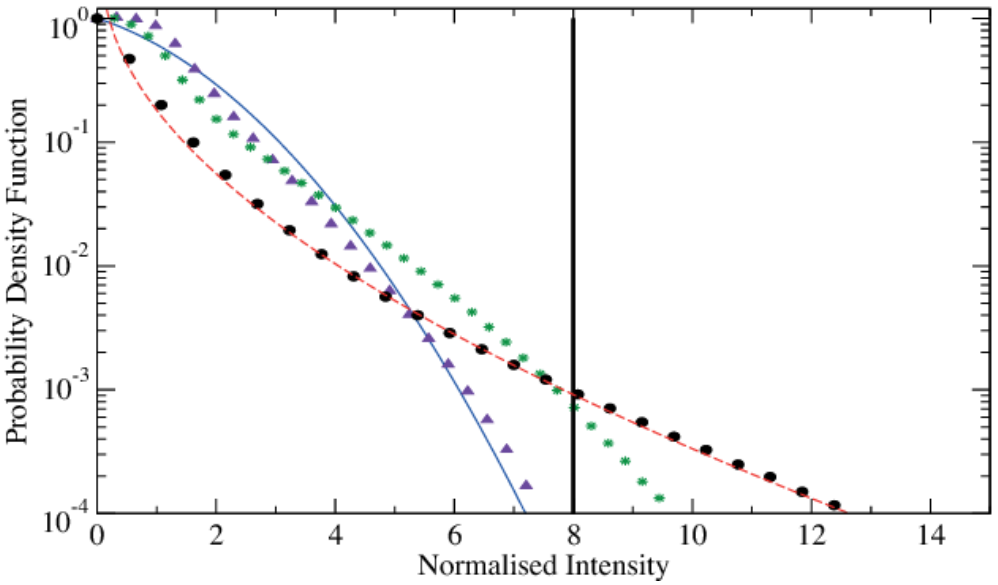

FIGURE 3.11: Intensity PDFs for the FCGL model for $P = 2$, $\omega = 0.3$, $E_{IN} = 0.24$ (purple triangles) with Gaussian fit (blue line) and $P = 8$, $\omega = 2.4$, $E_{IN} = 3.40$ (green stars) and the $sinc^2$ model: $P = 8$, $\omega = 1$, $E_{IN} = 1.48$ (black circles) with Weibull fit (red dashed line). The vertical black line represents the threshold for defining waves as an extreme event.

were recorded. Furthermore, the rogue wave cut off point is very easily identified and is at the same point for each figure produced.

Figure(3.11) gives the intensity PDFs for different regimes of vortex turbulence. When the pump intensity is low (shown by P=2, purple triangles in the PDF) no rogue waves are observed and we can see that none of the distribution lies above the eight standard deviation cut off for a 10^{-4} probability of observation. At such pump intensities for all models in Eq(3.8), the PDF is accurately modelled by a Gaussian distribution of the form

$$f(x) = A \exp\left(-\frac{x^2}{b^2}\right). \tag{3.14}$$

This can be attributed to the low number of defects of zero intensity, which in turn corresponds to a small number of vortex interactions. Gaussian distributions of this form well approximate the wave heights seen in the ocean. For the distribution shown

in Figure(3.11) the parameters for the Gaussian fit are $A = 1.3, b = 2.8$ and $x = I - \langle I \rangle$ where $I = |E|^2$ is the intensity and $\langle I \rangle$ is the average intensity over all the images included in the evaluation.

By increasing the intensity of the pump, the number of vortex interactions increase and become frequent thus accelerating the production of rogue wave events above that of the Gaussian distribution. By controlling the intensity of the pump, the probability of observing rogue waves can be also be controlled. As the intensity of the pump is increased the distribution of wave heights changes drastically and we observe long tailed PDFs typical of non-Gaussian distributions [32]. Long tailed PDFs show a mass generation of rogue wave events. For a pump intensity of P=8 (green stars for the cubic model and black dots for the sinc^2 model in the PDF plot), we can see that the distribution is non-Gaussian and the long tail well past the rogue wave cut-off shows the mass observation of short lived rogue wave intensity spikes. This distribution can be approximated by a Weibull distribution of the form [32, 57]

$$f(x) = A \left(\frac{x}{b}\right)^{c-1} \exp\left(-\frac{x}{b}\right)^{c}. \tag{3.15}$$

Parameters of the Weibull distribution for the fit in Figure(3.11) are $A = 1.4, b = 0.42, c = 0.62$ and again $x = I - \langle I \rangle$. The PDFs show that by controlling the intensity of the pump we can control the probability of observing rare events.

3.4.3 Comparison with Speckle

It is important to note that the non-Gaussian statistics displayed in Figure(3.11) cannot be replicated by the superpositions of random waves. Such superpositions of random waves have been referred to as *speckle* [60, 61] and are formed by the interference between many monochromatic waves of different phase and amplitudes. The resultant transverse field is shown in Figure(3.12) and it can be seen that it does share some of

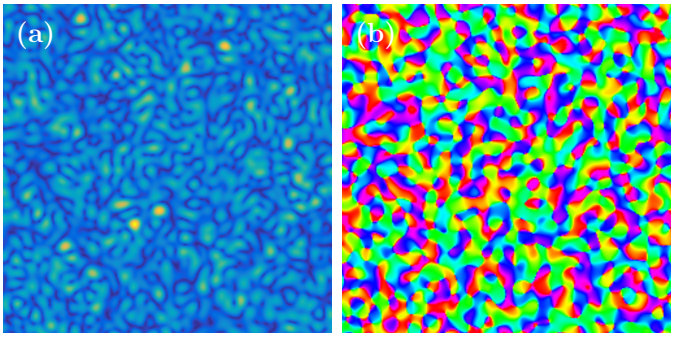

FIGURE 3.12: Transverse intensity (left) and phase profile (right) for a speckle pattern created from a random superposition of 1000 plane waves of random amplitude and phase.

the features of the defect mediated turbulence we have presented. There are areas of near zero intensity and large amplitude spikes in areas of the transverse intensity plane.

However it is easy to show that our defect mediated turbulence is different from speckle. Firstly, we can calculate a correlation function for each of the solutions and show that the difference in their correlation function indicates the difference between the underlying mechanism of each solution. A correlation function provides a measure of the spatial dependence of the electric field across the transverse plane. If two points separated by a given distance are highly correlated then knowing the state of the field at one point gives a good approximation of the field at another. Conversely, two uncorrelated points indicate that they are independent of one another and information about one of the points has no effect or dependence on the other. Using a correlation function of the form [62]

$$C(\rho) = \frac{\left\langle \left(\Re\left[E(\mathbf{r},t)\right] - \langle \Re\left[E(t)\right]\rangle_{x,y} \right) \left(\Re\left[E(\mathbf{r}',t)\right] - \langle \Re\left[E(t)\right]\rangle_{x,y} \right) \right\rangle_t}{\left\langle \left(\Re\left[E(\mathbf{r},t)\right] - \langle \Re\left[E(t)\right]\rangle_{x,y} \right) \left(\Re\left[E(\mathbf{r},t)\right] - \langle \Re\left[E(t)\right]\rangle_{x,y} \right) \right\rangle_t}, \tag{3.16}$$

where $\Re[E(r,t)]$ represents the real part of the field at position, $\mathbf{r}$, and time, t. The angle brackets are calculated averages which are given by the relevant subscripts of the brackets. For a speckle field the correlation function is well approximated by a sinc function such that [61]

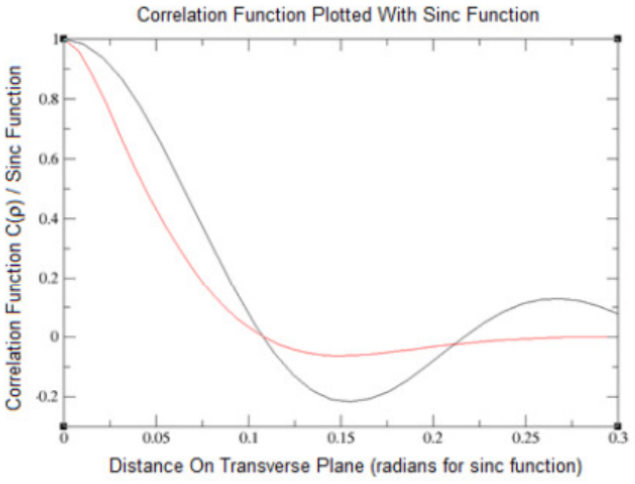

FIGURE 3.13: Correlation functions as a function of distance in the transverse plane for the defect mediated turbulent state (red solid line) and the speckle pattern given by Eq(3.17) (black solid line).

$$C(\rho) = \frac{\sin(kx)}{kx} \tag{3.17}$$

Figure(3.13) shows the correlation for the fully defect mediated turbulent state as well as the sinc function which represents the correlation function for a speckle pattern. It is clear that the significant difference between the correlation functions gives a hint at the different mechanisms of both states. Since speckle is generated by a distribution of waves with different amplitudes and phase but of the same frequency there is an underlying correlation length between points in the field as is typical of any interference effect. This underlying correlation length can be seen in the periodic oscillations of the correlation function. For defect mediated turbulence it can be seen that the correlation function decreases rapidly as the distance between points increases indicating that beyond a very short spatial scale there is no dependence between points. Because of the amount of interactions between vortices on a short scale there is some level of correlation but beyond the typical interaction distance between the vortices there is no spatial dependence which explains the rapid drop off in correlation function.

We also note that the rogue waves in vortex turbulence demonstrated in this work

are different from those due to vorticity in models of inviscid fluids [33]. The CGL and CSH have been shown to be equivalent to the flow of a compressible and viscous fluid of density $\rho = |E|^2$ and velocity $\mathbf{v} = \nabla\phi$ where ϕ is the phase of the field [63, 64]. Where forcing is considered in our case, the relation $\nabla \times \mathbf{v}$ remains close to zero close to the location of rogue wave intensity spikes. This difference can be seen by comparing the typical phase distribution of the speckle field with that of the defect mediated turbulence as shown in Figure(3.12).

From this we conclude that the rogue waves generated in our system are formed from interacting defects in the absence of vorticity rather than random superposition of waves and the non-Gaussian PDFs generated from the defect mediated turbulence have a different mechanism and cannot be described simply by speckle.

3.5 Finite Input Beams

We now remove the periodic boundary conditions and now consider finite sized input beams representable of experimental set-ups and physical systems and show that the dynamics described in the previous sections hold in the limit of finite input beams. This is done simply by shaping the plane wave inputs with an hyperbolic tangent function of the form

$$E = \frac{E_0}{2}\left(1 - \tanh\left(a(r-b)\right)\right) \tag{3.18}$$

which produces a top hat input where $r = x^2 + y^2$ is the radius from the centre of the input beam, a controls the width of the top hat and b controls the steepness of the edges of the beam. This gives complete control and flexibility over the size and shape of the top hat pump.

We have carried out numerical simulations with finite boundaries to show that the same onset to defect mediate turbulence is observed and this effect is not boundary related.

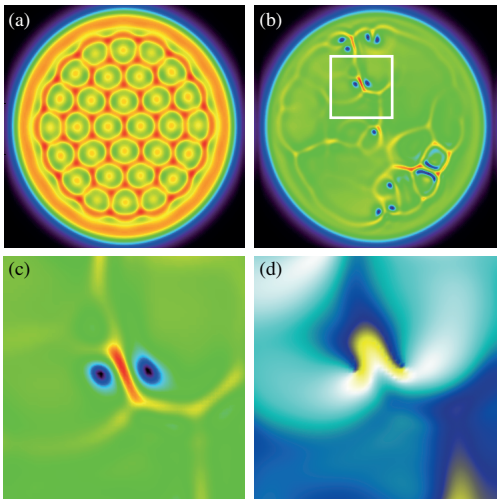

FIGURE 3.14: Transverse intensity for (a) hexagonal Turing pattern, and (b)-(c) optical vortex-mediated turbulence with the corresponding phase for two vortices with OAM of opposite polarity shown in (d). Simulations are for the FCGL equation with P=6, $\omega = 0.77$, $E_{IN} = 1.00$ (a) and $E_{IN} = 0.95$ in (b)-(d). The area in (c) and (d) corresponds to that of the white square superimposed in (b).

Figure(3.14) shows the transverse field distribution at the same stages of the bifurcation as in Section 3.3 and we can see that the same transition occurs and in the same manner as in the periodic boundary case. The transition from pattern to turbulence occurs at the same forcing intensity as in the periodic boundary case. Figure(3.15) gives a three dimensional representation of an optical rogue wave in the case of a top hat pump.

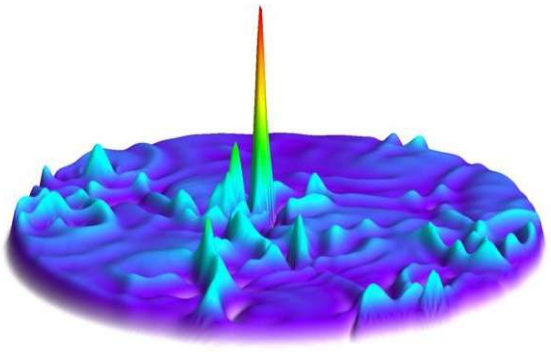

FIGURE 3.15: Three dimensional representation of the transverse intensity profile for a rogue wave with finite input boundaries for the same parameters as in (b)-(d) of Figure(3.14).

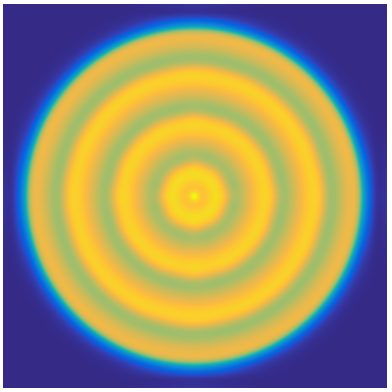

FIGURE 3.16: Transverse intensity structure of a diffraction ring pattern formed where the forcing of the system is too small for defect mediated turbulence to remain stable. Parameters are $P = 6$, $\omega = 0.77$ and $|E_{IN}|^2 = 0.64$ for the FCGL model.

One interesting thing to note is with the top hat pump is that a lower bound on the intensity of the forcing E_{IN} is introduced for which the defect mediated turbulent state is stable. The top hat boundary continually tries to propagate inside the field. When the forcing of the system is large enough the formation, interaction and annihilation between vortices is frequent enough to break any diffraction patterns that try to present. When decreasing the forcing of the system however, the boundary propagates inside and clears up the turbulence. The result is a diffraction ring pattern state as shown in Figure(3.16).

For completeness we have analysed the stability region for defect mediated turbulence where we would expect to see these dynamics experimentally in laser experiments. Figure(3.17) shows the stability region as a function of the pump and forcing intensities for the FCGL model. The shaded pink region is the parameter space where we predict the observation of rogue waves, the upper curve is the transition from hexagonal pattern to turbulence and the lower curve is the transition from turbulence to diffraction ring pattern.

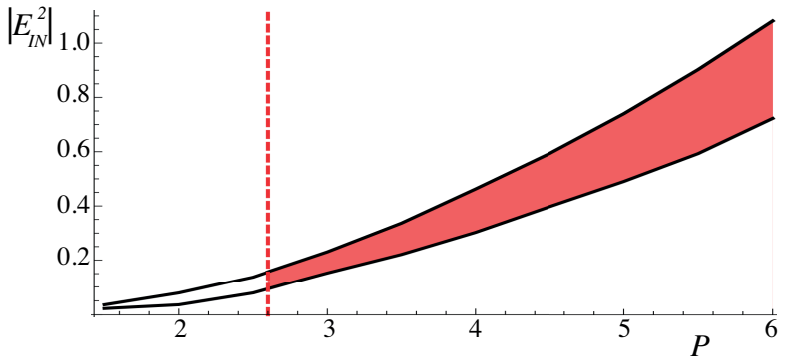

FIGURE 3.17: Stability region for observation of rogue wave peaks defined by Eq(3.13) for the FCGL model. The upper curve is the hexagonal structure to defect mediated turbulent transition. The lower curve is the turbulence to target pattern transition. No rogue wave peaks above the threshold defined in Eq(3.13) are observed below the vertical red dashed line.

3.6 Conclusion

In conclusion, we have demonstrated a mechanism for producing rogue waves in the transverse area of externally driven nonlinear optical devices via vortex turbulence. Given the universality of our model, this mechanism should be observable in a large variety of systems. Models of lasers with injected signal, where the invariance of the Adler limit cycle is well known [58, 65, 66], can be easily extended to semiconductor media and to class B lasers, thus including the largest majority of solid state lasers. Outside optics, vortex-mediated turbulence without driving has been observed in nematic liquid crystals [67], chemical reactions [49] and fluid dynamics [50]. In the unlocked regime of these systems with driving, vortex turbulence can excite rogue waves and lead to the formation of highly inhomogeneous fields with non-Gaussian statistics. The prototype model used to describe rogue waves is the Non-Linear Schrödinger (NLS) equation [32, 37]. The FCGL and FCSH models studied here are active, non-conservative systems outside thermodynamic equilibrium where many of the methods developed for the NLS cannot be applied. In the NLS equation, as well as in the CGL and CSH equations, stationary vortex solutions are possible although mainly unstable. In the presence of forcing, vortices can only exist in dynamical states. It is exactly in these situations that we have demonstrated rogue waves close to regions of interaction of turbulent vortices.

By studying the bifurcation to turbulence we have fully understood and demonstrated how to generate such states through an amplitude instability which grows into an amplitude instability with comparison to the Adler limit cycle. Using a well accepted definition of extreme events we have shown the parameter regime where such states are expected to be observed and showed using finite boundaries that this state is non boundary dependent.

Because of universality, suitably perturbed NLS models may also display these features. Unlike rogue waves in the longitudinal direction [37], the aspect ratios required for transverse rogue waves induced by 2D vortex turbulence are extremely small (typical input beams have diameters less than 1mm) and the statistics require times of the order of hundreds of μs [68]. The small aspect ratio, the full 2D character and the quick dynamics represent the major advantages of transverse optical devices in studying the generation and control of rogue waves with applications,by universality, in hydrodynamics and oceanography.

Chapter 4

Propagation of Fully Structured Light

Work based on the publication - Christopher J. Gibson, Patrick Bevington, Gian-Luca Oppo and Alison M. Yao, "Control of polarization rotation in nonlinear propagation of fully structured light," *Phys. Rev. A.*, **97**, 033832, 2018.

4.1 Introduction

Vector beams or Fully Structured Light (FSL) beams, obtain their name from the vector nature and inhomogeneous spatial intensity, phase *and* polarisation structure that characterises such modes of light; all of lights properties are structured spatially and can be tailored and controlled across the transverse domain [28–30]. For a mathematical description of such types of light see Section 2.6 of Chapter 2 and references therein which details how such beams are created and the form they take which is important for the work presented in this chapter.

FSL beams have received increasing attention in a variety of applications like second and third harmonic generation microscopy [69] due to the unique properties such as

tighter focussing [70, 71], propagation characteristics [72] and the vector nature of their polarisation distribution. Furthermore, it has been shown that fragmentation of OAM beams during propagation in a self-focussing Kerr medium can be inhibited, without altering the nonlinear confinement by using vector superpositions of OAM beams rather than scalar beams. In such cases FSL beams can propagate significantly further than their scalar counterparts [11]. These properties together with the ability to obtain a desired spatial intensity profile and polarisation structure have been found useful in a wide array of applications such as material processing, stimulated emission depletion and confocal microscopy [73–76], optical trapping and manipulation [77, 78], atomic state preparation, manipulation and detection [77, 79, 80], optical communication [11, 81] and even in classical entanglement [82–84]. Additionally, novel focussing properties of distinct polarisation distributions lead to tighter focussing of given modes and strong axial field components that are of use in microscopy, optical trapping [85] and as a mechanism for linear accelerators. Thus it is of importance to understand the mechanisms that affect the spatial distribution of both the intensity and polarisation of the FSL beams.

Of particular interest in this chapter is the effect of propagation (linear and nonlinear) on the evolution of the polarisation distribution and nonlinear confinement of FSL beams. We aim to explain the mechanisms behind the rotation of the polarisation and, by understanding and highlighting the factors that affect the beams behaviour during propagation, we show that by selection of experimental parameters the rotation of the polarisation can be predicted and controlled.

In Section 4.3 we begin with analysis for a linear propagation of FSL and detail the behaviour of the polarisation structure. Linear propagation has been studied previously for the case of low-order Poincaré beams $\ell_R = 1$ and $\ell_L = 0$, where the polarisation experiences a uniform rotation in orientation of $\pi/2$ as it propagates from a beam waist $z = 0$ to the far field [28]. Here, we give an analytical derivation that gives an expression for the orientation of the polarisation at each point on the transverse plane and its rotation during linear propagation, generalised such that the rotation of

polarisation for all FSL beams can be calculated. The result is shown to depend purely on the difference in Gouy phase experienced between the two eigenmodes comprising the FSL resulting in a uniform rotation across the transverse plane where each point on the transverse plane rotates by the same amount. We show excellent agreement with numerical results and highlight the difference between the rotation of the individual points in the transverse plane and the polarisation distribution as a whole. The section is concluded with the introduction of radial modes ($p > 0$) into the FSL composition and detailing the effect that the radial modes have on the polarisation rotation.

In Section 4.4 we consider the propagation of FSL in self-focussing nonlinear media. The Kerr medium is shown to induce a cross-phase modulation between the modes in the FSL superposition which attempts to maximise the spatial overlap between the modes. The rotation of the orientation of the polarisation at each point in the transverse field is no longer homogeneous which in turn results in a non-trivial measurement of the rotation as the spatial overlap is not constant. We justify an averaging method of measuring the rotation of the polarisation for a given FSL beam and compare the behaviour of the polarisation between the linear and nonlinear propagation cases. Different vector compositions with the same net OAM are shown to generate different polarisation rotations upon nonlinear propagation and this is attributed to the different spatial profiles and the spatial overlaps between the eigenmodes in the different superpositions. Cylindrical vector (CV) beams do not present any rotation as they have the same magnitude of OAM and identical spatial profiles in both of the modes in the FSL beam.

Finally in Section 4.4.4 we detail the physical parameters that can control the behaviour of the polarisation during propagation such as input power, temperature (or nonlinearity) of the medium and the beam waist of the vector modes and show that any desirable behaviour in the rotation polarisation structure can be achieved and controlled. We also show that the introduction of nonlinearity not only can change the amount of polarisation rotation for beams with a net OAM, but for CV beams with zero net OAM, by introducing a bias between the amplitudes within the superposition.

Any difference in amplitude between the two modes breaks the spatial symmetry and in turn introduces rotation in polarisation during propagation, such that CV beams with radial polarisation can be converted to spiral and azimuthal polarisation distributions. This may be of use in advancing polarisation measurements and manipulation of atoms [80].

4.2 Numerical Model

4.2.1 Normalised Nonlinear Schödinger Equation

As we are interested in the behaviour of the FSL beams during propagation in nonlinear Kerr media we begin from the paraxial wave equation derived in Section 2.2 of Chapter 2 and rearrange Eq.(2.28) such that we obtain an expression for the evolution of the beam along the direction of propagation as

$$\frac{\partial \mathbf{A}}{\partial z} = \frac{i}{2k}\nabla_{\perp}^{2}\mathbf{A} + \frac{i\omega^{2}}{2k\varepsilon_{0}c^{2}}\mathbf{P}. \tag{4.1}$$

We introduce the following scaled co-ordinates

$$\eta = \sqrt{\frac{k}{z_R}}x, \tag{4.2}$$

$$\xi = \sqrt{\frac{k}{z_R}}y, \tag{4.3}$$

$$\zeta = \frac{1}{z_R}z, \tag{4.4}$$

where z_R is the Rayleigh length, or effective diffraction length for the beam, such that our co-ordinates are normalised and scaled by the characteristic diffraction length of the beam. The relative derivatives with respect to these scaled co-ordinates are then

$$\frac{\partial^2}{\partial \eta^2} = \frac{z_R}{k}\frac{\partial^2}{\partial x^2}, \tag{4.5}$$

$$\frac{\partial^2}{\partial \xi^2} = \frac{z_R}{k}\frac{\partial^2}{\partial y^2}, \tag{4.6}$$

$$\frac{\partial}{\partial \zeta} = z_R\frac{\partial}{\partial z}, \tag{4.7}$$

Substituting these scaled co-ordinates and their respective derivatives into Eq(5.2) we can write the normalised NLSE as

$$\frac{\partial \mathbf{A}}{\partial \zeta} = \frac{i}{2}\nabla_\perp^2 \mathbf{A} + \frac{i\omega^2 z_R}{2k\varepsilon_0 c^2}\mathbf{P}. \tag{4.8}$$

4.2.2 Nonlinear Polarisation and the Susceptibility Tensor

We now require an expression for the form of the nonlinear polarisation response $\mathbf{P}$ for a Kerr $\left(\chi^{(3)}\right)$ medium. Recall that the polarisation can be written as a power series in terms of the relative susceptibilities and electric field from Eq.(2.7) as

$$\mathbf{P} = \varepsilon_0 \left[\chi^{(1)}\mathbf{E} + \chi^{(2)}\mathbf{E}^2 + \chi^{(3)}\mathbf{E}^3 ..\right] \tag{4.9}$$

$$= \varepsilon_0\chi^{(1)}\mathbf{E} + \mathbf{P}^{NL} \tag{4.10}$$

where ε_0 is the permittivity of free space and the orders of χ are the relative susceptibilities of the medium. For a Kerr medium, due to the inversion symmetry of the medium, the even orders of the electric susceptibility in $\chi^{(n)}$ are zero. This means that we only include the linear contribution to the polarisation as well as the most significant nonlinear term $\chi^{(3)}$ in the nonlinear polarisation, $\mathbf{P}^{NL}$. Because we are considering the full complex vector natures of the fields the susceptibilities represented by the χ terms

take the form of tensors relating the amplitudes of the electric fields with the polarisation. In the case presented here the linear susceptibility $\chi^{(1)}$ takes on the form of a 3x3 second order tensor and the third order nonlinear susceptibility $\chi^{(3)}$ is a fourth order tensor of the form 3x3x3x3 such that it can relate all the permutations of $\mathbf{E}$ that contribute to the polarisation. The nonlinear polarisation term in Eq.(4.10) can then be written as

$$\mathbf{P}_i^{NL}(\omega_4 = \omega_1 + \omega_2 + \omega_3) = \epsilon_0 \sum_{jkl} \sum_{123} \chi^{(3)}_{ijkl}(\omega_4; \omega_1, \omega_2, \omega_3) \mathbf{E}_j(\omega_1) \mathbf{E}_k(\omega_2) \mathbf{E}_l(\omega_3) \quad (4.11)$$

which when summed over 1,2 and 3 gives

$$\mathbf{P}_i^{NL}(\omega_4 = \omega_1 + \omega_2 + \omega_3) = \varepsilon_0 D^{(3)} \sum_{jkl} \chi^{(3)}_{ijkl}(\omega_4; \omega_1, \omega_2, \omega_3) E_j(\omega_1) E_k(\omega_2) E_l(\omega_3), \quad (4.12)$$

where D^3 is known as the degeneracy factor and gives the number of distinct permutations of the applied fields $[\mathbf{E}_j; \mathbf{E}_k; \mathbf{E}_l]$ and $\chi^{(3)}_{ijkl}$ is the third order nonlinear susceptibility tensor. The degeneracy factor takes the values

$$D^{(3)} = \begin{cases} 1 & \text{One distinct field} \\ 3 & \text{Two distinct fields} \\ 6 & \text{All fields are distinct.} \end{cases} \quad (4.13)$$

In our case we are considering the nonlinear propagation of a vector superposition of two distinct LG modes ($D^{(3)} = 3$) that propagate with the same frequency along the same axis. This requirement imposes restrictions on ω_4 in that the nonlinear polarisation response takes on the frequency of the two modes in the vector superposition requiring

that $\omega_4 = \omega + \omega - \omega = \omega$. Including the degeneracy factor for our case and imposing the restriction on ω_4 we can write the nonlinear polarisation in the form

$$\mathbf{P}_i^{NL}(\omega = \omega + \omega - \omega) = 3\varepsilon_0 \sum_{jkl} \chi^{(3)}_{ijkl}(\omega; \omega, \omega, -\omega) E_j(\omega) E_k(\omega) E_l(-\omega), \tag{4.14}$$

where the field with negative frequency indicates that the conjugate of the complex fields should be taken i.e. $E(-\omega) = E^*(\omega)$. We now consider the medium to be isotropic which means the properties of the medium are identical along each of the *x,y,z* axis. Considering the tensor nature of the nonlinear susceptibility this implies

$$\chi^{(3)}_{xxxx} = \chi^{(3)}_{yyyy} = \chi^{(3)}_{zzzz} \tag{4.15}$$

such that the susceptibility is the same along each of the axis. By symmetry there are only three distinct independent non-zero components along any axis, for example the x-axis

$$\chi^{(3)}_{xxxx} = \chi^{(3)}_{xxyy} + \chi^{(3)}_{xyxy} + \chi^{(3)}_{xyyx} \tag{4.16}$$

The implications of Eq.(4.15) and Eq.(4.16) reduce the number of terms required to completely define the susceptibility tensor in Eq.(4.14) and we can write it as

$$\chi^{(3)}_{ijkl} = \chi^{(3)}_{xxyy}(\delta_{ij}\delta_{kl}) + \chi^{(3)}_{xyxy}(\delta_{ik}\delta_{jl}) + \chi^{(3)}_{xyyx}(\delta_{il}\delta_{jk}), \tag{4.17}$$

where δ_{ab} is a delta function which is equal to 1 when $a = b$, and zero otherwise. The transverse Cartesian components of the nonlinear polarisation can then be written as

$$\begin{aligned} P_i^{NL} &= 3\varepsilon_0\Big[\chi^{(3)}_{xxyy}(|E_x|^2+|E_y|^2)E_i + \chi^{(3)}_{xyxy}(|E_x|^2+|E_y|^2)E_i \\ &+ \chi^{(3)}_{xyyx}(E_xE_x+E_yE_y)E_i^*\Big], \end{aligned} \tag{4.18}$$

with $i = x, y$. This can be more concisely written in vector form,

$$\mathbf{P}^{NL} = 3\varepsilon_0\Big[\left(\chi^{(3)}_{xxyy}+\chi^{(3)}_{xyxy}\right)(\mathbf{E}\cdot\mathbf{E}^*)\mathbf{E} + \chi^{(3)}_{xyyx}(\mathbf{E}\cdot\mathbf{E})\mathbf{E}^*\Big], \tag{4.19}$$

with the transverse vectors defined as $\mathbf{A} = A_x\mathbf{x} + A_y\mathbf{y}$. It is important to note that the terms on the right-hand side of Eq.(4.19) give polarisations with opposite handedness. We now assume that each of the independent non zero components contribute equally to the total susceptibility tensor $\chi^{(3)}_{xxyy} = \chi^{(3)}_{xyyx} = \chi^{(3)}_{xyxy} = \frac{1}{3}\chi^{(3)}_{xxxx}$ as Agarwal does in [86], such that Eq.(4.19) becomes

$$\mathbf{P}^{NL} = 3\varepsilon_0\chi^{(3)}_{xxxx}\left[\frac{2}{3}(\mathbf{E}\cdot\mathbf{E}^*)\mathbf{E} + \frac{1}{3}(\mathbf{E}\cdot\mathbf{E})\mathbf{E}^*\right], \tag{4.20}$$

which can be expanded and re-arranged by taking the term $(E_iE_i)E_i^*/3$ from the last product in Eq.(4.20) and re-inserting it as $|E_i|^2E_i/3$ to find,

$$P_i^{NL} = 3\varepsilon_0\chi^{(3)}_{xxxx}\left[\left(|E_i|^2+\frac{2}{3}|E_j|^2\right)E_i + \frac{1}{3}(E_jE_j)E_i^*\right], \tag{4.21}$$

with $i, j = x, y$ and $i \neq j$.

4.2.3 Circular Basis

As we will be using circularly polarised Laguerre-Gauss modes as the foundation of creating the FSL modes it is convenient to write the NLSE using a circular basis. The unit vectors for a circular basis are defined in terms of the Cartesian vectors as

$$\mathbf{e}_+ = \mathbf{e}_L = \frac{(\mathbf{x} + i\mathbf{y})}{\sqrt{2}}, \tag{4.22}$$

$$\mathbf{e}_- = \mathbf{e}_R = \frac{(\mathbf{x} - i\mathbf{y})}{\sqrt{2}}, \tag{4.23}$$

$$\mathbf{e}_0 = \mathbf{e}_z = \mathbf{z}. \tag{4.24}$$

The transverse circular unit vectors, Eq(4.22) & Eq(4.23), are complex and have the following properties:

$$\mathbf{e}_\pm \cdot \mathbf{e}_\pm = 0, \tag{4.25}$$

$$\mathbf{e}_\pm \cdot \mathbf{e}_\mp = 1, \tag{4.26}$$

$$\mathbf{e}_\pm^* = \mathbf{e}_\mp. \tag{4.27}$$

Any transverse vector field can then be decomposed in terms of its left- and right-handed circular components,

$$\mathbf{E} = E_L\mathbf{e}_L + E_R\mathbf{e}_R. \tag{4.28}$$

Using this decomposition, and the rules given in Eq(4.25) & (4.26), we can convert the Cartesian components of the nonlinear polarisation given in Eq.(4.20). First, we expand the two vector product terms on the right-hand side of the equation,

$$\begin{aligned} (\mathbf{E} \cdot \mathbf{E}^*) &= (E_L\mathbf{e}_L + E_R\mathbf{e}_R) \cdot (E_L^*\mathbf{e}_L^* + E_R^*\mathbf{e}_R^*), \\ &= (|E_L|^2 + |E_R|^2), \end{aligned} \tag{4.29}$$

$$\begin{aligned} (\mathbf{E} \cdot \mathbf{E}) &= (E_L\mathbf{e}_L + E_R\mathbf{e}_R) \cdot (E_L\mathbf{e}_L + E_R\mathbf{e}_R), \\ &= (2E_LE_R). \end{aligned} \tag{4.30}$$

Next, by considering the circularly polarised components of the polarisation vector ($\mathbf{P} = P_L\mathbf{e}_L + P_R\mathbf{e}_R$) we can succinctly define the components of Eq.(4.20) as,

$$\begin{aligned} P^{NL}_{L,R} &= 2\varepsilon_0\chi^{(3)}_{xxxx}\left[(|E_L|^2 + |E_R|^2)E_{L,R} + (E_L E_R)E^*_{R,L}\right], \\ &= 3\varepsilon_0\left[|E_{L,R}|^2 + 2|E_{R,L}|^2\right]E_{L,R}. \end{aligned} \tag{4.31}$$

Finally we substitute the form of the nonlinear polarisation response into Eq(eq:NLSEmodel) to obtain a full expression for the description of propagation in a $\chi^{(3)}$ medium as

$$\frac{\partial E_{L,R}}{\partial \zeta} = \frac{i}{2}\nabla^2_\perp E_{L,R} + \frac{3i\omega^2 z_R}{2kc^2}\left[|E_{L,R}|^2 + 2|E_{R,L}|^2\right]E_{L,R}.. \tag{4.32}$$

It is well known that, in (2+1) dimensions, spatial solitons are unstable in homogeneous Kerr media. Self-focussing in such models lead to a blow up in the amplitude of the fields which is a phenomenon known as collapse where the model becomes numerically unstable [87]. One way to increase their stability is to use a saturating nonlinearity and consider a saturable self-focussing medium to prevent catastrophic collapse due to the self-focussing. As such we use a model based on the same considerations but with a saturating term as in [11]

$$\frac{\partial E_{L,R}}{\partial \zeta} = \frac{i}{2}\nabla^2_\perp E_{L,R} + i\mu\frac{|E_{L,R}|^2 + 2\,|E_{R,L}|^2}{1 + \sigma\left(|E_{L,R}|^2 + 2\,|E_{R,L}|^2\right)}E_{L,R}, \tag{4.33}$$

where the important parameters are the nonlinear parameter, μ, and the saturation parameter, σ, which are given by:

$$\mu = \frac{2k_0^2 n_2 P_0}{3n_0}; \qquad \sigma = \frac{4P_0}{3I_{sat}w_0^2}, \tag{4.34}$$

respectively where k_0 is the free space wave number, n_0 and n_2 are the linear and nonlinear refractive indices, I_{sat} is the saturation intensity of the medium and P_0 is the

power of the incident laser beam. All other terms in Eq.(4.33) and Eq.(4.34) are as defined previously.

4.3 Linear Propagation

4.3.1 Analytical analysis of polarisation rotation.

Recall that FSL beams are given by Eq(2.38). For linear propagation we can use this to determine an analytical expression for the form of the FSL as a function of the propagation distance, z. This allows calculation of the Stokes parameters at any point on the transverse plane at any value of z. As we are particularly interested in the rotation of the polarisation structure we can use the stokes parameters to define the orientation of the polarisation as a function of propagation distance, z, from Eq(2.47) such that the orientation, ψ is defined as

$$\psi = \frac{1}{2}\tan^{-1}\left[\frac{S_2}{S_1}\right] = \frac{1}{2}\tan^{-1}\left[\frac{\Im\left[\mathbf{E}_R^*\mathbf{E}_L\right]}{\Re\left[\mathbf{E}_R^*\mathbf{E}_L\right]}\right], \tag{4.35}$$

where $\mathbf{E}_{R,L}$ are the right and left hand circularly polarised modes in the FSL beam respectively and take on the form of Laguerre-Gauss modes as in Eq(2.35), $\Re$ and $\Im$ represent the real and imaginary parts and * is the complex conjugate. From Eq(2.38) we can define the FSL beam and E_R and E_L as

$$\mathbf{E} = \mathbf{E}_R + \mathbf{E}_L; \quad \mathbf{E}_R = \sin(\gamma)\mathbf{LG}_{p_R}^{\ell_R}\mathbf{e}_R; \quad \mathbf{E}_L = \exp[i\beta]\cos(\gamma)\mathbf{LG}_{p_L}^{\ell_L}\mathbf{e}_L, \tag{4.36}$$

and by using the form of the Laguerre-Gauss modes in Eq(2.35) we can calculate the relevant term $\mathbf{E}_R^*\mathbf{E}_L$ to obtain

$$\begin{aligned}
\mathbf{E}_R^*\mathbf{E}_L &= \sin(\gamma)\cos(\gamma)A^2(r,z)\exp\left[i(\ell_L-\ell_R)\phi\right] \\
&\times \exp\left[i(2(p_R-p_L)+|\ell_R|-|\ell_L|)\eta(z)\right]\exp\left[i\beta\right], \qquad (4.37)\\
\Re[\mathbf{E}_R^*\mathbf{E}_L] &= \sin(\gamma)\cos(\gamma)A^2(r,z) \\
&\times \cos\left[(\ell_L-\ell_R)\phi-(2(p_R-p_L)+|\ell_R|-|\ell_L|)\,\eta(z)+\beta\right], \qquad (4.38)\\
\Im[\mathbf{E}_R^*\mathbf{E}_L] &= \sin(\gamma)\cos(\gamma)A^2(r,z) \\
&\times \sin\left[(\ell_L-\ell_R)\phi-(2(p_R-p_L)+|\ell_R|-|\ell_L|)\,\eta(z)+\beta\right] \qquad (4.39)
\end{aligned}$$

where we have simplified the amplitude terms in the form of the Laguerre-Gauss modes such that

$$A(r,z)=\sqrt{\frac{2p!}{\pi(p+|\ell|)!}}\frac{1}{w(z)}\left(\frac{r\sqrt{2}}{w(z)}\right)^{|\ell|}L_p^{|\ell|}\left(\frac{2r^2}{w^2(z)}\right)\exp\left(\frac{-r^2}{w^2(z)}\right).$$

Finally by substituting Eq(4.38) and Eq(4.39) into Eq(4.35) we can define the orientation of the polarisation as a function of propagation z as

$$\begin{aligned}
\psi(z) &= \frac{1}{2}\tan^{-1}\left[\frac{\sin\left[(\ell_L-\ell_R)\phi-(2(p_R-p_L)+|\ell_R|-|\ell_L|)\,\eta(z)+\beta\right]}{\cos\left[(\ell_L-\ell_R)\phi-(2(p_R-p_L)+|\ell_R|-|\ell_L|)\,\eta(z)+\beta\right]}\right] \\
&= \frac{1}{2}\left[(\ell_L-\ell_R)\phi-(2(p_R-p_L)+|\ell_R|-|\ell_L|)\,\eta(z)+\beta\right]. \qquad (4.40)
\end{aligned}$$

As can be seen above all amplitude terms cancel, as do exponential terms that do not involve the OAM and radial number of the modes. We can break this result down into two important parts; terms independent of the propagation distance z and those that evolve with propagation. The initial orientation of the polarisation at the beam waist ($z=0$) is given by

$$\psi(0)=\frac{1}{2}\left[(\ell_L-\ell_R)\phi-\beta\right]$$

and contains all the terms independent of z. Physically this means that the initial orientation of each polarisation ellipse in the transverse plane is purely dependent on the difference in OAM between E_L and E_R as well as any initial phase difference β between the modes in the superposition. The azimuthal angle ϕ gives the spatial dependence of the polarisation structure. Since all terms in $\psi(0)$ don't have any dependence on z, they are constant during propagation and do not contribute to any rotation or change in behaviour of the polarisation structure during propagation. For a linear propagation of a FSL beam from the beam waist to a distance z the change in orientation of the polarisation ellipse at each point, i.e the rotation of the polarisation, at each point is given by:

$$\begin{aligned} \Delta\psi(z) &= \psi(z) - \psi(0) && (4.41)\\ &= \frac{1}{2}\left[(2(p_R - p_L) + |\ell_R| - |\ell_L|)\eta(z)\right] && (4.42)\\ &= \left(\Delta p_{R,L} + \frac{1}{2}\Delta|\ell_{R,L}|\right)\eta(z), && (4.43) \end{aligned}$$

where $\Delta p_{R,L} = p_R - p_L$ is the difference in radial number and $\Delta|\ell_{R,L}| = |\ell_R| - |\ell_L|$ is the difference in the magnitude of the OAM between the two modes in the vector superposition. The expression for the rotation of the polarisation contains all the terms from Eq.(4.40) that evolve with propagation and interestingly gives the difference in Gouy phase between the two modes in the FSL superposition. Hence for a linear propagation the rotation of the polarisation is simply the change in phase difference between the two modes which is purely dependent on the difference in radial number and the difference in magnitude of OAM between E_R and E_L. This is unsurprising since for two beams that have a different Gouy phase the result is an evolving phase difference between the beams which in essence is the same as changing β in $\psi(0)$ which corresponds to a change in orientation of the polarisation ellipse. Note that both the initial orientation of the polarisation and the net rotation during propagation are independent of the amplitudes of the two modes and dependent purely on the difference

in their OAM and radial number. Since $\eta(z)$ is independent of the azimuthal angle and spatial location in the transverse plane the magnitude of rotation is the same for *all* points in the beam since. This analysis is for the rotation of the polarisation at each point in the beam, the rotation of the polarisation structure as a whole is dependent on the cylindrical symmetry of the distribution as we will show in a later section. Initially for simplicity we only consider LG beams without radial modes such that $p = 0$ which simplifies the rotation for linear propagation to

$$\Delta\psi(z) = \frac{1}{2}\Delta|\ell_{R,L}|\eta(z). \tag{4.44}$$

For such vector beams propagating from $z = 0$ to the far field, the rotation of the polarisation will asymptote, since

$$\eta(z) = \tan^{-1}\left(\frac{z}{z_R}\right) \xrightarrow[z\to\infty]{} \frac{\pi}{2},$$

which means that the rotation itself asymptotes

$$\Delta\psi(z) \xrightarrow[z\to\infty]{} \frac{\pi}{4}\Delta|\ell_{R,L}|,$$

Figure.(4.1) gives the rotation in the orientation of the polarisation for vector beams of varying $\Delta|\ell_{R,L}|$ propagating from $z = -10z_R$ through the beam waist $z = 0$ to $z = 10z_R$. The dashed lines show the respective asymptotes for each curve at $\frac{\pi}{4}|\ell_{R,L}|$, where the particular value of OAM of the eigenstates in the superposition is not important, only the difference in their magnitude. For example, a fully structured light beam composed of $\ell_R = 3$ and $\ell_L = 1$ will experience the same polarisation rotation across all points on the transverse plane as one composed of a superposition of $\ell_R = 5$ and $\ell_L = -3$. This means cylindrical vector beams, which by definition have the same magnitude of OAM in the right and left hand circularly polarised modes such that $\Delta|\ell_{R,L}| = 0$, experience no polarisation rotation or change in distribution during linear propagation. Since the rotation of the polarisation only depends on the difference in Gouy phase we

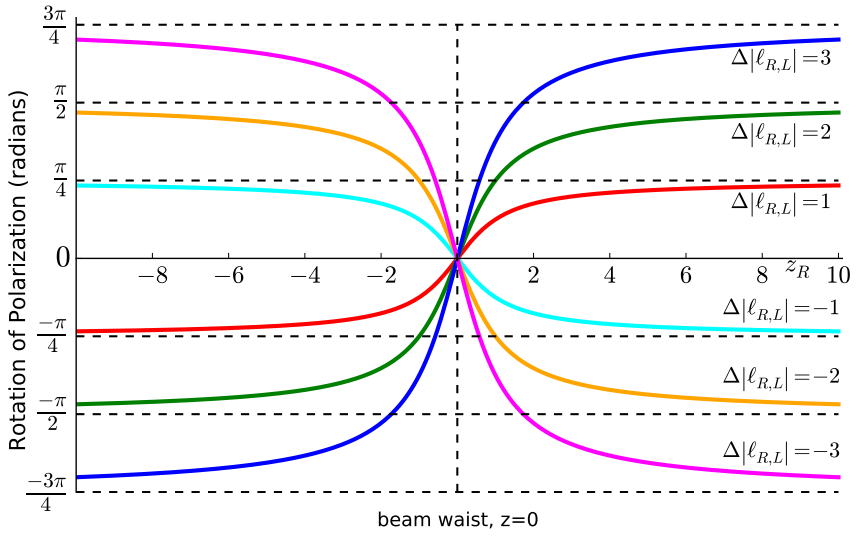

FIGURE 4.1: Magnitude of the rotation of polarisation ellipses calculated analytically from Eq.(4.44) from $z = -10z_R$ through the beam waist to a propagation distance of $z = 10z_R$ for different FSL compositions of $\Delta|\ell_{R,L}|$ = -3 (magenta), -2 (orange), -1 (cyan), 1 (red), 2 (blue) and 3 (green). The horizontal dashed black lines represent the relevant asymptotes of the rotation curves and the vertical dashed black line represents the beam waist at z=0.

can compare this graph with that of the Gouy phase for a Laguerre-Gaussian beam in Figure.(2.6) and see that the rotation curves for a linear propagation are the same, just scaled by the difference in magnitude of the OAM in each of the eigenstates of the vector superposition and nearly all the rotation occurs within a few Rayleigh lengths of the beam waist. In the nonlinear section we will focus on this region within $\pm 3z_R$ where most of the rotation occurs.

4.3.2 Numerical Comparison of Polarisation Rotation.

We can numerically analyse the behaviour of FSL beams during a linear propagation, by numerical integration of Eq.(4.33) but without the nonlinearity, $\mu = 0$, such that a linear propagation is described by a simplified model of:

$$\frac{\partial E_{L,R}}{\partial \zeta} = \frac{i}{2}\nabla_{\perp}^{2} E_{L,R}, \tag{4.45}$$

which just describes the diffraction of the beam, where all terms are the same as defined in Eq.(4.33). Numerically we calculate the orientation of the polarisation by calculating the Stokes parameters at each of the points in the field in the transverse plane at fixed distances during linear propagation use the expression for ψ in Eq.(2.47). The rotation of the polarisation, just as in the analytical calculation, is then just the change in angle at propagation distance z from the initial orientation, which can be calculated at each propagation step for all points in the transverse plane. We also note that we add a small amount of noise in the initial condition of the simulation. Because of the diffraction of the beam, for a linear propagation the intensity of the beam decreases with propagation distance and when the magnitude of the intensity becomes comparable with the initial noise on the beam the measurement of the Stokes parameters and hence the rotation of the polarisation becomes subject to noise and no longer an accurate representation for the behaviour of the polarisation. Because higher order modes have a larger radius and their initial intensity is lower this effect is more pronounced as the OAM of the mode increases. Furthermore for the numerical simulations periodic boundary conditions are used and when the underlying phase of the beam propagates to the boundary it can interfere with itself again resulting in behaviour that is not representative of the polarisation. Again this effect is more pronounced for larger OAM modes. We choose beams that are small with respect to the domainwidth of the simulation such that the boundary does not have any influence on the behaviour of the beam.

Numerically this means that we can only track the rotation of the polarisation over a finite propagation distance and this distance decreases the larger the OAM involved in the vector beam. For the level of noise and domain size used in the simulations for linear and nonlinear propagation in this work and for an OAM of 1, the rotation can be tracked for approximately 15 Rayleigh ranges. However this quickly decreases to around 6 Rayleigh ranges for an OAM of 4. For this reason, the lowest composition of OAM

modes are used in the numerical data in Figure.(4.2), i.e. $\ell_R = \Delta|\ell_{R,L}|$ and $\ell_L = 0$, such that the polarisation rotation can accurately be determined over the maximum propagation distance.

Figure.(4.2) shows the comparison between the analytical and numerical measurements for the polarisation rotation. Since the rotation is uniform and rigid across the transverse plane for linear propagation, each of the rotation curves for all the points in the field are identical and hence we need only pick one of the points to represent the behaviour of the polarisation. The numerical measurements are shown up until the point where the measurement of rotation is no longer accurate; the magnitude of intensity is comparable with the noise. The analytical result is shown from the beam waist up to 10 Rayleigh lengths, $z = 10z_R$. It can be seen there is excellent agreement between the analytical and numerical results up to appropriate propagation distances. It is also important to note that although for Figure.(4.2), we have shown only cases for $\ell_R > \ell_L$, the results are symmetric about the x-axis and for $\ell_L > \ell_R$ the polarisation orientation will rotate in the opposite direction just as in Figure.(4.1).

4.3.3 Polarisation Orientation and Structure

The previous analysis of polarisation behaviour focused on the change in orientation of the polarisation ellipse at each individual point in the transverse plane. Figure.(4.3) shows the polarisation distributions for two FSL beams, with $\Delta|\ell_{R,L}| = 1$, initially at the beam waist and after a linear propagation of 20 Rayleigh lengths such that the rotation of the polarisation structure has sufficiently asymptoted and there will be negligible rotation upon further propagation. The beam on the top row in (a) and (b) is referred to as a lemon beam and has the vector superposition $\ell_R = 1$ and $\ell_L = 0$ [11] and the bottom row in (c) and (d) is referred to as a star beam composed of $\ell_R = -1$ and $\ell_L = 0$ [11]. As expected, for both vector beams, each point in the polarisation structure has had its orientation rotated by $\frac{\pi}{4}$ or 45° since for both examples $\Delta|\ell_{R,L}| = 1$. As expected for both beams the polarisation ellipse at each point in the transverse plane has rotated by $\Delta\psi = \frac{\pi}{4}\Delta|\ell_{R,L}| = \frac{\pi}{4}$ or 45°. This is an analytical calculation where

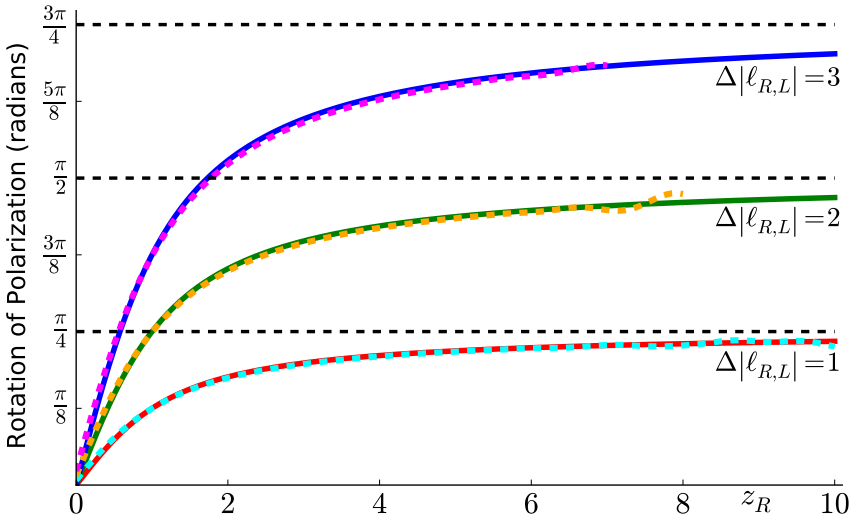

FIGURE 4.2: Comparison between the analytical and numerical results for the polarisation rotation of selected FSL modes. The analytical results are shown in the solid lines over a propagation distance of $10z_R$ and the numerical results are overlayed in the dashed lines up to a propagation distance where noise starts affecting the curve. The FSL modes shown are composed of $\Delta\,|\ell_{R,L}| = 1$ (red, cyan), 2 (green, orange) and 3 (blue, magenta). The dashed horizontal lines represent the relevant asymptotes for each of the modes.

we have ignored the effect of diffraction on the intensity of the beam for clarity such that each of the images can easily be compared. We note that this does not affect the polarisation rotation in any way.

Interestingly however, the behaviour of the polarisation structure as a whole pattern in the transverse plane is different between the two beams. By considering the structure as a whole and we can another interesting behaviour of the polarisation during propagation. For the lemon beam, the polarisation pattern *appears* to have rotated counter-clockwise by $\frac{\pi}{2}$, twice that of the rotation in orientation of each individual point, and for the star beam, the the pattern *appears* to have rotated counter-clockwise $\frac{\pi}{4}$, the same as the rotation of each individual point and half that of the lemon beam. Hence it is clear that although each point rotates by Eq.(4.44), the rotation of the structure as a whole changes depending on the vector superposition. Comparing the rotation of other polarisation structures reveals that it is the rotational symmetry of the

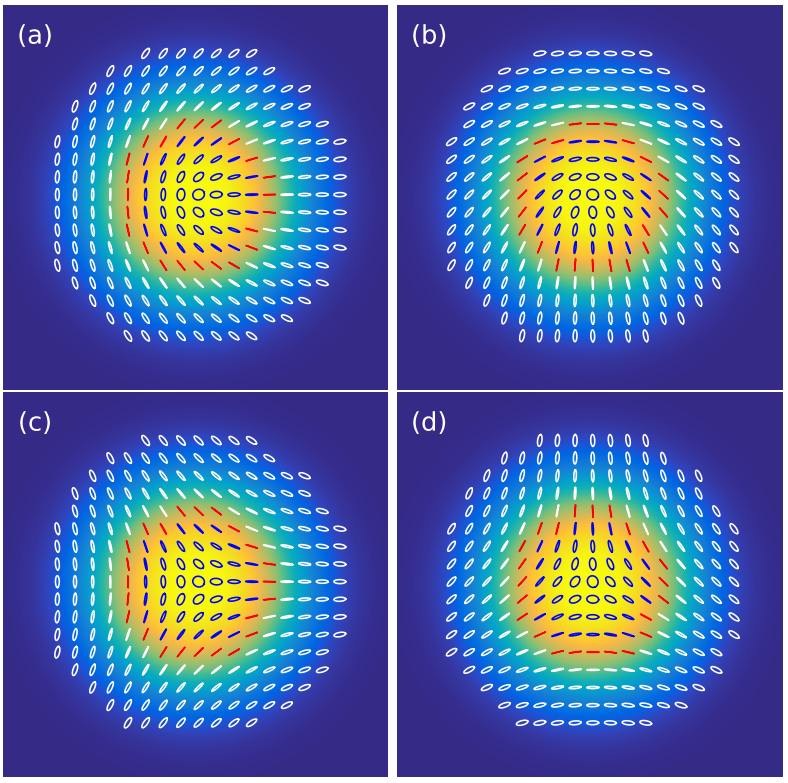

FIGURE 4.3: Polarisation distribution for a lemon beam composed of $\ell_R = 1$ and $\ell_L = 0$ at a linear propagation distance of z=0 in (a) and after a propagation distance of z=20z_R in (b) such that the rotation of the polarisation ellipses has sufficiently asymptotes and reached its final state. The bottom row (c) and (d) shows the same for a star beam which is a superposition of $\ell_R = -1$ and $\ell_L = 0$ at the same propagation distances. Note that the diffraction of the beam has no effect on the polarisation distribution or its rotation hence has been neglected here for simple comparison of the images.

pattern that gives rise to the behaviour of the structure as a whole and the behaviour of each point is given determined by the difference in magnitude of OAM between the eigenmodes as in Eq(4.44). There is no clear rule governing the spatial symmetry of the polarisation pattern and the rotation of its structure. In fact, for certain polarisation distributions, the structure can appear to rotate in the opposite direction to that in which the polarisation points are rotating.

4.3.4 Radial Modes

For completeness we now consider FSL beams that involve vector superpositions of LG beams that can contain radial modes where $p > 0$. The result of including radial modes further decreases the initial intensity of the beam and combined with the diffraction from linear propagation means that the distance over which the polarisation rotation can accurately be evaluated is further decreased. Again we consider only the simplest lowest order OAM and radial numbers. From Eq.(4.43) the radial number of the eigenmodes has twice the effect on the rotation of polarisation that the magnitude of the OAM. Consider a lemon beam ($\ell_R = 1$ and $\ell_L = 0$) whose polarisation behaviour follows the red/cyan curve in Figure.(4.2) and transverse polarisation structure is shown in Figure.(4.3). If we increase the radial number of the right circularly polarised mode ($p_R = 1$) then the rotation now rotates as $\Delta\psi(z) = \frac{3}{2}\eta(z)$, i.e expected to follow the blue/magenta curve in Figure.(4.2), three times the magnitude of rotation as the initial lemon beam. Instead if the radial number of the left circularly polarised mode is increased (p_L=1) then the rotation of the polarisation will follow $\Delta\psi(z) = -\frac{1}{2}\eta(z)$ which has the same magnitude of rotation as the original lemon beam but in the opposite direction. Figure.(4.4) shows both the analytical and numerical evaluation of the rotation for each of the cases discussed, again in excellent agreement. Figure.(4.5) shows the corresponding transverse profiles and polarisation states at the beam waist and after linear propagation of 20 Rayleigh lengths for both the $p_R = 1$ (top row) and $p_L = 1$ (bottom row) vector beams. The rotation of the polarisation ellipse at each of the points can be seen to match very well with the above predictions. Because the superposition with $p_R = 1$ asymptotes to a rotation of $3\pi/4$ and that with $p_L = 1$ rotates by $\pi/4$ in the opposite direction after propagation to the far field it should appear that they have rotated to the same final polarisation state as can be seen by the transverse polarisation profiles.

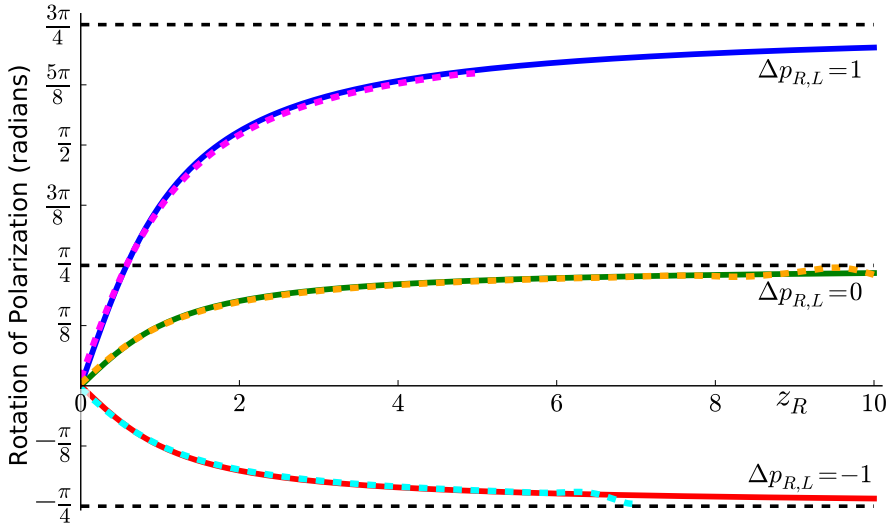

FIGURE 4.4: Magnitude of rotation of the polarisation for FSL modes composed of $\Delta|\ell_{R,L}|$ = and Δp_{R_L} = -1 (green, orange) 0 (red, cyan) and 1 (blue, magenta). The solid lines are calculated from Eq.(4.43) over 10 Rayleigh lengths and the overlayed dashed lines are the numerical results. The red and cyan lines are the same as in Figure.(4.2).

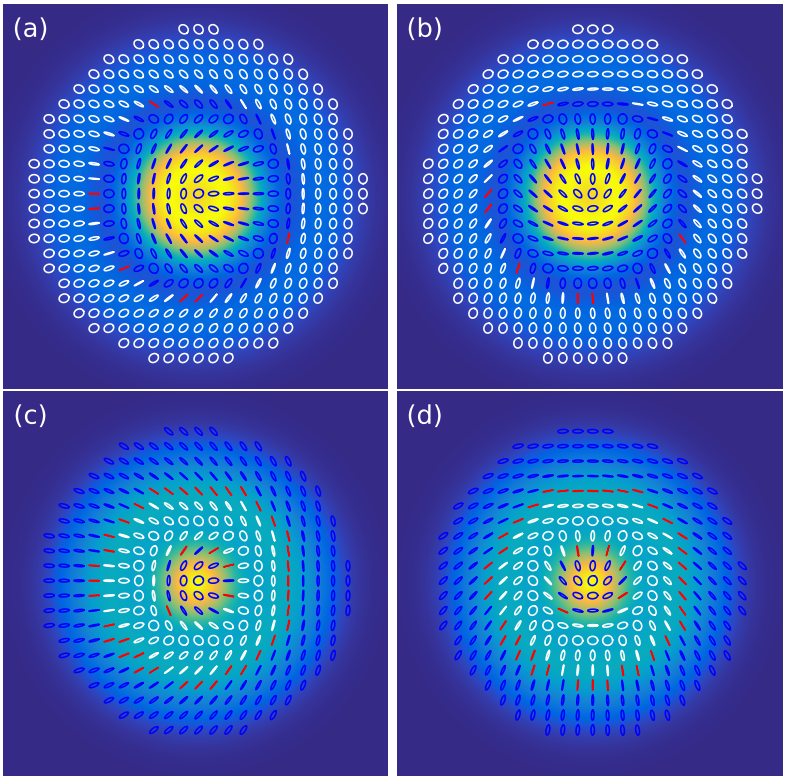

FIGURE 4.5: Polarisation distributions for a lemon beam from Figure.(4.3) but with the addition of a radial number $p_R = 1$ in (a)-(b) and $p_L = 1$ in (c)-(d). Again the polarisation states are shown at z=0 and z=$20z_R$ and diffraction has been neglected for simple comparison of the images. Each of the points in the top row (a)-(b) have rotated clockwise by $\frac{3\pi}{4}$ and in the bottom row (c)-(d) have rotated anti-clockwise by $\frac{\pi}{4}$. The distributions as a whole appear to have rotated anti-clockwise by $\frac{\pi}{2}$.

4.4 Nonlinear Propagation

4.4.1 Cross-phase Modulation and Spatial Overlap

For nonlinear propagation of fully structured light, evaluating the rotation of the polarisation structure is no longer trivial. In the case of linear propagation there is no coupling between the modes in the beam and they propagate independently such that their spatial overlap remains constant with propagation. The rotation of the polarisation is uniform across all points in the beam as it is dependent solely on the evolution of the phase difference between the beams which can be completely defined as a function of propagation distance by the OAM and radial number of the modes giving the difference in Gouy phase as in Eq(4.43). Since these properties are spatially independent in the transverse plane the difference in Gouy phase between the modes is also uniform and grows with increasing propagation distance until it asymptotes. As all the polarisation ellipses in the transverse plane experience the same change in orientation, the polarisation pattern as a whole remained the same. Diffraction of the beam had no effect on the rotation or the overlap between the beams and simply resulted in a global scaling of the spot size of the beam upon propagation.

However, in the nonlinear case, the Kerr effect results in self-focussing and cross-phase modulation. The amount of self-focussing depends on the individual mode and this in turn affects the cross-phase modulation between the modes of the FSL beam. Combined with the saturation in the mode we get a very complicated system.

The size of the modes upon nonlinear propagation depends on the balance between diffraction and the self focussing effect of the nonlinear medium. As the nonlinear response is intensity dependent, different OAM modes will experience different focussing and spatial confinement. For vector superpositions where $|\ell_R| \neq |\ell_L|$ the spatial overlap between the modes will change upon propagation since the focussing effect is not the same for each beam. Furthermore for nonlinear propagation the beams are coupled and do not propagate independently, the intensity distribution of one affects how the other propagates in a cross guiding effect due to cross phase modulation in the medium.

The effect of the cross phase modulation terms from Eq.(4.33) tends to maximise the spatial overlap of the intensity distribution of the two beams in the vector superposition such that after a sufficient propagation distance the two modes have the same spatial intensity distribution. A combination of the balancing between diffraction and self-focussing and the cross-guiding effect between the eigenmodes in the FSL beam results in the phase change of each of the beams becoming spatially dependent. This in turn means the evolution of the phase difference between each of the modes in the vector beam varies from point to point in the transverse plane and because the rotation of the polarisation at each point is directly dependent on this relative phase difference the rotation is no longer homogeneous for a nonlinear propagation. The change in orientation for each polarisation ellipse now depends on the spatial overlap and intensity distribution of the FSL beam and since the rotation at each point in the transverse plane varies the polarisation pattern as a whole now can change upon propagation.

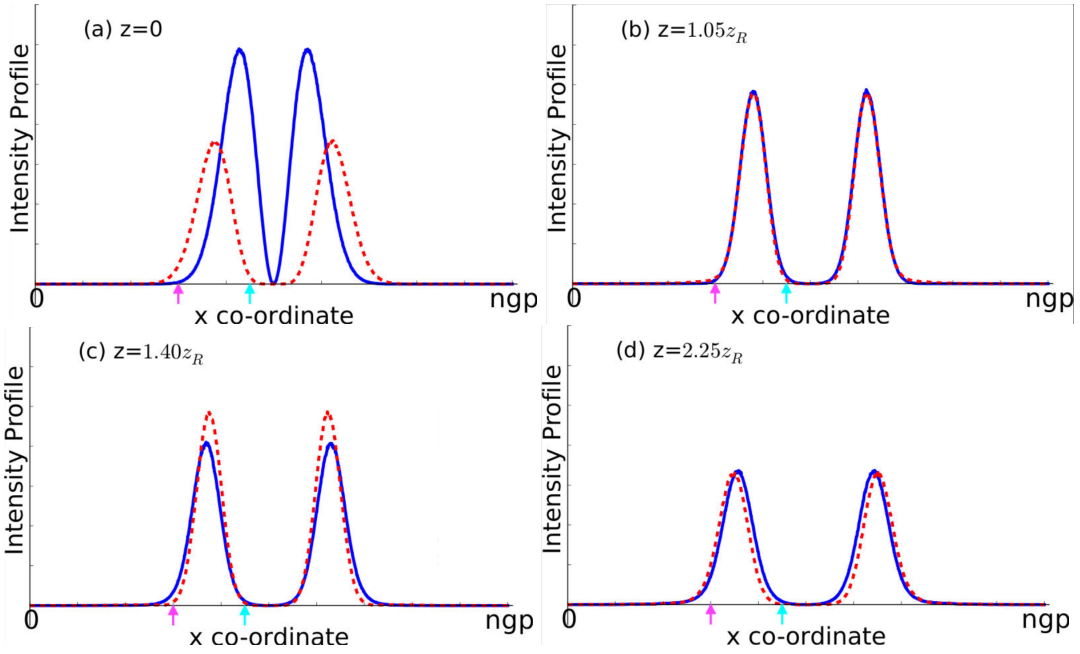

FIGURE 4.6: Transverse intensity profiles for an FSL beam composed of $\ell_R = 3$ (dashed red) and $\ell_L = -1$ (solid blue) at z=0 in (a) and after a nonlinear propagation ($n_2 = 8$) of z=1.05z_R in (b), 1.40z_R in (c) and 2.25z_R in (d). The cyan and magenta arrows represent chosen points in the transverse plane in which the rotation curves are shown in Figure.(4.7)

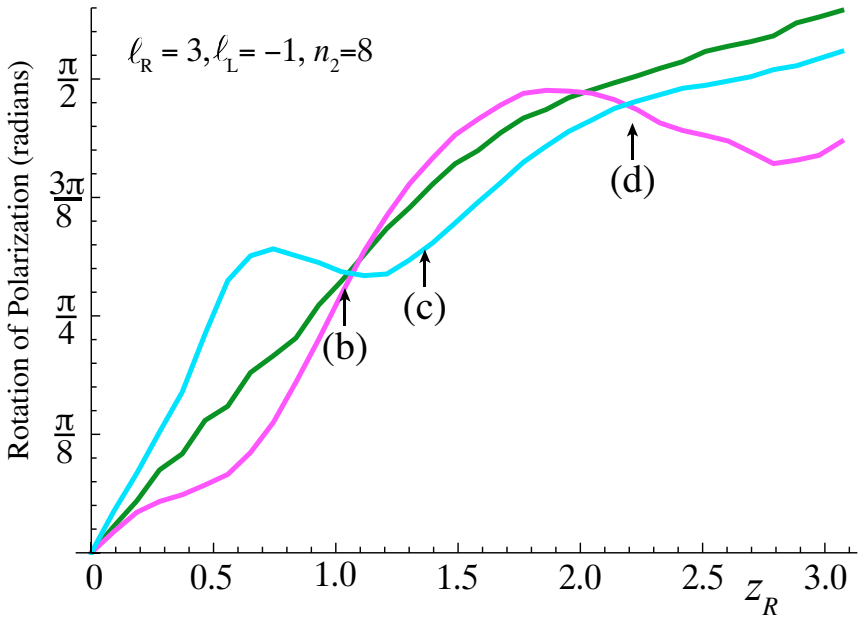

FIGURE 4.7: Rotation curves for the corresponding points chosen in Figure.(4.6) given by the cyan and magenta lines as well as the rotation curve when tracking the peak given by the green curve. The dashed lines represent the propagation distances of the transverse profiles in Figure.(4.6).

Figure.(4.6) shows a cut through the transverse intensity profiles and how the spatial overlap between the two modes in a vector superposition of $l_R = 3$ (red) and $l_L = -1$ (blue) evolves during propagation. We can see that the relative dimensions of of the modes fluctuate during propagation such that the spatial overlap and hence polarisation rotation across the transverse profile of the FSL beam changes. As the relative width of the modes fluctuate the polarisation rotation can change direction (see the cyan line in Figure(4.7)). The combination of self-focussing, diffraction and cross-phase modulation for a nonlinear propagation maximises the spatial overlap of the modes, at which point the rotation becomes uniform and asymptotes.

This is demonstrated in Figure(4.7) which shows the corresponding rotation of the polarisation ellipse for each of the points given by the coloured arrows in Figure(4.6). Depending on the change in relative phase difference and overlap between E_R and E_L, the rotation at each particular point in the plane can slow, stop or even change direction as can be seen by the cyan rotation curve. At the start of the propagation

(see Figure(4.6a)), points on the outer edge of the beam (magenta) see more right-circularly polarised light, while points closer to the centre (cyan) see more left circularly polarised light and thus their polarisations rotate in opposite directions. When the modes overlap exactly (see Figure(4.6b)) the modes experience the same nonlinear phase shift and so there is no net nonlinear rotation. If the beams remain *locked* like this then the polarisation rotation asymptotes. As the modes oscillate net left or right circularly polarised light can swap resulting in polarisation rotation changing direction (see Figure(4.6c)). Note that as the beam continues to propagate the effect of the nonlinearity is to try to maintain the spatial overlap of the two modes. Finally the *locked* beams then propagate with a constant small rotation depending on the final overlap of the beams see (see Figure(4.6d)). The green line in Figure(4.7) shows the behaviour of rotation when tracking the peak intensity (S_0) of the beam, which again has a different behaviour showing the non-uniform nature of the rotation of the polarisation across the transverse plane.

4.4.2 Evaluating Rotation for Nonlinear Propagation

These factors leave a number of choices as how to best represent the rotation of the polarisation for a given vector beam for a nonlinear propagation. Choosing a particular point (x,y co-ordinate) in the transverse plane as we did in the case of linear propagation is not really of use as the it is not representative of the behaviour across all the points in the beam. As shown in Figure.(4.7) the difference in behaviour of the rotation curves for different points can be severe hence we need a method to characterise the rotation of each FSL beam by a single curve. We note that a single curve gives a sense of the rotation of the FSL overall, though some applications could make use of the variation in rotation across the beams. A better choice of measurement would be to track the rotation of the polarisation ellipse at the peak intensity of the FSL beam as this lies between the two extremes at the edge of the intensity profile and hence gives an idea of the average between these two points. Tracking the rotation at the maximum intensity of the FSL beam has a characteristic less erratic behaviour in that it does not stop

and change direction as often as shown by the green curve in Figure.(4.7). However whenever there is a mode of $l = 0$, i.e. one of the beams in the vector superposition has a Gaussian profile rather than a doughnut, when the cross guiding of the cross phase modulation causes overlap of the beams the position of the peak intensity can change discontinuously from the centre of the Gaussian profile to the peak of the doughnut mode shape. This effect is shown in greater detail in a later section, but the main point is because the Gaussian beam changes its profile so rapidly when taking on the shape of higher order doughnut mode, the position of the peak intensity changes discontinuously and the jump in position of the peak causes the big jumps in the measurement of the polarisation rotation. Because of this tracking the peak intensity for measurement of the rotation is only effective for FSL modes where $|\ell_{R,L}| > 0$.

Another method, and the one chosen to evaluate the rotation of polarisation for the remainder of this chapter for nonlinear propagation involves averaging the rotation over many points on the transverse field. We select many points across the intensity profile of the FSL beam and calculate an average curve over the selected points. This has the same benefit as tracking the peak intensity in that a typical or average behaviour of the polarisation ellipse are characterised by a single curve for any given FSL beam but with the added benefit it is less sensitive to the shape and spatial overlap of the modes in the vector composition. Furthermore because the beams are radially symmetric we need only select one point in the transverse plane at each given radius i.e. average over all the points across a line spanning half the beam waist in the transverse plane as shown in Figure.(4.8). Averaging the rotation of the points over any of the dashed coloured dashed lines will yield the same results and characterise the average rotation for any FSL beam with no restrictions on the OAM values. The corresponding rotation curves for the coloured lines and the averaging method described are shown in Figure.(4.9) and it can be seen all curves are identical over any of the chosen lines because of the radial symmetry of the beam. For simplicity for the remainder of this chapter we will use the averaging method for measuring the polarisation rotation for nonlinear propagation using the points which have (x,y) with $x{=}y$ which corresponds to the red dashed line in Figure.(4.9).

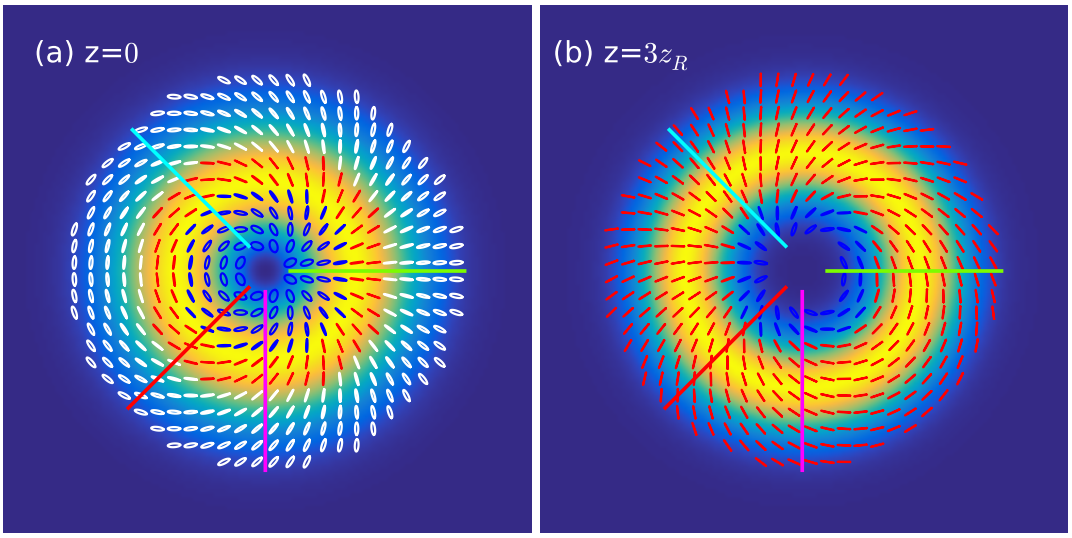

FIGURE 4.8: Polarisation distribution for a FSL superposition of $\ell_R = 2$ and $\ell_L = -1$ at z=0 and after nonlinear propagation ($n_2 = 8$) to a distance of $z = 3z_R$. The overlayed dashed coloured lines represent the points over which the rotation curves are averaged in Figure.(4.9).

4.4.3 Comparison between Linear and Nonlinear Propagation

To investigate the effect the nonlinearity has on the behaviour of the polarisation structure, Eq.(4.33) is numerically integrated. If the rescaling of the beam due to diffraction is neglected and the model is simplified, it can be seen that the first effect of the medium is an additional phase shift $\phi_{R,L}^{NL}$ to the orthogonal modes which is proportional to the nonlinear term. The rotation of the polarisation ellipses in the previous section was shown to be purely dependent on the phase difference between $\mathbf{E}_R$ and $\mathbf{E}_L$ such that for a nonlinear propagation we expect additional rotation due to the phase shift given by $\phi_{R,L}^{NL}$. We can write that the additional nonlinear rotation is proportional to

$$\Delta\psi_{NL}(z) \propto \left(\psi_L^{NL} - \psi_R^{NL}\right) \tag{4.46}$$

in addition to rotation caused by the difference in Gouy phase of the two modes. From this it can be concluded that when compared to the linear case, the magnitude of rotation of the polarisation is expected to be greater for propagation in a nonlinear

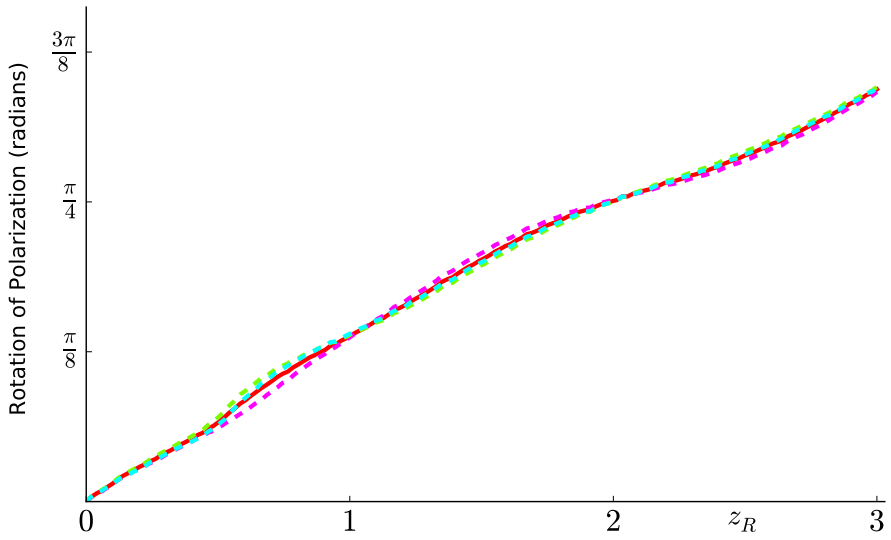

FIGURE 4.9: Corresponding averaged rotations curves. The colour of each curve corresponds to averaging the rotation over the points represented by the solid lines in Figure.(4.8) over a nonlinear propagation of 3 Rayleigh lengths.

medium. Figure.(4.10) gives the comparison between the linear and nonlinear cases over a propagation distance of 3 Rayleigh lengths, $z = 3z_R$, for the lowest order OAM modes that give each respective $|\Delta\ell_{R,L}|$ curve, i.e. $\ell_R = |\Delta\ell_{R,L}|$ and $\ell_L = 0$. The lowest order modes are again used to avoid numerical error from noise when the beams have diffracted significantly. It is clear from comparison between the curves that the rotation no longer asymptotes with propagation but instead increases almost linearly with propagation distance. This can be attributed to the phase difference between the two modes continuing to evolve from the inclusion of the nonlinear phase given by $\phi^{NL}_{R,L}$ well past the propagation distance where the Gouy phase $\eta(n)$ begins to asymptote. For a nonlinear propagation there will be a continual change in the phase difference between the modes due to the change in spatial overlap and cross-phase modulation such that the rotation will continue up until fragmentation of the beam hence it can be seen by comparing the linear and nonlinear propagation that the magnitude of rotation is much larger for the latter from a combination of these effects. An important note here is that cylindrical vector beams of $|\ell_R| = |\ell_L|$ still do not experience any rotation of the polarisation ellipses even in the nonlinear case. Because they have the same initial spatial profile they experience the same balance of self-focussing and diffraction such

that they propagate in a "locked" state where their spatial profile perfectly overlaps for the entirety of the propagation. This means that they have the same Gouy phase and experience same the nonlinear phase shift $\phi^{NL}_{R,L}$ so the phase difference between the modes is a constant with propagation with the result that there is no rotation of the polarisation.

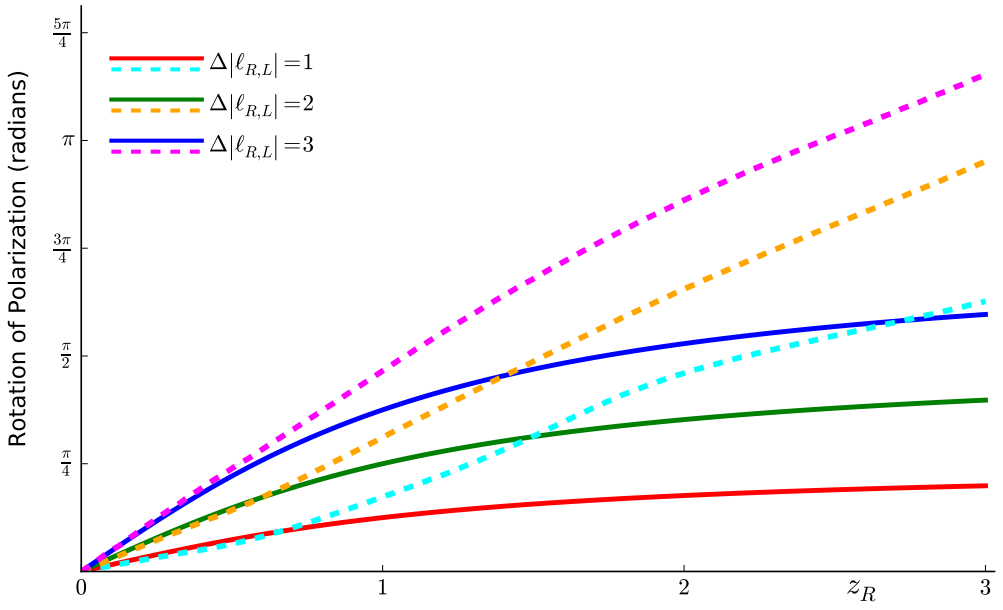

FIGURE 4.10: Measured rotation in polarisation during nonlinear propagation from beam waist to $z = 3z_R$, numerically integrating Eq.(4.33) for $\mu = 257.5$ and $\sigma = 19.8$ for vector beams composed of $\ell_R = \pm|\Delta\ell_{R,L}$ and $\ell_L = 0$, presented in the dashed lines. An analytical comparison for linear propagation using Eq.(4.44) is shown in the solid lines. $|\Delta\ell_{R,L} = 1$ (green, orange), 2 (red, cyan) and 3 (blue, magenta).

In the linear case the rotation depends purely on the difference in the magnitude of the OAM of the two eigenmodes such that any composition of OAM modes for any given $\Delta|\ell_{R,L}|$ no matter the OAM involved in the superposition the rotation curve is identical and homogeneous across the transverse plane. We have already shown that in the nonlinear medium the rotation is inhomogeneous across the beam due to the changing spatial overlap between the eigenmodes during propagation which was caused by the inclusion of the cross-phase modulation and balancing of diffraction and self-focussing. More importantly for the rotation, the nonlinear phase shift $\phi^{NL}_{R,L}$ also depends on the spatial overlap and intensity of the two modes in the FSL superposition which in turn

are directly related to the OAM values. This means that for a given $\Delta|\ell_{R,L}|$ the rotation of polarisation is not only inhomogeneous across the transverse plane but the particular values of the OAM in the superposition can change the magnitude and behaviour of the rotation. A FSL beam composed of $\ell_R = 2$ and $\ell_L = 0$ will no longer have the same rotation curve and behaviour as that composed of $\ell_R = 3$ and $\ell_L = -1$. Although they have the same difference in Gouy phase and the linear rotation is the same, the difference between the cross-phase modulation and self-focussing of each respective FSL superposition means that $\phi^{NL}_{R,L}$ and in turn the nonlinear rotation of polarisation is sensitive to the choice of OAM values.

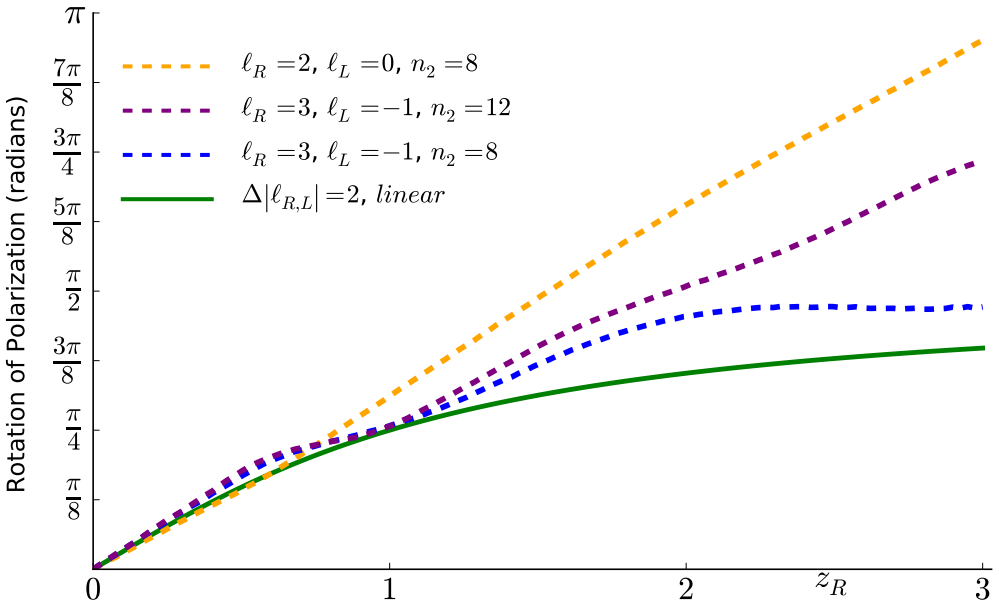

FIGURE 4.11: Polarisation rotation for a nonlinear propagation for $z = 3z_R$ for various FSL beams with a beam waist of 100μm and $\Delta|\ell_{R,L}| = 2$. The dashed blue line corresponds to $\ell_R = \pm 2$ and $\ell_L = 0$ for a $n_2 = 8$, the other dashed lines represent the rotation for $l_r = \pm 3$ and $\ell = \pm 1$ at a $n_2 = 8$ (purple) and $n_2 = 12$ (orange). The green solid line is the analytical result for a linear propagation for all the superpositions $\Delta|\ell_{R,L}| = 2$.

This phenomenon is demonstrated in Figure.(4.11) where the simulations for nonlinear propagation are repeated for a number of different mode superpositions with the same difference in magnitude of OAM where $\Delta|\ell_{R,L}| = 2$ but composed of different OAM superpositions and the respective rotation is measured. The orange curve is the same as in Figure.(4.10) for the lowest order $\ell_R = 2$ and $\ell_L = 0$ beam and by direct comparison

with the higher order $\ell_R = 3$ and $\ell_L = -1$ beam shown by the dashed blue line it can be seen there is a significant difference in the magnitude and behaviour of the rotation. Not only is the overall magnitude of rotation smaller for the higher order mode but the general shape of the curve with propagation distance is different. For the lowest order FSL beam the rotation increases almost linearly with propagation distance and this continues up until fragmentation of the beams. However for the higher order superposition there are regions during propagation where the rotation of the polarisation slows, stops and even changes direction and the rotation appears to asymptote with increasing propagation distance. Note that although here we have only shown the results for one higher order FSL beam very similar phenomena are observed when the value of OAM is increased. In fact the larger the value of OAM used in the FSL superposition the smaller the magnitude of rotation and the faster the rotation curve asymptotes. Another interesting behaviour that can be seen from Figure.(4.11) is that by increasing the value of the nonlinearity the magnitude of rotation increases and no longer asymptotes as seen by the dashed purple curve. As we increase the nonlinearity we recover the behaviour of the lowest order mode which can be attributed to a number of phenomena.

The most important phenomenon responsible for the difference in behaviour between the higher order modes ($l > 0$) and the FSL beams with a Gaussian beam ($l = 0$) is the spatial overlap between the eigenmodes in the superposition of the vector beam and how this spatial overlap evolves with propagation. Figure.(4.12) details the evolution of the overlap between the modes in the FSL superposition for the corresponding rotation curves in Figure.(4.11). For the lowest order mode represented by the dashed orange rotation curve composed of $\ell_R = 2$ and $\ell_L = 0$ it is apparent that the Gaussian mode takes on the shape of the higher order doughnut mode. However it quickly relaxes back to its original profile and because it had a fundamentally different shape than the doughnut modes it cannot become '*locked*' with the spatial profile of the higher order mode. The oscillation between taking on the doughnut profile and relaxing to a Gaussian distribution continues until fragmentation of the beam. The result of this behaviour is that the nonlinear phase from the cross-phase modulation between the

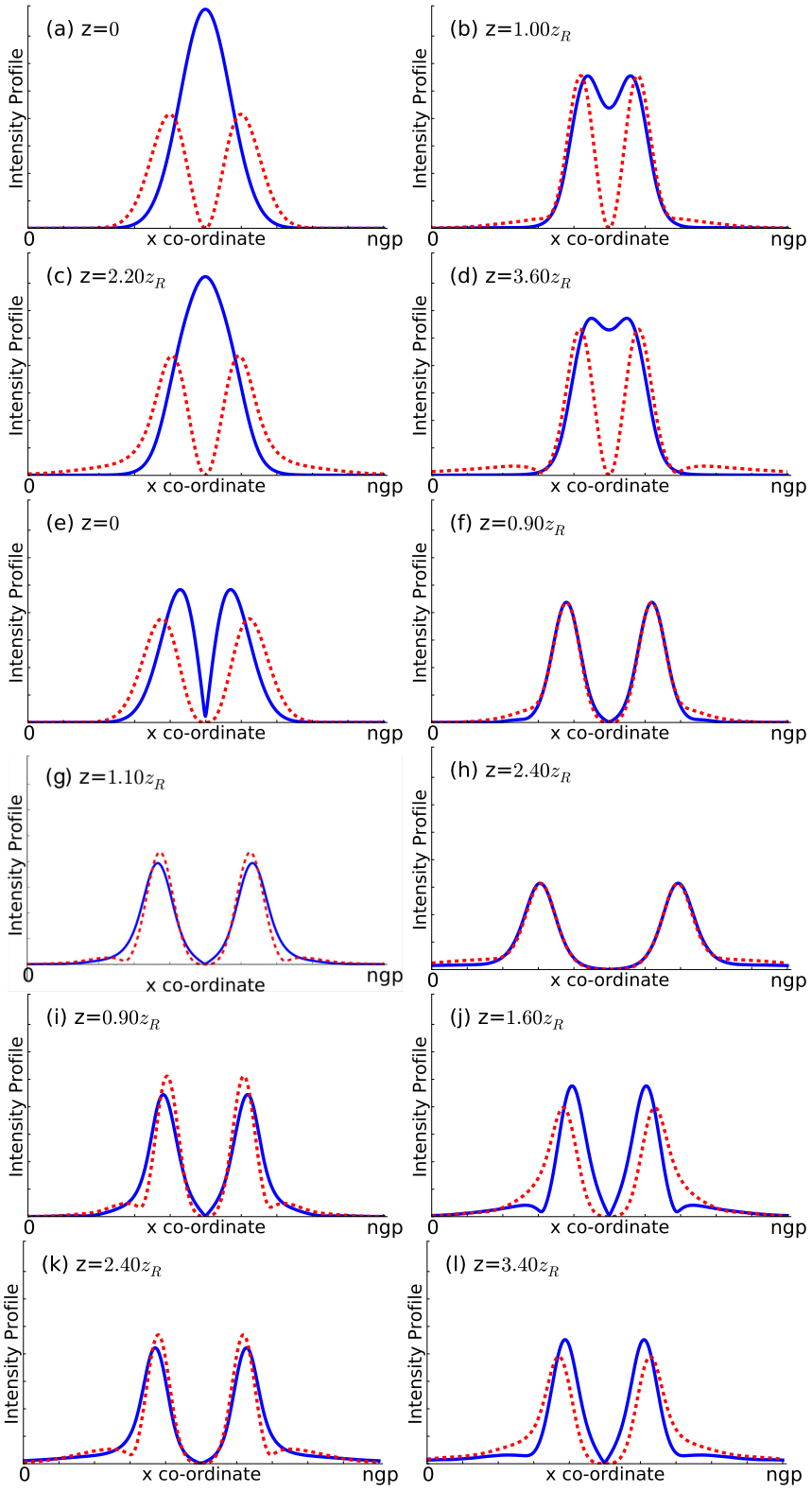

FIGURE 4.12: Cross-section of the spatial profile for selected FSL beams for a beam waist of $100\mu m$ composed of $\ell_R = 2$ and $\ell_L = 0$ with $n_2 = 8$ in (a)-(d), $\ell_R = 3$ and $\ell_L = -1$ with $n_2 = 8$ in (e)-(h) and $n_2 = 12$ in (i)-(l) at the stated propagation distances.

modes evolves continually which is why the rotation of the polarisation also continues in an almost linear fashion as shown by the dashed orange curve in Figure.(4.11).

However for the higher order FSL composed of $\ell_R = 3$ and $\ell_L = -1$ represented by the dashed blue line in figure Figure.(4.11) it can be seen that after nonlinear propagation of approximately $2.4z_R$ the two doughnut modes become '*locked*' in their spatial profile. Once locked the two beams share identical spatial profiles and propagate as such until fragmentation of the beam. The cross-phase modulation no longer causes any further change in the phase difference between the two modes and the nonlinear phase shift in Eq.(4.46) asymptotes. In terms of the rotation of the polarisation which is directly dependent on this phase difference it is also expected to asymptote in good agreement with the rotation curve. As the nonlinearity is increased we can see from images (i) to (l) in Figure.(4.12) that the same FSL superposition can now propagate for a much larger distance without the doughnut modes becoming locked in spatial profile. This results in the nonlinear phase and rotation of the polarisation persisting over larger propagation distances and there the asymptotic behaviour of the rotation disappears as shown by the purple dashed line in Figure.(4.11). As the nonlinearity is increased we start to recover the linear behaviour of the lowest order $\ell_R = 2$ and $\ell_L = 0$ beam.

The main difference in behaviour between the behaviour when increasing the nonlinearity is the change in balance between diffraction and self-focussing. As higher order LG modes are used in the FSL vector superposition the lower intensity of the modes cause less self-focussing and the beam tends to diffract more. This diffraction causes the spatial profile of each mode to spread out and tend towards a locked state as previously described. Thus for increasing OAM within the FSL superpositions, the rotation of the polarisation asymptotes more quickly as the beams reach a locked state due to increased diffraction. By increasing the nonlinearity the self-focussing of the Kerr nonlinearity spatially confines the higher order mode and by doing such the beams stay focused close to the original waist size. For larger and larger OAM values the nonlinearity must be increased to spatially confine the FSL beam and recover the same rotation behaviour.

The width of the beam and balance of diffraction and self-focussing is shown in Figure.(4.13) for the $\ell_R = 3$ and $\ell_L = -1$ for the two nonlinearities of the corresponding rotation curves in Figure.(4.11) and spatial overlap evolutions in Figure.(4.12).

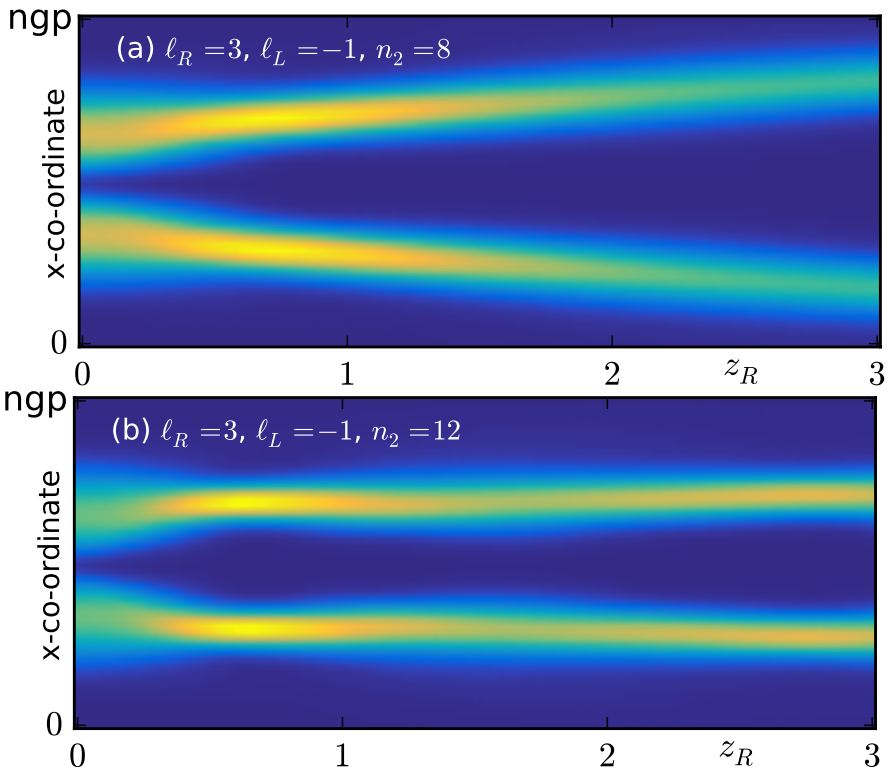

FIGURE 4.13: Cross-section of the spatial intensity during propagation for the FSL beam composed of $\ell_R = \pm 2$ and $\ell_L = 0$ at $n_2 = 8$ in (a). The equivalent for $n_2 = 12$ is shown in (b).
curv

4.4.4 Control of Polarisation Behaviour

In addition to understanding the mechanisms affecting the behaviour of the FSL beams during propagation, it is also important for various applications to be able understand how to control it through selection of various physical parameters. For a linear propagation there is a limitation as to the choices available to control the state of polarisation. The rotation is solely dependent on the difference in magnitude of the OAM and radial number of the eigenmodes in the FSL beam and governed through Eq.(4.43). The beam size can be altered as to control the Rayleigh range and hence the physical distance at

which the Gouy phase asymptotes, however for a given $|\Delta\ell_{R,L}|$ the shape of the curve for the rotation of the polarisation is fixed.

For a nonlinear propagation however the phase difference between the modes depends on the spatial overlap and intensity of the modes in the FSL composition which is inhomogeneous across the transverse plane. This in turn means all physical parameters affecting the self-focussing, nonlinear response, saturation and cross-phase modulation of the two modes will affect both the spatial confinement and overlap of the beams which in turn affects the rotation and behaviour of the polarisation. Therefore in the case of nonlinear propagation of a vector beam, there is a rich variety of parameters that can control the state of polarisation.

As we have shown previously, in both the linear and nonlinear case the choice of eigenmodes and their difference in OAM which determines $|\Delta\ell_{R,L}|$ has the largest effect on the behaviour of the polarisation rotation.

Figure.(4.14) gives one example that shows how the behaviour of the polarisation rotation changes with the power of the input beam. The power in the previous examples was chosen at 7.5mW (blue curve) and is the same curve as the orange dashed curve in Figure.(4.10). It is apparent that an increase in input power results in an increase in the nonlinear response leading to an larger magnitude in rotation of the polarisation. The increase in power also leads to an increase of the saturation parameter such that this effect asymptotes as the power becomes larger. Controlling the input power allows some limited control over the shape of the behaviour of the polarisation structure.

Additionally, changing the beam waist of the FSL beam controls the Rayleigh range - the distance over which characteristic behaviour of the polarisation state occurs. In image (a) of Figure.(4.15) the rotation for a nonlinear propagation is shown over $z = 3z_R$ for vector modes with beam waists of 100μm and for two examples - $\ell_r = 1, 2$ and $\ell_l = 0$ - in the dark blue and cyan curves respectively. The physical parameters for these curves are with $P_0 = 7.5mW$ and $n_2 = 8 \times 10^{-6} Wcm^{-2}$ such that the nonlinear parameter, $\mu = 257.5$, and saturation parameter, $\sigma = 19.8$. The results are repeated

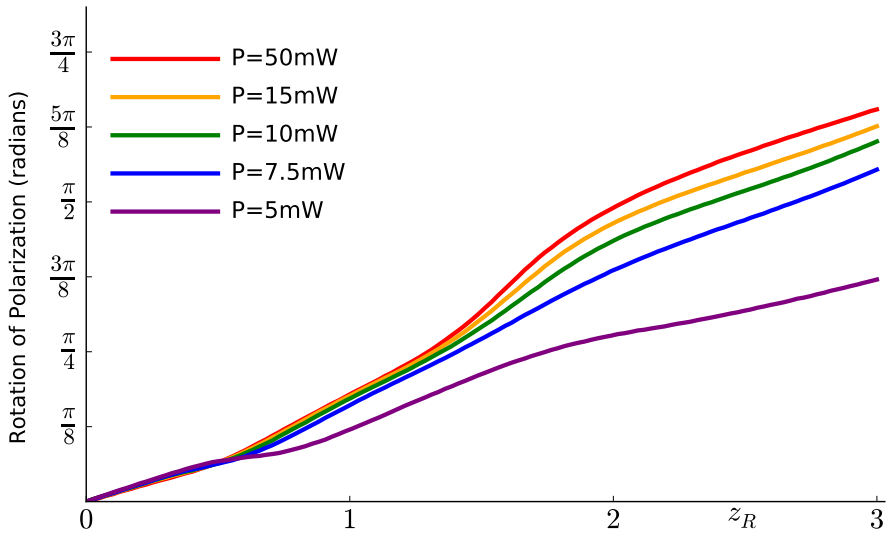

FIGURE 4.14: Polarisation rotation of $\ell_R = 1$ and $\ell_L = 0$ beam during nonlinear propagation from beam waist at $z = 0$ to $z = 3z_R$ for FSL beams with input power of 5mW (purple), 7.5mW (blue), 10.0mW (green), 15.0mW (orange) and 50mW (red).

for a beam waist of 200μm and shown in the dashed green and magenta curves for rescaled parameters $P_0 = 29.8m$W and $n_2 = 2 \times 10^{-6} Wcm^{-2}$ such that the nonlinear and saturation parameters are unchanged. Comparison between the beam waists shown that with control over the input power and nonlinearity of the medium, the magnitude of rotation for both cases can be made identical when compared over a given number of Rayleigh lengths in propagation. Plotting the same results as a function of physical distance rather than number of Rayleigh ranges, then by doubling the beam waist (increasing z_R by a factor 4), the magnitude of the larger beam is decreased by a factor of 4 for a given propagation distance. It is not possible to control the behaviour of the polarisation such that different beam widths have the same rotation over a given physical distance since it would require changing the ratios of n_2, P_0 and I_{sat}, such that the nonlinear and saturation parameters are altered which in turn changes the shape of the rotation curve.

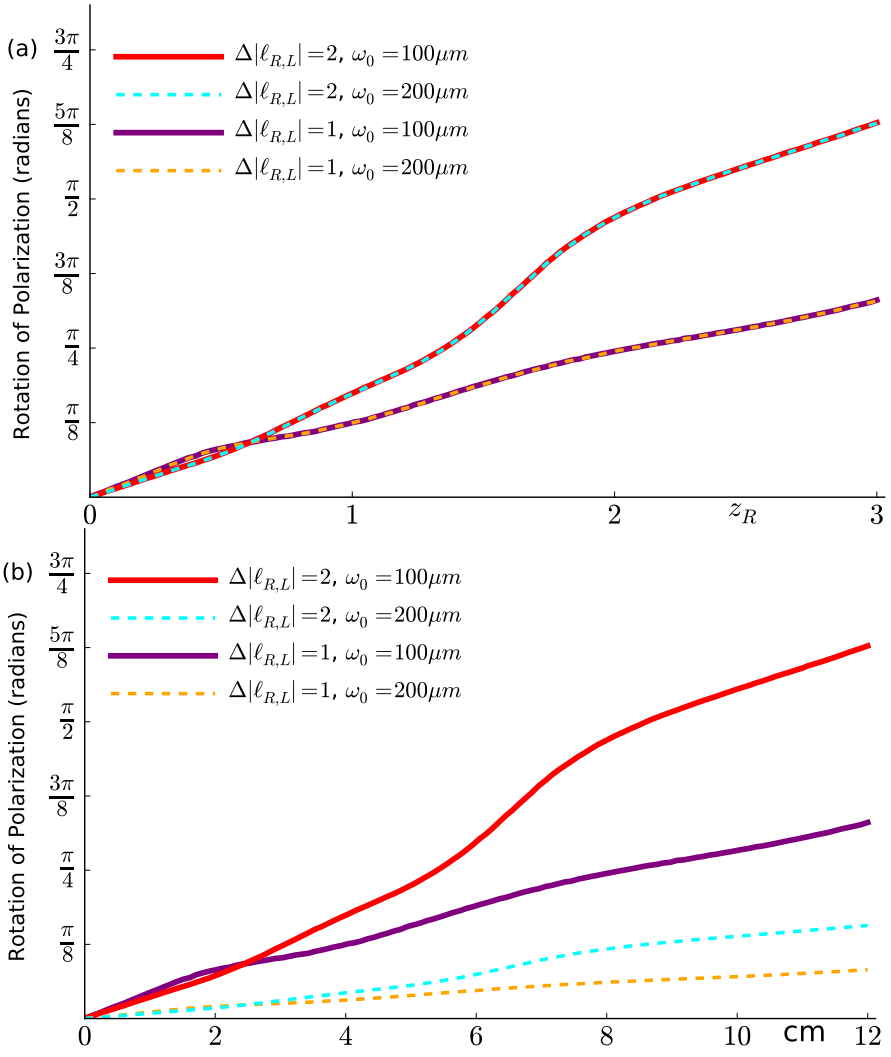

FIGURE 4.15: Polarisation rotation during nonlinear propagation for FSL beams with $\Delta|\ell_{R,L}| = 1, 2$ and waists of $100\mu m$ (dark blue, cyan) and $200\mu m$ (green, magenta). In both cases $\mu = 257.5$ and $\sigma = 19.8$ for (a) rotation against number of Rayleigh lengths and (b) rotation versus distance in cm.

4.4.5 Biased Vector Beams

The final method for controlling the behaviour of the polarisation structure is controlling the bias between the composition in the vector beam, i.e. changing γ in Eq.(2.38), such that the two modes in the superposition no longer have the same amplitude. For all results presented previously, γ was chosen to be $\pi/4$ such that the vector beams were of equal amplitude. In the linear case is was seen that the amplitude of the modes played

no part in the rotation of the polarisation hence the bias was unimportant in terms of polarisation orientation (it does however matter for the ellipticity of the polarisation even in the linear case). For a nonlinear propagation on the other hand, changing the bias between the two modes changes the spatial overlap between eigenmodes which has been shown to be central to the nonlinear polarisation rotation behaviour.

Cylindrical vector beams were shown in the linear section to experience no rotation or change in their polarisation distribution upon propagation, since for CV beams $|\Delta\ell_{R,L}| = 0$. Again in the nonlinear section, due to the eigenmodes having the same magnitude of OAM and hence the same spatial intensity profile both modes experienced the same Gouy phase and nonlinear phase shift such that the polarisation again remained unchanged upon propagation. However if the spatial intensity profile of the beams is changed by altering the bias, γ, *and* the beam propagates in a nonlinear medium, the nonlinear phase shift for each beam will no longer be equal and there should be polarisation rotation. Such behaviour is shown in Figure.(4.16) which shows that a rotation in the polarisation is observed for a biased CVB during nonlinear propagation. In addition it can be seen that the larger the difference in relative amplitude the larger the rotation that is observed. A further thing to note is that the rotation rate for a biased CVB is constant with propagation distance up until the point fragmentation of the beam occurs as shown by the straight rotation lines in Figure.(4.16). As the bias between the modes is further increased the contribution of one of the modes becomes negligible and approaches the scalar case and we recover the behaviour demonstrated in [11] in which a scalar beam fragments at a much shorter propagation distance compared with the FSL counterpart. Whether the larger amplitude is on the right or left circularly polarised modes determines the direction of rotation.

Another phenomenon observed by increasing the bias is that the increased rotation from increasing the bias asymptotes as the scalar case is approached. This is shown in Figure.(4.17) where the rotation after a propagation distance of $z = 3z_R$ is measured for a variety of different ratios of amplitudes as well as comparing the effect of increasing the magnitude of OAM in the CVB. We can see that for higher-order CVBs the magnitude

of rotation is larger, however due to the larger diffraction effect upon propagation we require a larger nonlinearity, n_2 in order to spatially confine the beam.

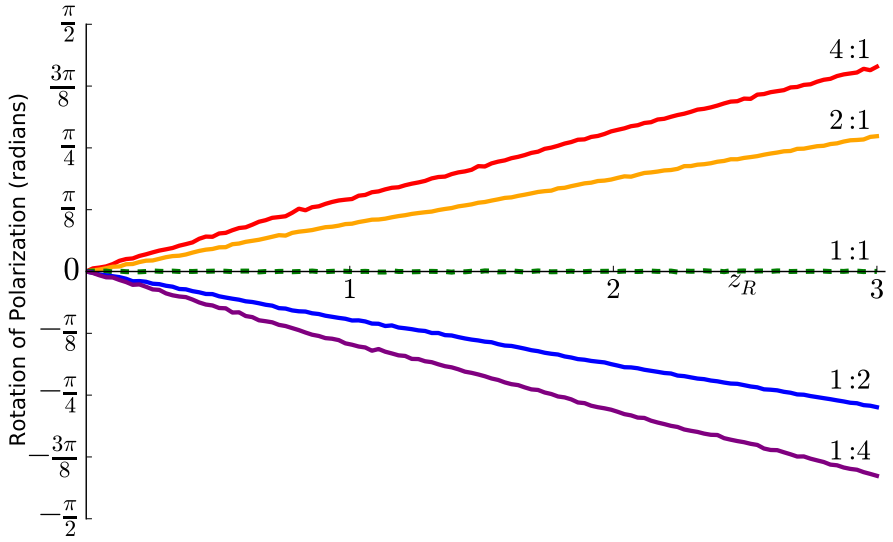

FIGURE 4.16: Nonlinear polarisation rotation for a propagation of a cylindrical vector beam with $|\ell_{R,L}| = 1|$ over $3z_R$. The parameter γ in Eq.(2.38) is chosen such that the ratio $|E_R| : |E_L|$ is 4:1 (red), 2:1 (blue), 1:1 (green), 1:2 (cyan) and 1:4 (magenta). The beam waist for each is $w_0 = 100\mu m$ and at low nonlinearity $n_2 = 8$.

An interesting result of the observed rotation in CV beams is the conversion of polarisation structure between radial and azimuthal through the intermediate spiral polarisation. This arises as the rotational symmetry of CV beams is infinite (i.e. the polarisation distribution is cylindrically symmetric) hence the polarisation structure does not rotate as a whole (as in Figure.(4.3)&(4.5)), but completely changes its structure as each point rotates. The transverse polarisation distribution for an amplitude ratio of $|E_R| : |E_L| = 4 : 1$ for a CV beam of $\ell_r = 1$ and $\ell_l = -1$ is shown in Figure(4.18) for (a) radial polarisation at $z = 0$, (b) spiral polarisation at $z = 1.3z_R$ and (c) azimuthal polarisation at $z = 2.5z_R$.

The polarisation distribution in the transverse plane during a nonlinear propagation for a biased CV beam of $\ell_r = 1$ and $\ell_l = -1$ with a bias of $|E_R| : |E_L| = 4 : 1$ for selected propagation distances. It is seen that at beam waist $z = 0$ the polarisation is radial, at $z = 1.3z_R$ the polarisation is spiral and finally at $z = 2.5$ the rotation is now azimuthal.

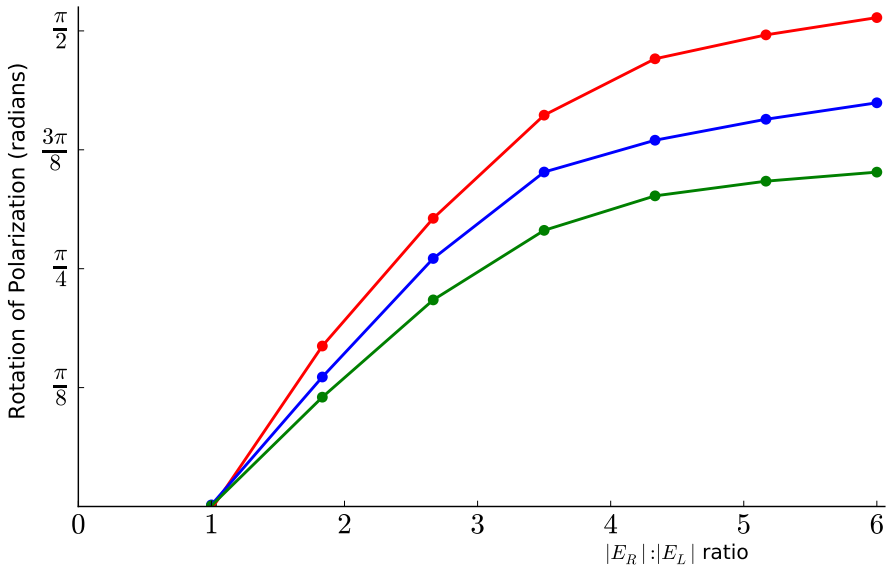

FIGURE 4.17: Nonlinear polarisation rotation at $3z_R$ as a function of biased CV beams with $|\ell_{R,L}|$=1,2 and 3 (red,blue and green respectively). The beam waist for each is $w_0 = 100\mu m$ and at low nonlinearity $n_2 = 8$.

Hence by selection of bias and beam width the polarisation can be controlled without the use of polarisation optics.

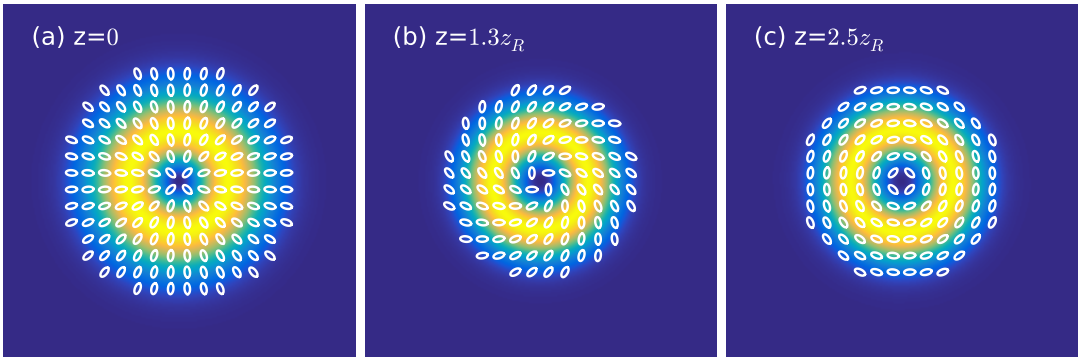

FIGURE 4.18: Radially elliptically polarised vector beam with $|\ell_{R,L}| = 1$ and $|E_R| : |E_L| = 4 : 1$. Left to right: At the beam waist $z = 0$, after nonlinear propagation over $z = 1.3z_R$, $z = 2.5z_R$. There is little change to the spatial profile of the beam during propagation but the polarisation structure as a whole changes from radial though spiral to azimuthal. The beam waist for each is $w_0 = 100\mu m$ and at low nonlinearity $n_2 = 8$.

4.5 Conclusions

Knowing how the spatial polarisation distribution of a beam is affected by propagation is of importance in many applications that depend on the state of polarisation. We have analytically calculated the polarisation rotation at each point of the transverse plane for fully-structured light (FSL) beams during linear propagation and shown that the observed rotation is due entirely to the difference in Gouy phase between the two eigenmodes comprising the FSL beams. This allows the exact polarisation state at a particular propagation distance to be controlled simply by choosing the eigenmodes of the FSL beam and the beam size. There was very good agreement between the analytical results and the numerical simulation although due to diffraction and noise the rotation can only be tracked over a finite propagation distance.

Moreover, we have shown that polarisation rotation is also affected by propagation through a self-focussing (Kerr) nonlinear medium and that this can be controlled by changing the eigenmodes of the superposition, and physical parameters such as the beam size, the amount of Kerr nonlinearity and the input power. Because of the cross-guiding effect from the cross-phase modulation during a nonlinear propagation the changing spatial overlap between the modes during propagation means that the rotation of the polarisation can be observed over a longer propagation distance. In addition, the ability to control both the intensity and polarisation of FSL beams may provide a useful method for applications in micro machining and microscopy [88, 89]. Finally, we have shown that by biasing cylindrical vector (CV) beams to have elliptical polarisation, we can vary the polarisation state from radial through spiral to azimuthal using nonlinear propagation.

Chapter 5

Spatially Rotating Solutions and Structured Light in a Vectorial Kerr Cavity

5.1 Introduction

In the previous section we detailed the behaviour of the polarisation structure during the propagation of fully structured light both in the linear and nonlinear cases. In this chapter we introduce a cavity around the nonlinear medium, just as in Chapter 3, and investigate the effect the cavity has on the behaviour of the light and its interaction with the medium. In particular, we focus on the pattern formation region where a Turing pattern presents itself on the OAM ring. We show that the generation of solitons and one dimensional patterns on the ring results in a rotating structure of peaks due to the phase gradient of the $\exp(i\ell\phi)$ dependence of OAM pumps. In the scalar case we derive an analytical expression for the rotation speed of the Turing structure and show good numerical agreement in the two dimensional case. In the full vector case, by choice of bias (relative intensity between modes in a FSL beam), OAM and beam waist we show the position and angular rotation rate of the peaks from the Turing instability can

be controlled. Such techniques are important in optical microscopy [90] and particle manipulation [91, 92]

We begin in section Section 5.3, considering the Lugiato-Lefever model in one dimension where analytical considerations are achievable. This corresponds to unwrapping the OAM ring into one dimension and adding periodic boundary conditions. We consider the growth of a perturbation to the stationary state of the Lugiato-Lefever in one dimension and observe the formation of Turing patterns above the intensity threshold. We derive an analytical description for the rate of rotation for Turing patterns on a scalar pump with OAM and show good agreement with numerical solutions.

In Section 5.4 we consider the full two dimensional Lugiato-Lefever case in which we analyse the rotation of Turing instabilities for optical vortex pump shapes both for a Laguerre-Gauss pump and a scalar tophat pump with an added phase of the form $\exp(i\ell\phi)$. In the Laguerre-Gauss case we compare the behaviour of the Turing pattern with the analytical one dimensional case and show good agreement between the rotation rates. In the tophat case we observe the formation of multiple rings of Turing instabilities. These individual rings are independent and rotate at different rates according to the analytical relationship we derived. Due to diffraction rings even when the pump is below the Turing instability threshold, the peak of the ring can actually form the Turing pattern. In addition, by controlling the steepness and width of the tophat pump we can control whether the diffraction ring causes pattern formation in the centre, at the edge or in the middle of the tophat pump.

Finally, in Section 5.5 we consider the full vector case in which the pump is of the form of the fully structured light as described in the previous chapter. For a balanced vector beam (same intensity in each mode) with equal and opposite magnitudes of OAM we show that the rotational effects of each of the modes cancel and we observe a stationary Turing pattern on the FSL beam. By controlling the relative bias between the intensities of the two modes we show that we can control the rate of rotation to obtain any rotation rate between the scalar cases and the balanced vector stationary state. Finally, we detail how decoupled rings can be generated in which each of the

Turing patterns can rotate independently at any rate in either direction by control of the OAM and beam size.

5.2 Nonlinear Model

We consider a similar cavity set up to Chapter 3 but now with a third order ($\chi^{(3)}$) medium and do not consider any wave mixing phenomena during propagation in the medium. A schematic diagram of a vectorial Kerr ring cavity is shown in Figure(5.1), where we consider the pump to be of the form of a Laguerre-Gauss beam as in Eq(2.35) or a fully structured light mode as in Eq(2.38).

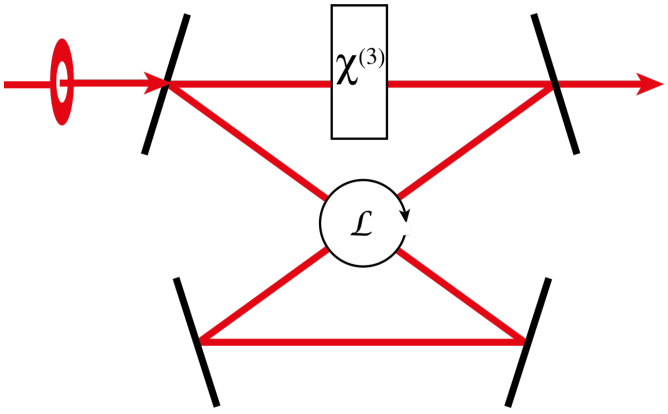

FIGURE 5.1: Schematic diagram of a vectorial Kerr ring cavity of length $\mathcal{L}$ with one partially reflecting mirror. The ring at the input represents a Laguerre-Gauss or fully structured light pump.

We have already derived the form of the nonlinear polarisation response of the medium in Eq(4.31) from Section 4.2 in Chapter 4 which is given by

$$P_{L,R}^{NL} = 3\varepsilon_0\left[|E_{L,R}|^2 + 2|E_{R,L}|^2\right]E_{L,R}. \tag{5.1}$$

In this case we don't, at the moment, consider saturation of the nonlinearity. Substituting this into the paraxial wave equation in Eq(5.2) we obtain a description of the propagation of a FSL beam through the nonlinear $\chi^{(3)}$ medium as the coupled equations

$$\frac{\partial E_{L,R}}{\partial z} + \frac{n_0}{c}\frac{\partial E_{L,R}}{\partial t} = \frac{i}{2k}\nabla_\perp^2 E_{L,R} + \frac{3i\omega}{2c}\left[|E_{L,R}|^2 + 2|E_{R,L}|^2\right]E_{L,R}. \tag{5.2}$$

By using the same cavity considerations as in Chapter 3 and making a similar mean field derivation as in [9] we obtain [93]

$$\partial_t E_{L,R} = -(1 + i\theta_{L,R})E_{L,R} + i\nabla^2 E_{L,R} + P_{L,R} + \frac{2i}{3}\left(|E_{L,R}|^2 + 2|E_{R,L}|^2\right)E_{L,R} \tag{5.3}$$

where $E_{L,R}$ are the left and right circularly polarised intra-cavity modes, $P_{L,R}$ is the amplitude of the left and right hand circularly polarised pump modes that make up the FSL beam, $\theta_{L,R}$ is the detuning between each of the relevant pump modes and the nearest cavity resonant frequency and again ∇^2 is the transverse Laplacian operator.

5.3 Scalar 1D case

In analysing the scalar (one mode) one dimensional case we begin from the well-known Lugiato-Lefever equation (LLE) in two transverse dimensions [94]:

$$\partial_t E = P - (1 + i\theta)E + i\beta|E|^2 E + i\nabla^2 E \tag{5.4}$$

where E is the intracavity field, P is the amplitude of the input pump, θ is the detuning between the input pump and the closest cavity resonance, β is proportional to the Kerr coefficient of the nonlinear material, and the term with the transverse Laplacian ∇^2 describes diffraction and can be written in either Cartesian or polar coordinates. In the following we will consider $\beta = 2/3$ because of its connection to the two orthogonal polarisation case as detailed in the previous chapter, but all considerations apply to generic values of β since its change corresponds to a renormalisation of E and P respectively. The time scale has been normalised by τ_p, the mean lifetime of photons in

the cavity given by $2L/cT$ for a unidirectional ring cavity and by $4L/cT$ for a Fabry-Perot cavity, with L being the cavity length, T the (intensity) transmission coefficient of the cavity mirrors and c the speed of light in vacuum. The transverse spatial scale (x or y) has been normalised by

$$a = \left(\frac{c\tau_p}{2K}\right)^{1/2} = \left(\frac{c\lambda\tau_p}{4\pi}\right)^{1/2} = \left(\frac{L}{KT}\right)^{1/2} \tag{5.5}$$

where K and λ are the wave vector and wavelength of the input light, respectively. By comparison with the full FSL model within the cavity in Eq(5.3) we can see that when one of the left or right circularly polarised modes amplitudes is zero it simplifies to the Lugiato-Lefever model, for the case the $\beta = 2/3$.

In order to derive some analytical results, we consider ring of fixed radius R normalised via Eq(5.5). By considering the transverse Laplacian in polar coordinates (R, ϕ), Eq(5.4) can be written as an LLE in one angular transverse dimension:

$$\partial_t E = P - (1 + i\theta)E + i\beta|E|^2 E + \frac{i}{R^2}\frac{\partial^2 E}{\partial \phi^2} \, . \tag{5.6}$$

The focus of this work is the effect of pumping the ring with light carrying orbital angular momentum (OAM) and superpositions of such modes. We therefore, in the scalar one dimensional case, consider pumps of the form:

$$P = P_\ell e^{i\ell\phi} \tag{5.7}$$

where P_ℓ is a complex amplitude independent of the azimuthal co-ordinate ϕ, and ℓ is an integer corresponding to the topological charge of the optical vortex. Writing the LLE in one angular transverse dimension corresponds to unwrapping the 2D transverse OAM ring into one dimension and adding periodic boundaries. In this case we study solutions of the form:

$$E(\phi, t) = F(\phi, t)e^{i\ell\phi} \tag{5.8}$$

that satisfy the equation:

$$\begin{aligned}\frac{\partial F}{\partial t} &= P_\ell - \left[1 + i\left(\theta + \frac{\ell^2}{R^2}\right)\right] F + i\beta|F|^2 F \\ &- \frac{2\ell}{R^2}\frac{\partial F}{\partial \phi} + \frac{i}{R^2}\frac{\partial^2 F}{\partial \phi^2}\,.\end{aligned} \tag{5.9}$$

One effect of the OAM-dependent solution Eq(5.8) is that the detuning is modified by an amount ℓ^2/R^2. We note that this phase shift is independent of the sign of OAM (i.e. left- or right-hand phase circulation) and the overall effect is to increase the cavity off-tuning for positive θ and to (partially) compensate the detuning in the case of negative θ. Moreover, this OAM-dependent detuning increases when the radius of the ring decreases.

5.3.1 Homogeneous Stationary States

For any value of ℓ, the homogeneous stationary solutions F_s are obtained from:

$$P_\ell = F_s\left[1 + i\left(\theta + \frac{\ell^2}{R^2} - \beta I_s\right)\right] \tag{5.10}$$

where I_s is the intensity of the stationary solution $I_s = |F_s|^2 = |E_s|^2$ given by the implicit form

$$|P_\ell|^2 = I_s\left[1 + \left(\theta + \frac{\ell^2}{R^2} - \beta I_s\right)^2\right]\,. \tag{5.11}$$

We highlight the radial dependent detuning term that comes from the OAM associated with the helical phase of the stationary solution Eq(5.8). Once the stationary intensity I_s is selected, the amplitude of the input field is obtained from Eq(5.11) while the phase of either the stationary field or the pump is obtained through Eq(5.10). Note that for $\ell \neq 0$, homogeneous stationary states of Eq(5.9) correspond to stationary states for the field E that are not homogeneous in the phase ϕ.

5.3.2 Turing instabilities on the ring for $\ell = 0$

For $\ell = 0$, $F = E$ and Eq(5.9) is equivalent to Eq(5.6). Both Eq(5.4) and Eq(5.6) are well known to display a Turing instability of the homogeneous stationary state. For clarity reasons, in the perturbation of the stationary state of Eq(5.6) we use k_ϕ for angular wave vectors associated with ϕ of the form $\exp(ik_\phi\phi)$ and $k = k_\phi/R$ for the spatial wave vector associated with R_ϕ of the form $\exp(ikR_\phi)$. Above the Turing instability, both Eq(5.4) and Eq(5.6) with $\ell = 0$ experience the linear growth of a perturbation with wave vector k given by [94, 95] :

$$\lambda(k) = -1 \pm \sqrt{4\Delta\beta I_s - 3\beta^2 I_s^2 - \Delta^2}\,. \tag{5.12}$$

where $\Delta = \theta + k^2$. It is clear from Eq(5.12) that if the square root is imaginary, there are no instabilities since both eigenvalues have negative real part. For a real eigenvalue to be positive, the quantity in the square root has to be larger than one. The instability boundary where the square root in Eq(5.12) is exactly equal to one, provides a relation between the detuning Δ (which contains the wave vector k) and the stationary intensity I_s:

$$\Delta = 2\beta I_s \pm \sqrt{\beta^2 I_s^2 - 1}\,. \tag{5.13}$$

This shows that there is an instability threshold in the stationary intensity given by $I_s^c = 1/\beta$. For a given $I_s > I_s^c = 1/\beta$ the most unstable wave vector is obtained by finding the maximum of the square root in Eq(5.12) when changing Δ:

$$k_c = \frac{k_{\phi,c}}{R} = \sqrt{2\beta I_s - \theta}\,. \tag{5.14}$$

Above threshold, N peaks appear along the ring separated by a distance given by, or close to, the wavelength of the Turing structure $\Lambda_c = 2\pi/k_c$. Note that $k_c R = k_{\phi,c} = N$ and exactly N peaks fit inside a ring of radius R to satisfy the periodic boundary conditions.

5.3.3 Rotating solutions for $m \neq 0$

In order to investigate the effect of the OAM we now focus on the case where $\ell \neq 0$. We start by rearranging Eq(5.9) such that the first order derivatives are on the left hand side:

$$\frac{\partial F}{\partial t} + \frac{2\ell}{R^2}\frac{\partial F}{\partial \phi} = P_\ell - \left[1 + i\left(\theta + \frac{\ell^2}{R^2}\right)\right] F + i\beta|F|^2 F + \frac{i}{R^2}\frac{\partial^2 F}{\partial \phi^2} \,. \tag{5.15}$$

It is important to note that this is the generalisation of the analysis of a tilted wave front [96] to polar coordinates on a ring.

We consider solutions to Eq(5.15) of the form $F(q)$ that move around the ring at a constant angular velocity ω and that depend on the variables ϕ and t through

$$q = \phi - \omega\, t \,. \tag{5.16}$$

In this case we can write the left hand side of Eq(5.15) as

$$\frac{\partial F}{\partial t} + \frac{2\ell}{R^2}\frac{\partial F}{\partial \phi} = \frac{\partial F(q)}{\partial q}\left(-\omega + \frac{2\ell}{R^2}\right) \,. \tag{5.17}$$

Clearly this equals zero when

$$\omega = \frac{2\ell}{R^2} \,, \tag{5.18}$$

and thus there exist rotating solutions $F(q)$ with angular velocity $\omega = 2\ell/R^2$ that can be determined via

$$P_\ell = \left[1 + i\left(\theta + \frac{\ell^2}{R^2}\right)\right] F - i\beta|F|^2 F - \frac{i}{R^2}\frac{\partial^2 F}{\partial \phi^2} \,. \tag{5.19}$$

Apart from a renormalisation of the detuning, Eq(5.19) is equivalent to the stationary solutions of Eq(5.9) and Eq(5.6) for $\ell = 0$. This means that all the results of the $\ell = 0$ case can be applied to the $\ell \neq 0$ case starting from the trivial homogeneous stationary state that we have already seen in Eq(5.10) and Eq(5.11). Since the Turing patterns for $\ell = 0$ are stationary states of Eq(5.9) and Eq(5.6), there exist Turing patterns that

are rotating solutions of Eq(5.15) for $\ell \neq 0$ satisfying Eq(5.12) and Eq(5.13) upon the redefinition of

$$\Delta = \theta + \frac{\ell^2}{R^2} + k^2 \tag{5.20}$$

while the critical wave vector is now:

$$k_c = \frac{k_{\phi,c}}{R} = \sqrt{2\beta I_s - \theta - \frac{\ell^2}{R^2}}\,. \tag{5.21}$$

Note that for detuning θ different from $2\beta I_s$ and for ℓ^2/R^2 small, e.g. for small magnitudes of OAM and large radii, the critical wave vectors from Eq(5.14) and Eq(5.21) are approximately the same. We can then conclude that spatially periodic Turing patterns for $\ell \neq 0$ rotate along the ring with the angular velocity ω calculated in Eq(5.18). Historically, expressions for the angular velocity similar to Eq(5.18) have been numerically verified for self-trapped necklace-ring beams in a self-focusing nonlinear Schrödinger equation [97] and applied to rotating domain walls in optical parametric oscillators [98]. $I_s^c = 1/\beta$ remains unchanged by the inclusion of OAM and the instability threshold to observe Turing patterns remains the same.

5.3.4 Rotating Turing patterns

In view of these results, we can now better investigate the interplay between input fields with OAM due to helical phases and the resultant Turing structures on the ring. Above threshold, Turing patterns are spatially modulated structures with a peak (trough) to peak (trough) distance close to $\Lambda_c = 2\pi/k_c$ where k_c is the critical wave vector. We consider spatially modulated solutions of the ring LLE Eq(5.6) of the form

$$E(\phi,t) = F(\phi,t)e^{i\ell\phi} = A[Q(\phi,t)]\exp\{i\Phi[Q(\phi,t)] + i\psi\}e^{i\ell\phi} \tag{5.22}$$

where ψ is a constant phase and A and Φ are amplitude and phase functions that are periodic in the variable $q = \phi - \omega t$ and spatially normalised for Turing patterns of wave vectors k_c, given by:

$$Q(\phi,t) = k_c\, R\, q = k_c\, R\,(\phi - \omega t) \tag{5.23}$$

where ω is the angular frequency. By replacing Eq(5.22) in the ring LLE Eq(5.9) gives:

$$\begin{aligned} - \quad & k_c R\omega \left(\frac{\partial A}{\partial Q} + iA\frac{\partial \Phi}{\partial Q}\right) \exp\left(i\Phi + i\psi\right) = \\ & P_\ell + \left\{ - \left[1 + i\left(\theta + \frac{\ell^2}{R^2}\right)\right] A + i\beta A^3 \right. \\ + \quad & k_c^2 \left[i\frac{\partial^2 A}{\partial Q^2} - A\frac{\partial^2 \Phi}{\partial Q^2} - 2\frac{\partial A}{\partial Q}\frac{\partial \Phi}{\partial Q} - iA\left(\frac{\partial \Phi}{\partial Q}\right)^2 \right] \\ - \quad & \left. \frac{2\ell k_c R}{R^2}\left(\frac{\partial A}{\partial Q} + iA\frac{\partial \Phi}{\partial Q}\right) \right\} \exp\left(i\Phi + i\psi\right) . \end{aligned} \tag{5.24}$$

This demonstrates that above threshold, Turing patterns with an amplitude and a phase that are spatially modulated at the critical wave vector k_c are solutions of Eq(5.9) provided that they rotate at an angular velocity $\omega = 2\ell/R^2$.

As expected from the previous section, solution Eq(5.22) is a stationary state of Eq(5.15) and rotates at the angular frequency ω. This is further demonstrated by the balance of the first and last terms in Eq(5.24). Eq(5.24) results in the following constraint for rotating Turing patterns

$$\begin{aligned} P_\ell \exp\left(-i\psi\right) = & \left\{ \left[1 + i\left(\theta + \frac{\ell^2}{R^2}\right)\right] A - i\beta A^3 \right. \\ & \left. -k_c^2 \left[i\frac{\partial^2 A}{\partial Q^2} - A\frac{\partial^2 \Phi}{\partial Q^2} - 2\frac{\partial A}{\partial Q}\frac{\partial \Phi}{\partial Q} - iA\left(\frac{\partial \Phi}{\partial Q}\right)^2 \right] \right\} \exp\left(i\Phi\right) \end{aligned} \tag{5.25}$$

To summarise, our analysis suggests the existence of Turing pattern solutions that rotate at an angular velocity of $\omega = 2\ell/R^2$ and are formed by $N = k_c R$ peaks with separation $\Lambda_c = 2\pi/k_c$ along a ring of radius R, where $k_c = \sqrt{2\beta I_s - \theta - \ell^2/R^2}$. Moreover, these solutions must satisfy Eq(5.25).

We verify this numerically by integrating Eq(5.6). Note that we consider $\beta = 2/3$ throughout because of its connection to the two orthogonal polarisation case [99] but all considerations apply to generic values of β since its change simply corresponds to a renormalisation of E and P. Figure(5.2) shows the resulting amplitude (red) of the field E along the ring for $I_s = 2$, $\theta = 5/3$, $\ell = 1$ and $R = 6$. In this case $k_c \approx 1$ and we see a pattern consisting of 6 peaks, as we would expect given that $k_c R \approx 6$. We also

show (in blue) that the right hand side of Eq(5.25) evaluated numerically via Eq(5.6) is indeed equal to the value of P_ℓ, as determined by Eq(5.11).

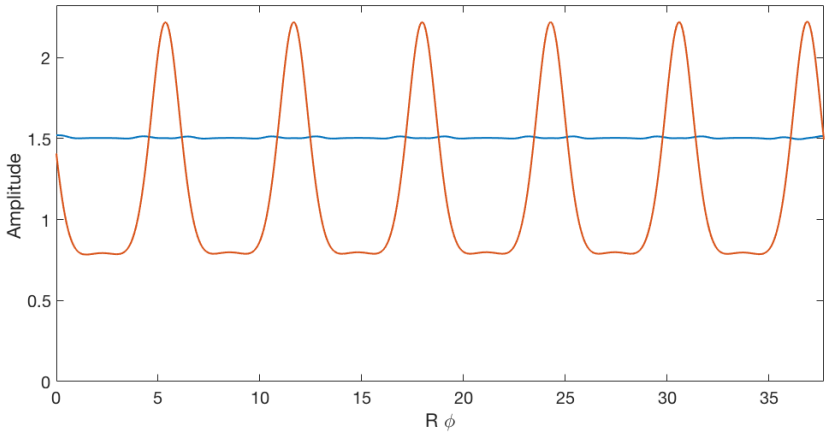

FIGURE 5.2: Amplitude of the rotating Turing pattern (red line) and numerical evaluation of the rhs of Eq. (5.25) (blue line). Parameters are $I_s = 2$, $\beta = 2/3$, $\theta = 5/3$ and $N = 6$.

To verify that the angular velocity is given by Eq(5.18), in Figure(5.3) we plot the time evolution of the amplitude of the field E along the ring for the same parameters of Figure(5.2). We can write $t = \phi/\omega = (R\phi)/(R\omega) = (R\phi)(R/2\ell)$ if $\omega = 2\ell/R^2$. The red lines correspond to the movement of the position of the peaks in Figure.5.2 over time. For a stationary solution the result would be vertical red lines since the position of the peaks would remain constant with time. However since we are pumping with a pump with an $\exp(i\ell\phi)$ dependence we instead observe that the peaks evolve in time. The gradient of the red lines in Figure(5.3) therefore give the angular velocity of the peaks which we can compare with our analytical result in Eq(5.18). From Figure(5.2) we can see that there are six peaks ($N = 6$) therefore for an OAM of $\ell = 1$ we calculate the expected slope of the red lines in Figure(5.3) to be 3 as expected.

Finally we have confirmed the variation of the pattern wave vector due to the factor ℓ^2/R^2 in Eq(5.21) by performing simulations for large ℓ and small R, in this case $\ell = R = 4$. Using $I_s = 1.6$, $\beta = 2/3$ and $\theta = 2\beta I_s - 1 - \ell^2/R^2$, to guarantee $k_c = 1$, we find that the correct pattern of four peaks is formed when starting from small noise,

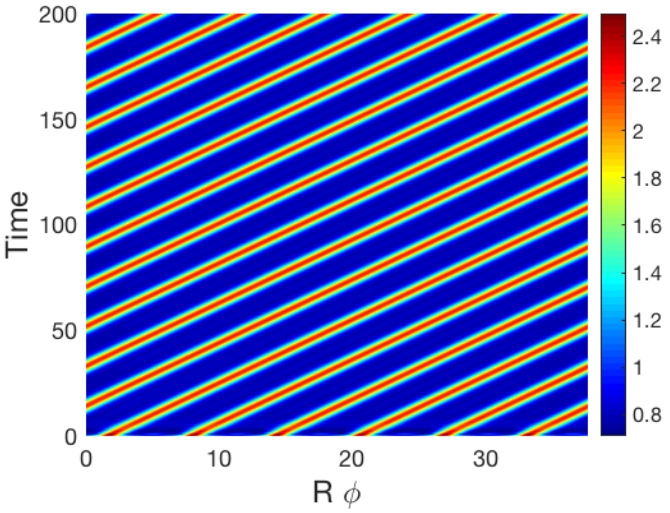

FIGURE 5.3: Time evolution of a rotating Turing pattern on a ring with OAM of $\ell = 1$ from Eq(5.6). Parameters are $I_s = 2$, $\beta = 2/3$ and $\theta = 5/3$. Red lines correspond to peaks shown in Figure(5.2)

as shown in Figure(5.4). However, when the corrective term ℓ^2/R^2 is not included an incorrect number of peaks is obtained.

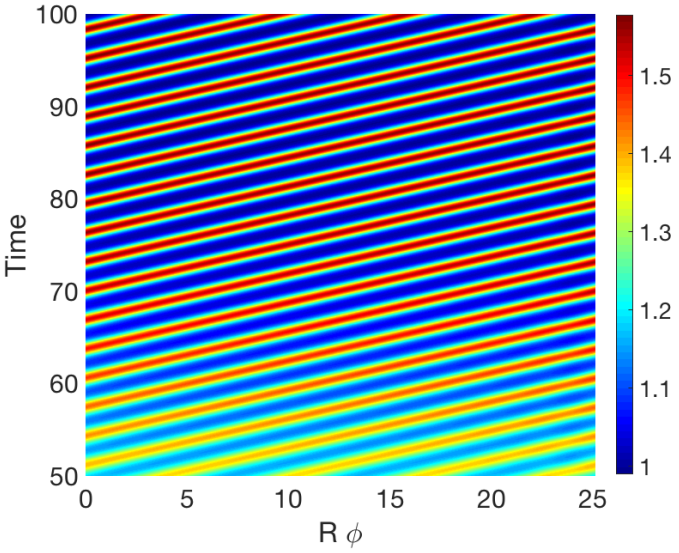

FIGURE 5.4: Time evolution of a rotating Turing pattern on a ring with OAM of $\ell = 4$ and $R = 4$ from Eq. (5.6). Parameters are: $I_s = 1.6$, $\beta = 2/3$ and $\theta = 2\beta I_s - 1 - \ell^2/R^2$ to guarantee $k_c = 1$.

5.4 Scalar 2D case

5.4.1 Input pumps of LG mode shape

We now consider two dimensional solutions to the Lugiato-Lefever equation in Eq.(LL2D), using a Laguerre-Gauss pump. A Laguerre-Gauss beam as the pumping mode most closely relates to the previous one dimensional analysis as it corresponds to wrapping the periodic boundary conditions into a ring mode. Here we compare the behaviour using the one dimensional analysis with the numerical results using an LG pump. Figure(5.5) shows the transverse intensity profile for an LG pump of $\ell = 1$ above the Turing instability threshold for a small and large beam waist. We observe the formation of a set of peaks equally separated by a distance which again is close the wavelength of the Turing structure, hence the number of peaks can easily be controlled. In the one dimensional case the number of peaks was controlled by the radius, R. Similarly in the LG pump case the number of peaks can be controlled by changing the beam waist of the mode to control the radius and circumference of maximum intensity of the ring, as shown in Figure(5.5). As LG modes by nature contain a phase gradient the cause and nature of the rotation of the structure is trivial as cavity solitons have been shown to move in the presence of phase gradients.

In order to measure the rotation rate of the structure the position of a particular peak is tracked over many images and the gradient of position against time is calculated as in Figure(5.3) and Figure(5.4). In Figure(5.6) we show how the angular velocity of the Turing structure changes as the beam waist of the OAM beam is altered. We show the result for four different beam waists by the coloured dots for $\ell = 1$ (blue), 2 (cyan) and 3 (purple). The dependence of the angular velocity as a function of the radius R is also plotted for the analytical results in Eq(5.18) in the dashed coloured lines (red, yellow and green for ℓ =1,2 and 3 respectively) and we can see excellent agreement between the numerical results for a two dimensional LG mode and the analytical result of the previous section.

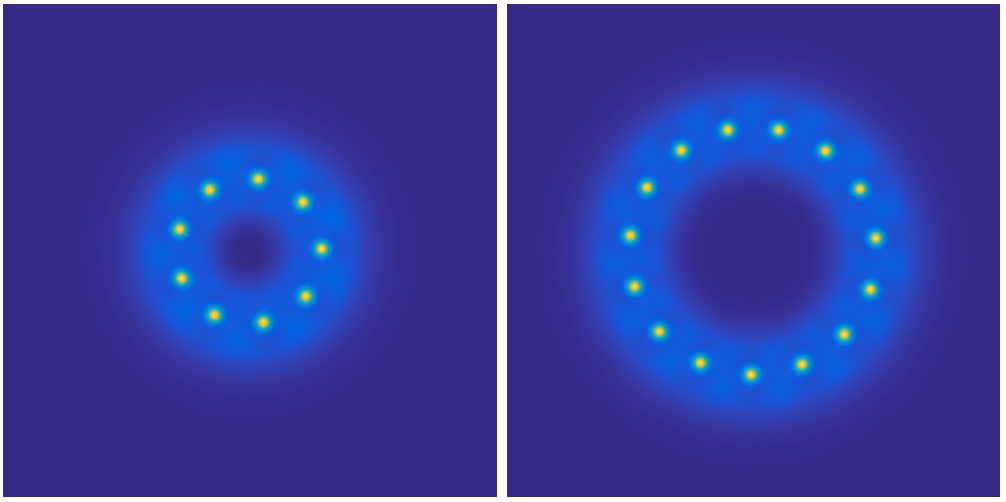

FIGURE 5.5: Final intensity of the field E from Eq. (5.4) using a Laguerre-Gauss pump with $\ell = 1$. Parameters are: $I_s = 1.45$, $\beta = 2/3$ and $\theta = 1$, $\ell = 1$ for a small beam waist containing 9 peaks (left panel) and a large beam waist of 15 peaks (right panel).

5.4.2 tophat input pumps

We now consider the 2D case where the input pump has a tophat shape amplitude multiplied by an azimuthal phase:

$$P = \frac{P_\ell}{2}\left[1 - \tanh\left(S(r - r_t)\right)\right] e^{i\ell\phi}\,, \tag{5.26}$$

where P_ℓ is a complex amplitude independent of ϕ, S and r_t control the steepness of the sides and the radius of the tophat, respectively, and ℓ is an integer corresponding to the topological charge of the optical vortex, as before.

When $\ell = 0$, diffraction due to the finite size of the pump induces concentric rings whose amplitudes decrease from the outer ring inwards. The amplitude of the outermost ring increases with the steepness of the sides of the pump, and this may allow its intensity to go above the Turing instability, $I_s^c = 1/\beta$ and the pattern to form. In this case, the distance between concentric rings is close to the critical wavelength Λ_c along the radial direction, see the solid red line in the left panel of Figure(5.7). Once the pattern has formed on the outer ring, we observe a sequence of azimuthal instabilities on the

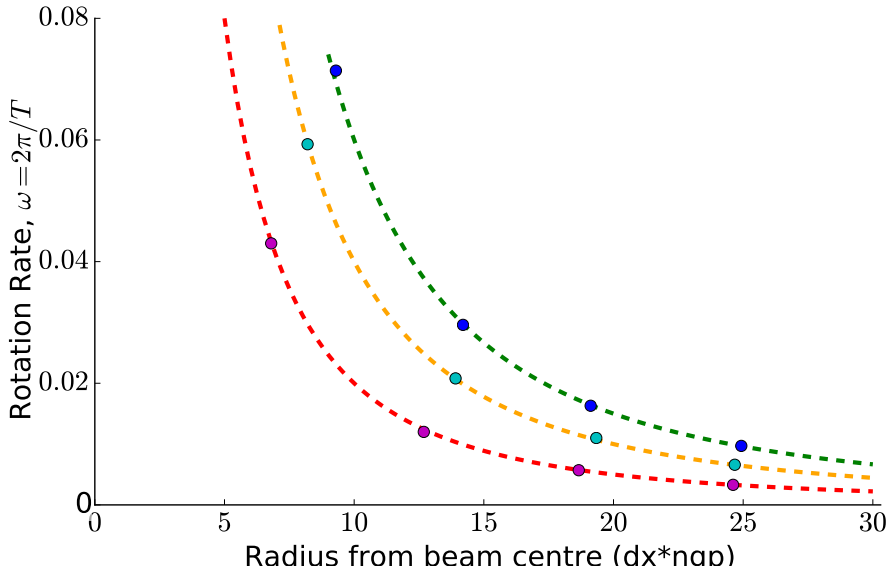

FIGURE 5.6: Angular velocity of the rotating ring patterns for a scalar Laguerre-Gauss beam versus $2\ell/R^2$ for $\ell = 1, 2$ and 3. The coloured dots represent the numerical measurement of the angular velocity and the dashed lines are the analytical prediction from Eq(5.18).

smaller and smaller rings. A number of peaks form on each ring, separated by the critical wavelength corresponding to the radial length of the particular diffraction ring. The final patterns for $\ell = 0$ are stationary (note that there is some initial transition and movement around until they fit, for example, a hexagonal structure in a circular pump). Patterns on the outermost diffraction ring are similar to the well-known daisy or sunflower patterns as observed in VCSELs with an electronic pump with a steep oxide confinement [100].

When the pump carries OAM, i.e. $\ell \neq 0$, the phase at the centre of the pump is undefined and hence the field at the origin has to be zero, as is typical for Laguerre-Gauss modes [24]. This is a fundamental difference with respect to the one dimensional case. The physical effect of this on-axis vortex is the induction of diffractive rings close to the centre of the beam, see the dashed blue line in the left panel of Figure(5.7). In this case the intensity of the inner ring may exceed I_s^c and undergo an azimuthal Turing instability. The distance between the rings along the radial direction is again close to the critical wavelength Λ_c, and once the pattern has formed on the inner ring we

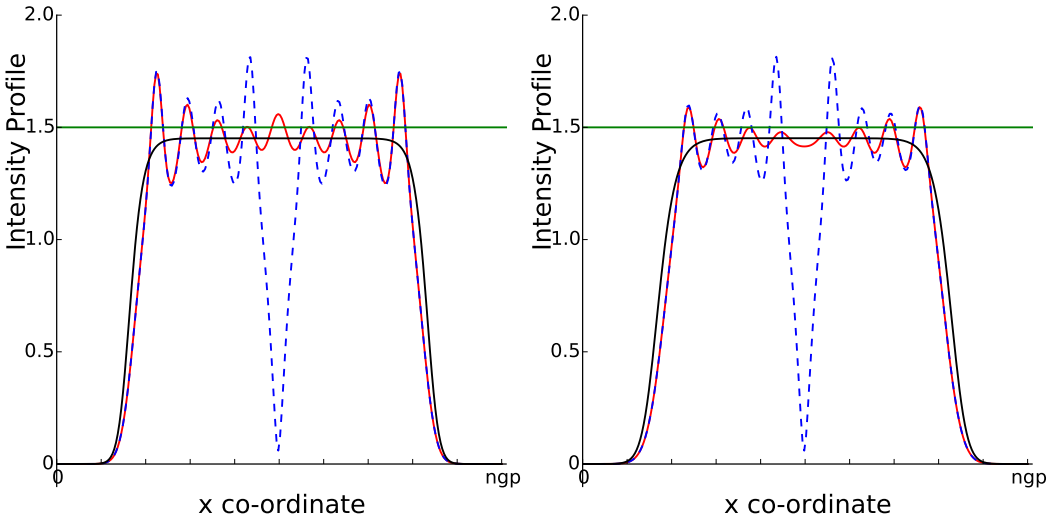

FIGURE 5.7: Left: Cross-section of intensity of pump (black) and fields for $\ell = 0$ (red) and $\ell = 1$ (dashed blue) where both displaying the radial modulation at the critical wave vector k_c. Right: The same but when tophat is not steep enough for Turing instability in the case $\ell = 0$. Green line is pump intensity threshold for Turing instability. Parameters are: $I_s = 1.45$, $\beta = 2/3$ and $\theta = 1$. Note that although the models and numerical solutions are calculated based on R and ϕ we have labelled the position as the x co-ordinate to represent we are taking a cross-section through the transverse plane.

observe a sequence of azimuthal instabilities on the larger and larger rings. As before, the number of peaks is separated by the critical wavelength corresponding to the radial length of the particular diffraction ring, although modified by the factor ℓ^2/R^2.

Close to the Turing instability, the radial wave vector for $\ell = 1$ is almost the same as that for $\ell = 0$ (see Figure(5.7) right panel). However, the size of the central vortex increases with increasing OAM, ℓ, and alters the radial wave vector in the vicinity of the vortex. Figure(5.7) right panel is there to show that the wavelength of the ripples is not Λ_c when the field is not far enough above the Turing instability. This can be observed by comparing the difference in the distance between ripples between the red and dashed blue lines of the right hand panel.

Figure(5.8) shows the time evolution of the 2D amplitude of the field E from Eq. (5.4) after the first azimuthal instability of the inner diffraction ring. By adjusting the steepness of the sides of the tophat and/or the OAM of the vortex we can control

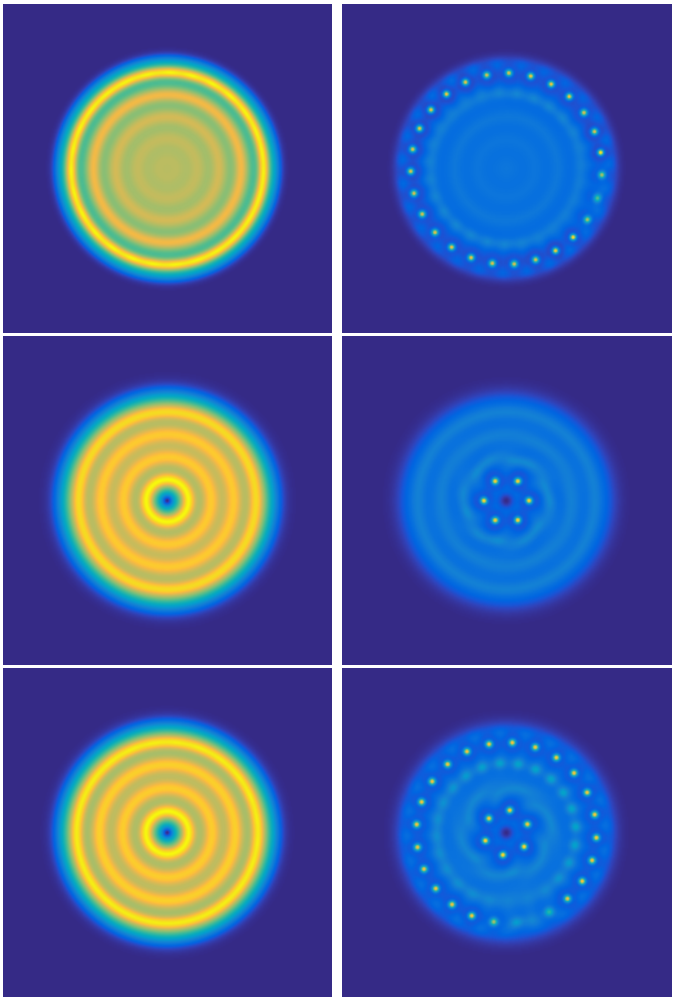

FIGURE 5.8: 2D amplitude of the field E from Eq(5.4) showing initial diffraction rings (left column) and at the first azimuthal instability (right column). Parameters are: $I_s = 1.45$, $\beta = 2/3$ and $\theta = 1$, $\ell = 0$ (top panel) and $\ell = 1$ (middle & bottom panels). Left hand panels show the initial diffraction rings, right hand panels show the start of the Turing instability. In the top panels the steepness of the tophat has been chosen such that the vortex slope is shallower than the tophat slope and the pattern starts on the outermost ring first. The middle panels show when the vortex slope is steeper and the pattern presents first on the inner ring. In the bottom the steepness of the tophat has been chosen to match that of the vortex such that the pattern starts on both inner and outer rings simultaneously.

whether the Turing instability first occurs on the inner or the outer ring, or even on both simultaneously. Ring by ring azimuthal instabilities can occur from the outside to the inside, or vice versa depending on where the pattern is first formed, or may even collide as shown in Figure(5.9). We can see that the instability occurs simultaneously on the inner and outer rings which in turn excites the formation of the Turing instability on neighbouring rings. After successive excitations the two propagating instabilities collide.

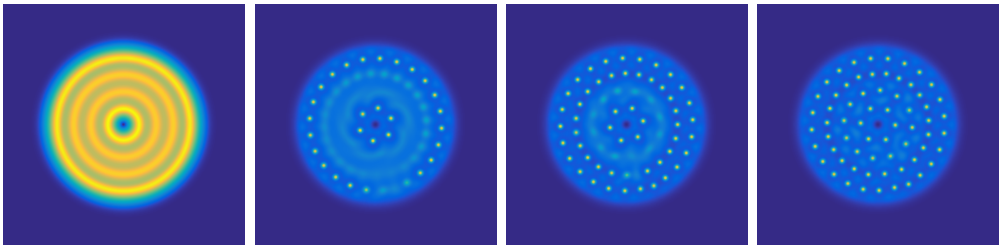

FIGURE 5.9: Transverse in intensity of the tophat solutions for (a) initial diffraction rings, (b) initial instability on both inner and outer rings, (c) excitation of neighbouring rings and (d) collision of the two instabilities.

Whatever the mechanism of ring excitation (innermost or outermost), for $\ell \neq 0$ Turing patterns appear on the first excited ring and start to rotate before the next ring is excited. This leads to concentric Turing pattern rings where the peaks are seen to rotate at exactly the angular frequency given by Eq(5.18) with R equal to the radius of the specific diffraction ring, see Figure(5.10). Each ring appears to be completely decoupled from the rest of the structure, meaning that they behave as independent 1D structures although embedded in a 2D field and rotate at the frequency given by Eq(5.18) with R equal to the radius of the specific diffraction ring. If the steepness of the sides of the tophat pump is increased, diffraction effects of the finite pump size can be enhanced on the outer rings of the field E. This phenomenon leads to well-known daisy or sunflower patterns as observed in VCSELs with an electronic pump with a steep oxide confinement [100]. We observe daisy-like pattern formation on the outermost diffraction ring in our simulations with OAM different from zero. Again, ring by ring azimuthal instabilities take place but in this case from the the outside to the inside. The two mechanisms of ring by ring instabilities, outward and inward,

can even collide as shown in Figure(5.9). The nature of the decoupled rings on the tophat is shown in Figure(5.10) which shows the final amplitude of a tophat field where the Turing structure has presented on all diffraction rings. The coloured circles show each of the diffraction rings over which we measure the angular velocity. This angular velocity of each of the separate rings is then plotted against their radius to show that each of them rotate at Eq(5.18).

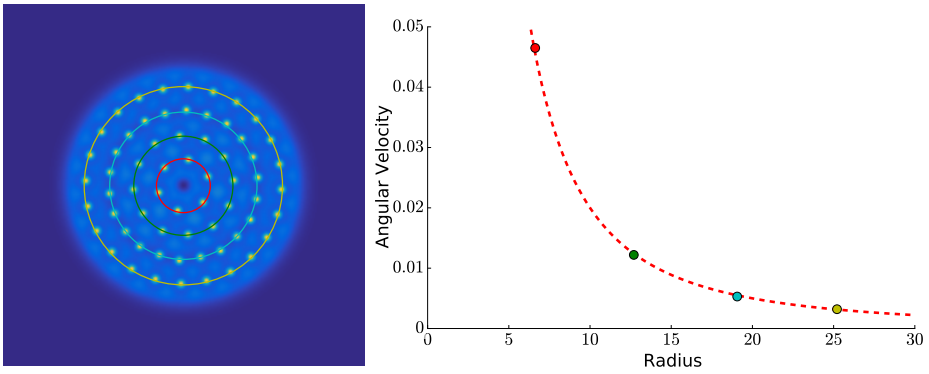

FIGURE 5.10: Left panel: Final amplitude of the field E from Eq. (5.4). Parameters are: $I_s = 1.45$, $\beta = 2/3$ and $\theta = 1$, $\ell = 1$ (corresponding to final result from middle panel of Figure(5.8)). The coloured circles show each of the rings. Right panel: Angular velocity of each of the Turing rings calculated numerically and shown via the coloured dots. Each dot represents the rotation rate of the corresponding coloured ring in the left panel. The dashed line represents the analytical $2\ell/R^2$ dependence from Eq(5.18).

5.5 Full Vector Case

Finally, we now consider the full vector case where the input pump to the cavity is a fully structured light mode composed of two Laguerre-Gauss modes of orthogonal polarisations. Recall that the a FSL beam is given by Eq(2.38) as

$$\begin{aligned} \mathbf{E} &= \mathbf{E}_R + \mathbf{E}_L \\ &= \sin(\gamma)\mathbf{LG}_{p_R}^{\ell_R}\mathbf{e}_R + e^{i\beta}\cos(\gamma)\mathbf{LG}_{p_L}^{\ell_L}\mathbf{e}_L. \end{aligned} \tag{5.27}$$

In the previous sections the position at which the Turing structure formed was trivial and on the radius of peak intensity of the pump mode. However now we are considering fully structured light composed of two beams, hence when the modes in the superposition have different OAM there are two rings of maximum intensity which the pattern can form. The position at which the Turing structure forms is non trivial and depends upon the beam waist, biases and OAM of the given modes within the superposition.

However, using a FSL beam as the pump gives more control over the angular velocity of the structure. Since both of the modes in the superposition contributes to both the intensity structure and the rotation rate of the pattern the behaviour of the output of the cavity is no longer analytical or trivial. In this section we will consider a variety of cases for different beam waists, bias and OAM of the FSL input pump and detail the behaviour of the Turing structure as a result of controlling these parameters.

5.5.1 Below pattern threshold

Firstly we consider cavity intensities below pattern threshold to see the effect of the cavity upon the behaviour of the polarisation of the modes. This is slightly more complex than in the scalar case since the addition in intensity of each of the modes must be taken into consideration for the pattern threshold. The top row of Figure(5.11) gives the transverse intensity and polarisation distribution for the same FSL beams as detailed in Figure(4.3). We can see that below the Turing instability threshold that the polarisation distribution and intensity is the same as in Figure(4.3) highlighting that there is no change in the intensity or polarisation distribution. The bottom row shows the transverse intensity and polarisation distribution above the Turing instability where we can see the formation of peaks evenly separated again by the wavelength of the Turing structure Λ_c. The polarisation distribution interestingly is unaffected by the formation of the peaks.

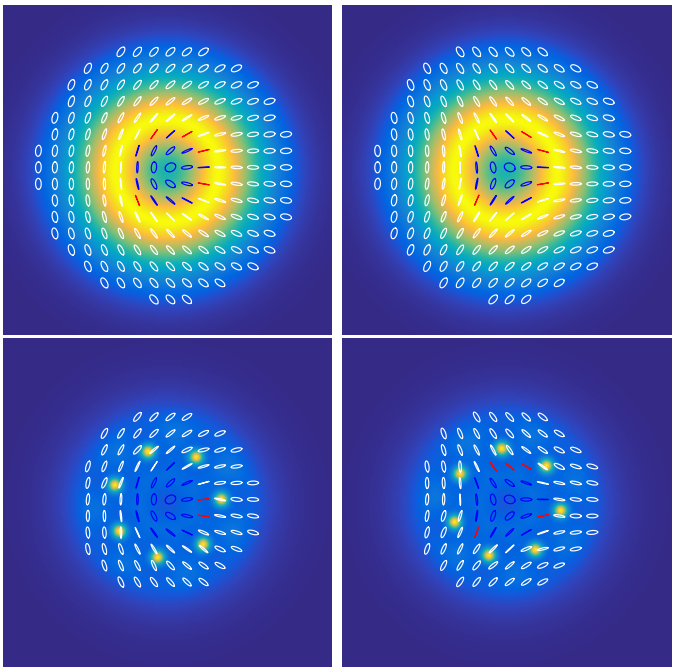

FIGURE 5.11: Transverse intensity structure and polarisation distribution at the output of the cavity for a fully structure light beam below Turing threshold (top row) and once the pattern has developed (bottom row). The left hand column is for a lemon beam composed of $\ell_R = 1$ and $\ell_L = 0$ and the right hand column is for a star beam composed of $\ell_R = 1$ and $\ell_L = 0$. For both beams $\beta = \pi/4$ and $\gamma = 0$

5.5.2 Cylindrical Vector Beams - $|\ell_R| = |\ell_L|$ and $\gamma = \frac{\pi}{4}$

Above pattern threshold we observe the same regular ring structure form on the OAM modes where the intensity overlap is greatest. Intuitively for the trivial case for a vector beam composed of equal but opposite OAM in the right and left circularly polarised modes and of equal amplitudes there would be no net rotation of the structure. Indeed we find numerically that there is no rotation and the transverse structure at the output of the cavity is stationary. Since there is perfect intensity overlap between each mode as the OAM and amplitudes are equal the radius at which the structure forms is trivial and occurs at the radius of peak intensity given by $r = \omega_0\sqrt{|\ell|/2}$. Additionally, from the perfect overlap, the rotational contribution from each of the modes in the FSL will cancel, resulting in a stationary Turing structure with no rotation.

5.5.3 Biased OAM modes - $\ell_R = \ell_L$ and $\gamma \neq \frac{\pi}{4}$

We now analyse the behaviour when the relative intensity between the two modes in the FSL superposition is not equal. The bias between the two modes is controlled through the γ term in Eq(5.27). From Eq(5.18) we have analytically calculated the angular velocity for $\gamma = 0$ and $\gamma = \pi/2$ since these cases correspond to the scalar case in which there is only one mode at the input to the cavity. We also know that for $\gamma = \pi/4$ (a balanced vector beam) the Turing pattern is stationary and the angular velocity is zero. It is not clear, however, how the rotation rate is affected by the change of bias between these points as the relative intensities of the modes is altered.

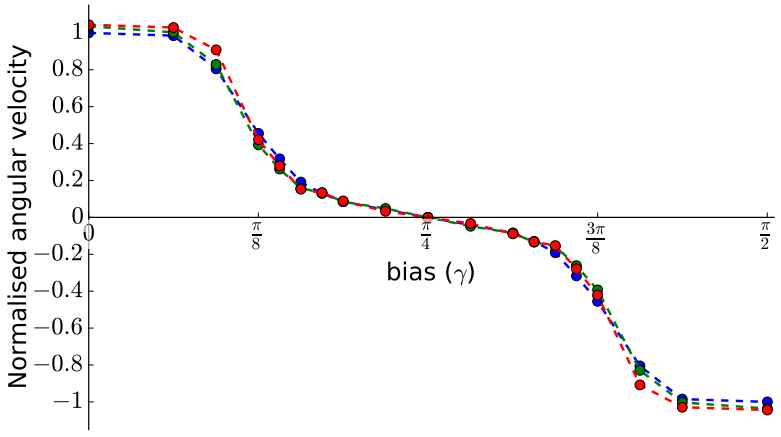

FIGURE 5.12: Angular velocity of the rotating ring pattern versus the intensity bias between the modes of a fully structured light composed of $\ell = \pm 1$ (blue), $\ell = \pm 2$ (green) and $\ell = \pm 3$ (red). Again the coloured dots are the numerically calculated angular velocities of the Turing structure. The beam waist is the same for all 3 compositions of FSL (the radius for the structure is given by $r = w_0\sqrt{|\ell|/2}$. The angular velocity has been normalised by that of $\ell = \pm 1$ for $\gamma = 0$.

Figure(5.12) details the behaviour of the angular velocity against the bias between the modes of the FSL superposition for an OAM of 1 (blue), 2 (green) and 3 (red). The circular points show the data points for which the angular velocity of the Turing pattern has been measured numerically. For clarity the rotation rate has also been normalised by the rotation rate of the $\ell = 1$ ($\gamma = 0$) scalar beam. As can be seen, the behaviour for each of the different OAMs is the same and the angular velocity of the Turing structure for the FSL beam depends purely on the difference between the intensities of the modes.

This is due to the fact that the increase in OAM is exactly compensated for by the increase in the radius at which the Turing structure forms. Recall that the radius of peak intensity for a Laguerre-Gauss beam is given by $r_{peak} = w_0\sqrt{|\ell|/2}$, which can be substituted into Eq(5.18);

$$\begin{aligned} \omega &= \frac{2\ell}{R^2}, & (5.28)\\ &= \frac{2\ell}{(w_0\sqrt{|\ell|/2})^2}, & (5.29)\\ &= \pm\frac{4}{w_0^2}, & (5.30) \end{aligned}$$

i.e. independent of the OAM of the FSL beam.

If we instead decrease the beam waist of the higher order modes such that the peak of the LG mode and hence Turing pattern is at the same radius independent of the OAM, then we recover the intuitive behaviour that increasing the the OAM increases the angular velocity of the rotation of the pattern. Figure(5.13) shows the behaviour of the rotation rate against the bias between the modes of the FSL superposition where the beam waist is chosen such that the Turing pattern is at the same radius. We note that in this case, by doubling the OAM the angular velocity for the scalar case ($\gamma = 0, \pi/2$) is doubled. Between the case of the scalar mode and the balanced vector beam the change in angular velocity is non trivial and the curve for the $\ell_{L,R} = \pm 2$ is not simply two times the curve of the $\ell_{L,R} = \pm 1$. The ability to control the OAM, beam waist and bias allows full and very precise control over the angular velocity of the Turing pattern.

5.5.4 Decoupled OAM rings

In the case of a scalar tophat input we showed that individual rings of structured peaks become decoupled and rotate at an independent angular velocity given by Eq.5.18. In the case of fully structured light inputs, decoupled rings of independently rotating structures can be generated. This occurs when the peaks on each of the right and left handed circularly polarised modes are at a sufficiently different radius that there is no

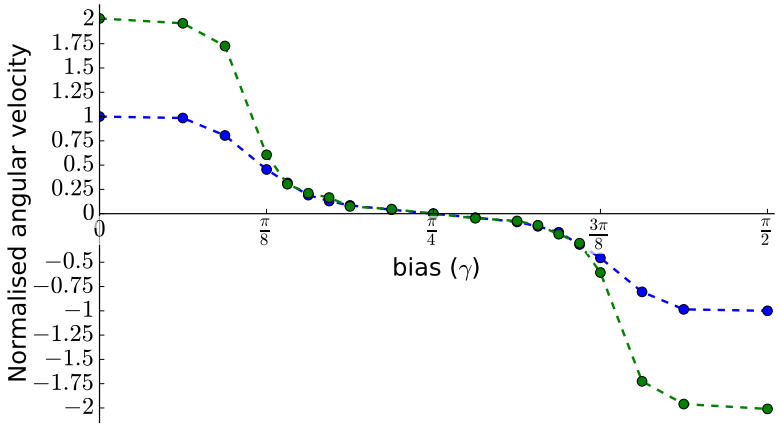

FIGURE 5.13: Angular velocity of the rotating ring pattern versus the intensity bias between the modes of a fully structured light composed of $\ell = \pm 1$ (blue) and $\ell = \pm 2$ (green) where this time the beam waist has been chosen so that the Turing pattern for each of the OAM values occurs at the same radius. The angular velocity has been normalised by that of $\ell = \pm 1$ for $\gamma = 0$.

interaction between each beam. When this criteria is met the cross phase modulation between the modes is negligible and the rings rotate independently, each with velocity according to Eq(5.18). Furthermore because each of the modes have orthogonal polarisation they can be tailored to rotate at various speeds and also in opposite directions. Such a configuration has useful applications in particle control and manipulation.

Such a state can be achieved via two methods. Firstly the value of OAM in each of the orthogonal modes can be chosen such that the magnitude of one is very much greater than the other, i.e. $\ell_R \gg \ell_L$ or $\ell_R \ll \ell_L$. Since the peak intensity of an OAM beam is given by $r = \omega_0\sqrt{|\ell|/2}$ the larger OAM mode will have a peak at a much larger radius. The left hand panel of Figure(5.14) shows the transverse intensity of a fully structured light mode composed of $\ell_R = 5$ and $\ell_L = -1$ and shows the direction of rotation for each ring. As demonstrated previously, the larger rotation rate due to increasing the OAM is counterbalanced by the larger radius and so the structure on each ring has the same angular velocity, although in opposite directions, hence both are labelled with ω_1. Because of the constraints of Eq.5.18 using this method to generate independently rotating rings will result in a fixed angular velocity for a given beam waist independent of the choice of OAM.

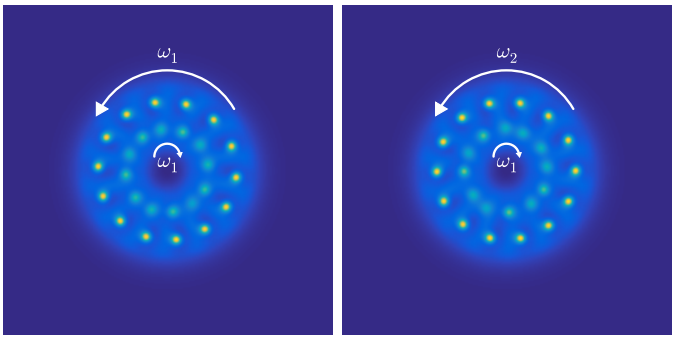

FIGURE 5.14: Left panel: Transverse intensity of an FSL mode composed of $\ell_R = 5$ and $\ell_L = -1$ where the direction of the arrows shows the direction of rotation of the structure for each of the different Turing rings. Both rings rotate with the same angular velocity ω_1. Right panel: Transverse intensity of an FSL mode composed of $\ell_R = 2$ and $\ell_L = -1$ where the inner ring rotates with the same angular velocity ω_1 but the outer ring now rotates at a smaller angular velocity of ω_2.

However by controlling both the OAM of the modes and the beam waist simultaneously, we can tailor the radius of maximum intensity for any choice of OAM such that we can fix the radius at which the Turing structure will form. This means that once the radius at which the peaks will occur is chosen, any OAM can be chosen to change the angular velocity of the pattern. Such a case is shown in the right panel of Figure(5.14) for a fully structured light mode of $\ell = 2$ and $\ell = -1$. The inner ring has the same beam waist, radius of peak intensity and the same OAM as the inner ring of the left panel and hence will still rotate clockwise with an angular velocity of ω_1. The outer ring, on the other hand, now has the same radius at which the Turing pattern occurs as the corresponding ring on the left panel but since the value of OAM is now lower, will rotate at a slower angular velocity as denoted by ω_2. By changing the beam waist of each of the modes and selecting a particular value of OAM we can generate rings of Turing instability with any chosen number of peaks, separated by any chosen distance and rotating at any chosen angular velocity.

5.6 Conclusion

Optical vortices and beams carrying OAM have been used widely in particle control and manipulation. Such states of light have an intensity gradient that can trap and move particles on the nanoscale. Such techniques have allowed the development of optical traps and optical tweezers. Hence it is important to be able to control and tailor the state of the optical field that allows complete control over the manipulation of atoms and molecules. Here we have demonstrated the behaviour of a fully structured light beam at the output to a vectorial Kerr cavity. Above the Turing instability threshold, a pattern forms on the ring which consists of evenly spaced intensity peaks separated by an equal distance given by the Turing wavelength Λ_c.

In the scalar case, where there is a single mode at the input, when the beam carries OAM the peaks rotate along the phase gradient. By considering the well known Lugiato-Lefever in one dimension we have shown analytically that the angular velocity of the Turing pattern is dependent purely on the OAM of the beam and the radius from the centre of the beam as given by Eq(5.18). Numerical results show good agreement in both the one dimensional case as well as with two dimensional solutions using Laguerre-Gauss and tophat beams as the pump. With the use of a tophat pump we can generate multiple Turing rings that rotate independently of each other at an angular velocity dependent on their radius from the centre of the beam. By controlling the steepness of the pump we can control where the Turing structure begins to form: outer edge of ring, centre of ring or both simultaneously.

In the full vector case, we observed that for a cylindrical vector beam where the relative intensity of the two modes is equal the rotational contribution from each beam cancels and the pattern is stationary. When the relative intensity between the two beams is changed we note that the behaviour of the angular velocity is non trivial due to the complex nature of the cross phase modulation as the bias is altered. However, we have shown that we can generate any angular velocity of the Turing structure between $\pm 2\ell/r^2$ by changing the relative intensity. Finally we showed by changing the beam

width and OAM we can recover the case of the tophat pump in which we can generate multiple independently rotating structures in which we have complete control over the number of peaks and their angular velocity around the OAM ring. Unlike the tophat pump, in this case we can even have structures rotating in opposite directions.

Chapter 6

Conclusion

Lasers are vital in modern technology to the point where there is barely an optical device that does not rely on the production of laser and laser pulses. Lasers are also put to use in medical science in diagnostics and even in operations [101]. In more recent times there has been a great deal of interest in controlling the structure and properties of laser light for a variety of applications such as material processing [88], microscopy [73] and optical trapping[78]. In this thesis we have attempted to show some of ways in which the intensity, phase and polarisation of light can be tailored in the transverse plane.

We have considered some of the interesting phenomena that arise when high intensity laser light interacts with a nonlinear medium. We have analysed the interaction with both second order $\chi^{(2)}$ and third order $\chi^{(3)}$ media, inside and outside of an optical cavity. For a second order nonlinear medium in an optical cavity, an optical parametric oscillator, we showed that by adding forcing into the system detuning can be introduced such that there is the presence of self-forming hexagonal structures [9]. By lowering the amplitude of the injected signal, the Turing structure becomes unstable first to a phase instability and then an amplitude instability. The resultant state is a dynamical solution of defect mediated turbulence [47] driven by defects of OAM ± 1 in the presence of helical waves. Interactions between defects result in the production of short lived

intensity peaks characteristic of rogue waves [36]. We have numerically analysed the state to determine that we do in fact observe rogue waves by considering a widely used definition of an extreme event threshold [38]. It was noted that this mechanism for the generation of defect mediated turbulence cannot be replicated by a superposition of random waves known as speckle. Finally we showed that this phenomena holds in the limit of finite boundary conditions and the parameter region where we predict the observation of rogue waves was given. These results can be useful in predicting the conditions that drive the onset of rogue waves by comparison to the hydrodynamic case [40].

Knowing and controlling the spatial polarisation distribution of a beam is important in applications such as optical tweezing and optical communications [81]. For a Kerr medium we analysed how the polarisation distribution of a fully structured light beam is affected by both linear and self-focussing nonlinear propagation. In the linear case we showed that the observed rotation of the polarisation ellipse is entirely down to the difference in Gouy phase between the two eigenmodes in the FSL beam. For a nonlinear propagation we explored the effect of cross-phase modulation, which when combined with the self-focussing and diffraction results in an evolving spatial overlap of the eigenmodes. Selection of physical parameters such as the beam size, the amount of Kerr nonlinearity, input power and the choice of OAM in the eigenmodes the rotation of the polarisation distribution can be controlled. Being able to control both the intensity and polarisation distribution can be of use in a variety of application where the particular transverse distribution is of importance such as atomic state preparation and atomic manipulation [77, 79, 80].

Finally we considered the effect an optical cavity would have on the interaction between fully structured light and a Kerr medium. Above a Turing threshold we observe the formation of regularly spaced intensity peaks on the intensity ring of the FSL beam. Where there is a net orbital angular momentum the Turing structure is seen to rotate. By considering the well known Lugiato-Lefever in one dimension we were able to analytically calculate the angular velocity of the Turing pattern for a scalar beam (one mode)

and showed good agreement with the numerical results for both the one dimensional and two dimensional solutions. In the FSL case where the relative amplitudes of the eigenmodes are not equal we showed the the rotation rate of the structure is non-trivial, however we can generate any desired rotation rate between a stationary structure and that of the scalar case. Furthermore by controlling the OAM and beam waist we can generate separate Turing rings that can rotate independently at any chosen angular velocity in the same direction or counter-rotating. This level of control over optical peaks can be of use in particle control and manipulation as well as in trapping.

References

[1] A. Einstein, Physikalische Zeitschrift **18**, 121 (1917).

[2] J. P. Gordon, H. J. Zeiger, and C. H. Townes, Phys. Rev. **99**, 1264 (1955).

[3] K. Shimoda, T. C. Wang, and C. H. Townes, Phys. Rev. **102**, 1308 (1956).

[4] N. Bloembergen, Phys. Rev. **104**, 324 (1956).

[5] A. L. Schawlow and C. H. Townes, Phys. Rev. **112**, 1940 (1958).

[6] T. H. Maiman, Nature **187**, 493 (1960).

[7] P. A. Franken, A. E. Hill, C. W. Peters, and G. Weinreich, Phys. Rev. Lett. **7**, 118 (1961).

[8] J. A. Giordmaine and R. C. Miller, Phys. Rev. Lett. **14**, 973 (1965).

[9] G.-L. Oppo, A. M. Yao, and D. Cuozzo, Phys. Rev. A **88**, 043813 (2013).

[10] J. Kerr, Philosophical Magazine **50**, 337 (1875).

[11] F. Bouchard, H. Larocque, A. M. Yao, C. Travis, I. De Leon, A. Rubano, E. Karimi, G.-L. Oppo, and R. W. Boyd, Phys. Rev. Lett. **117**, 233903 (2016).

[12] C. J. Gibson, P. Bevington, G.-L. Oppo, and A. M. Yao, Phys. Rev. A **97**, 033832 (2018).

[13] C. E. M. Strauss and D. J. Funk, Opt. Lett. **16**, 1192 (1991).

[14] R. W. Boyd and A. L. Gaeta, *Chaos in Nonlinear Optics* (Springer US, Boston, MA, 1991), pp. 99–105.

[15] R. Fitzpatrick, *Maxwell's Equations and the Principles of Electromagnetism* (Infinity Science Press LLC, Massachusetts, MA, 2008), 1st ed.

[16] J. D. Jackson, *Classical Electrodynamics* (Wiley, New York, NY, 1999), 3rd ed.

[17] R. W. Boyd, *Nonlinear Optics* (Academic Press, Burlington, 2008), 3rd ed.

[18] B. Saleh and M. Teich, *Fundementals of Photonics* (Wiley, New York, NY, 1991), 2nd ed.

[19] A. Siegman, *Lasers* (University Science Books, 1986).

[20] J. Hamazaki, Y. Mineta, K. Oka, and R. Morita, Opt. Express **14**, 8382 (2006).

[21] H. Kogelnik and T. Li, Appl. Opt. **5**, 1550 (1966).

[22] M. Lax, W. H. Louisell, and W. B. McKnight, Phys. Rev. A **11**, 1365 (1975).

[23] S. Barnett and R. Zambrini, *Quantum Imaging* (Singapore: Springer, K I Kolobov ed, 2007).

[24] A. M. Yao and M. J. Padgett, Adv. Opt. Photon. **3**, 161 (2011).

[25] L. Allen, M. W. Beijersbergen, R. J. C. Spreeuw, and J. P. Woerdman, Phys. Rev. A **45**, 8185 (1992).

[26] J. Hough, Astronomy & Geophysics **47**, 3.31 (2006).

[27] B. J. Zeng, R. W. Ni, J. Z. Huang, Z. Li, and X. S. Miao, Journal of Optics **16**, 125402 (2014).

[28] A. M. Beckley, T. G. Brown, and M. A. Alonso, Opt. Express **18**, 10777 (2010).

[29] E. J. Galvez, S. Khadka, W. H. Schubert, and S. Nomoto, Appl. Opt. **51**, 2925 (2012).

[30] Q. Zhan, Adv. Opt. Photon. **1**, 1 (2009).

[31] B. S. White and B. Fornberg, Journal of Fluid Mechanics **355**, 113 (1998).

[32] M. Onorato, S. Residori, U. Bortolozzo, A. Montina, and F. Arecchi, Physics Reports **528**, 47 (2013).

[33] A. Abrashkin and A. Soloviev, Physics Reports **110**, 014501 (2013).

[34] F. Fedele, J. Brennan, S. Ponce de Len, J. Dudley, and F. Dias, Scientific Reports **6**, 27715 (2012).

[35] S. Birkholz, C. Brée, A. Demircan, and G. Steinmeyer, Phys. Rev. Lett. **114**, 213901 (2015).

[36] NOAA, *What is a rogue wave?* (2018), URL `https://oceanservice.noaa.gov/facts/roguewaves.html`.

[37] M. Onorato, S. Residori, U. Bortolozzo, A. Montina, and F. Arecchi, Physics Reports **8**, 755 (2014).

[38] J. Dudley, F. Dias, M. Erkintalo, and G. Genty, Nature Phot. **8**, 755 (2014).

[39] D. R. Solli, C. Ropers, P. Koonath, and B. Jalali, Nature **450**, 1054 (2007).

[40] K. Dysthe, H. E. Krogstad, and P. Mller, Annual Review of Fluid Mechanics **40**, 287 (2008).

[41] A. Montina, U. Bortolozzo, S. Residori, and F. T. Arecchi, Phys. Rev. Lett. **103**, 173901 (2009).

[42] C. Bonatto, M. Feyereisen, S. Barland, M. Giudici, C. Masoller, J. R. R. Leite, and J. R. Tredicce, Phys. Rev. Lett. **107**, 053901 (2011).

[43] C. Liu, R. E. C. van der Wel, N. Rotenberg, L. Kuipers, A. Krauss, T. F. Di Falco, and A. Fratalocchi, Nature **11**, 358 (2015).

[44] Y.-Y. Wang, J.-T. Li, C.-Q. Dai, X.-F. Chen, and J.-F. Zhang, Physics Letters A **377**, 2097 (2013).

[45] Y.-Y. Tsai, J.-Y. Tsai, and L. I, Nature Physics **12**, 573 (2016).

[46] R. Adler, Proc. IRE **34**, 351 (1964).

[47] P. Coullet, L. Gil, and J. Lega, Phys. Rev. Lett. **62**, 1619 (1989).

[48] C. Hemming and R. Kapral, Physica D: Nonlinear Phenomena **168** (2002), ISSN 0167-2789.

[49] Q. Ouyang and J.-M. Flesselles, Nature **379**, 143 (1996).

[50] E. Bodenschatz, W. Pesch, and G. Ahlers, Annual Review of Fluid Mechanics **32**, 709 (2000).

[51] W. Cousins, M. Onorato, A. Chabchoub, and T. P. Sapsis, Phys. Rev. E **99**, 032201 (2019).

[52] A. D. Cattrell, M. Srokosz, B. I. Moat, and R. Marsh, Journal of Geophysical Research: Oceans **123**, 5624 (2018).

[53] L. Mandel and E. Wolf, *Optical Coherence and Quantum Optics* (Cambridge University Press, 1995).

[54] A. N. Vamivakas, B. E. A. Saleh, A. V. Sergienko, and M. C. Teich, Phys. Rev. A **70**, 043810 (2004).

[55] H. Di Lorenzo Pires, F. M. G. J. Coppens, and M. P. van Exter, Phys. Rev. A **83**, 033837 (2011).

[56] P. G. Kwiat, K. Mattle, H. Weinfurter, A. Zeilinger, A. V. Sergienko, and Y. Shih, Phys. Rev. Lett. **75**, 4337 (1995).

[57] C. J. Gibson, A. M. Yao, and G.-L. Oppo, Phys. Rev. Lett. **116**, 043903 (2016).

[58] C. Mayol, R. Toral, C. R. Mirasso, and M. A. Natiello, Phys. Rev. A **66**, 013808 (2002).

[59] F. Prati, G. Tissoni, C. McIntyre, and G. Oppo, Eur. Phys. J. D **59** (2010).

[60] J. Dainty, *Laser Speckle and Related Phenomena* (CRC Press, 2001), 1st ed.

[61] M. V. B. M. R. Dennis, Proc. R. Soc. London. A **452**, 2059 (2000).

[62] P. Broersen, *Automatic Autocorrelation and Spectral Analysis* (Springer, 2006), 1st ed.

[63] K. Staliunas, Phys. Rev. A **48**, 1573 (1993).

[64] M. Brambilla, F. Battipede, L. A. Lugiato, V. Penna, F. Prati, C. Tamm, and C. O. Weiss, Phys. Rev. A **43**, 5090 (1991).

[65] H. G. Solari and G.-L. Oppo, Optics Communications **111**, 173 (1994).

[66] M. Zimmermann, M. Natiello, and H. Solari, Chaos **11**, 500 (2001).

[67] T. Frisch and J. Gilli, J. Physique II **5**, 561 (1995).

[68] S. Barland, M. Brambilla, L. Columbo, B. Garbin, C. J. Gibson, M. Giudici, F. Gustave, C. Masoller, G.-L. Oppo, F. Prati, et al., in *Nonlinear Guided Wave Optics* (IOP Publishing, 2017), 2053-2563, pp. 1–1 to 1–28.

[69] S. Carrasco, B. E. A. Saleh, M. C. Teich, and J. T. Fourkas, J. Opt. Soc. Am. B **23**, 2134 (2006).

[70] S. Quabis, R. Dorn, M. Eberler, O. Glckl, and G. Leuchs, Optics Communications **179**, 1 (2000).

[71] R. Dorn, S. Quabis, and G. Leuchs, Phys. Rev. Lett. **91**, 233901 (2003).

[72] J. Bar-David, N. Voloch-Bloch, N. Mazurski, and U. Levy, Scientific Reports **6**, 34272 (2016).

[73] K. Willig, S. Rizzoli, V. Westphal, R. Jahn, and S. Hell, Nature **117**, 233903 (2016).

[74] P. Török and P. Munro, Opt. Express **12**, 3605 (2004).

[75] K. S. Youngworth and T. G. Brown, Opt. Express **7**, 77 (2000).

[76] S. N. Khonina and I. Golub, J. Opt. Soc. Am. A **29**, 2242 (2012).

[77] L. Novotny, M. R. Beversluis, K. S. Youngworth, and T. G. Brown, Phys. Rev. Lett. **86**, 5251 (2001).

[78] A. La Porta and M. D. Wang, Phys. Rev. Lett. **92**, 190801 (2004).

[79] B. Sick, B. Hecht, and L. Novotny, Phys. Rev. Lett. **85**, 4482 (2000).

[80] F. K. Fatemi, Opt. Express **19**, 25143 (2011).

[81] N. Bozinovic, Y. Yue, Y. Ren, M. Tur, P. Kristensen, H. Huang, A. E. Willner, and S. Ramachandran, Science **340**, 1545 (2013).

[82] C. Gabriel, A. Aiello, W. Zhong, T. G. Euser, N. Y. Joly, P. Banzer, M. Förtsch, D. Elser, U. L. Andersen, C. Marquardt, et al., Phys. Rev. Lett. **106**, 060502 (2011).

[83] X.-F. Qian and J. H. Eberly, Opt. Lett. **36**, 4110 (2011).

[84] S. Berg-Johansen, F. Töppel, B. Stiller, P. Banzer, M. Ornigotti, E. Giacobino, G. Leuchs, A. Aiello, and C. Marquardt, Optica **2** (2015).

[85] Q. Zhan, Opt. Express **12**, 3377 (2004).

[86] G. P. Agarwal, *Nonlinear Fiber Optics*, Optics and Photonics (Academic Press, San Diego, 2006), 4th ed.

[87] J. J. Rasmussen and K. Rypdal, Phys. Scr. **33**, 481 (1986).

[88] A. V. Nesterov and V. G. Niziev, J. Phys. D: Appl. Phys. **33**, 1817 (2000).

[89] K. J. Mitchell, S. Turtaev, M. J. Padgett, T. Čižmár, and D. B. Phillips, Opt. Express **24**, 29269 (2016).

[90] S. Fürhapter, A. Jesacher, S. Bernet, and M. Ritsch-Marte, Opt. Lett. **30**, 1953 (2005).

[91] A. Lehmuskero, Y. Li, P. Johansson, and M. Käll, Opt. Express **22**, 4349 (2014).

[92] M. Chen, M. Mazilu, Y. Arita, E. M. Wright, and K. Dholakia, Opt. Lett. **38**, 4919 (2013).

[93] J. Geddes, J. Moloney, E. Wright, and W. Firth, Optics Communications **111**, 623 (1994).

[94] L. A. Lugiato and R. Lefever, Phys. Rev. Lett. **58**, 2209 (1987).

[95] D. Gomila and P. Colet, Phys. Rev. A **68**, 011801 (2003).

[96] W. J. Firth and A. J. Scroggie, Phys. Rev. Lett. **76**, 1623 (1996).

[97] M. Soljac˘ić and M. Segev, Phys. Rev. Lett. **86**, 420 (2001).

[98] G.-L. Oppo, A. J. Scroggie, and W. J. Firth, Phys. Rev. E **63**, 066209 (2001).

[99] M. Haelterman, S. Trillo, and S. Wabnitz, J. Opt. Soc. Am. B **11**, 446 (1994).

[100] C. Degen, I. Fischer, and W. Elsäßer, Opt. Express **5**, 38 (1999).

[101] R. W. Waynant, *Lasers in Medicine* (Springer, 1984), 2nd ed.